Microlayer and Contact Line Evaporation during the Dewetting of a Volatile Liquid on a Superheated Solid

Dissertation

Kai Schweikert

TECHNISCHE UNIVERSITÄT DARMSTADT

Mechanical Engineering Department

Institute for Technical Thermodynamics

Microlayer and Contact Line Evaporation during the Dewetting of a Volatile Liquid on a Superheated Solid

Dünnfilm- und Kontaktlinienverdampfung während der Entnetzung einer flüchtigen Flüssigkeit an einem überhitzten Feststoff

Accepted doctoral thesis by Kai Schweikert

1. Review: Prof. Dr.-Ing. Peter Christian Stephan
2. Review: Prof. Dr. Paolo Di Marco

Date of submission: 22.11.2021
Date of thesis defense: 26.01.2022

Darmstadt

Please cite this document as:
URN: urn:nbn:de:tuda-tuprints-198599
URL: http://tuprints.ulb.tu-darmstadt.de/19859

This document is provided by tuprints,
E-Publishing-Service of TU Darmstadt
http://tuprints.ulb.tu-darmstadt.de
tuprints@ulb.tu-darmstadt.de

Dünnfilm- und Kontaktlinienverdampfung während der Entnetzung einer flüchtigen Flüssigkeit an einem überhitzten Feststoff

Microlayer and Contact Line Evaporation during the Dewetting of a Volatile Liquid on a Superheated Solid

Accepted doctoral thesis by Kai Schweikert

Institute for Technical Thermodynamics
Mechanical Engineering Department
Technical University of Darmstadt

1. Review: Prof. Dr.-Ing. Peter Christian Stephan
2. Review: Prof. Dr. Paolo Di Marco

Darmstadt, 2022

Danksagung

Die vorliegende Dissertationsschrift entstand während meiner Anstellung als wissenschaftlicher Mitarbeiter am Fachgebiet für Technische Thermodynamik der Technischen Universität Darmstadt. Ich möchte mich ganz herzlich bei Herrn Prof. Peter Stephan für die Möglichkeit bedanken, die Arbeit an seinem Fachgebiet durchzuführen. Das stets entgegengebrachte Vertrauen und die gelassenen Freiräume, sowohl inhaltlich als auch in der Gestaltung des Arbeitsalltages, habe ich sehr geschätzt. Mein Dank gilt auch Dr. Axel Sielaff, der meine Zeit am Institut von meiner ersten Anstellung als Studentische Hilfskraft an begleitet hat. Für seine stets offene Tür, zahlreichen Anregungen und experimentelle Expertise bedanke ich mich sehr.

Besonders bedanken möchte ich mich auch bei allen Initiatoren sowie Mitarbeiterinnen und Mitarbeitern des Sonderforschungsbereiches 1194, aus dem diese Arbeit hervorging. Der geschaffene Raum für interdisziplinären Austausch, der mit zahlreichen internationalen Vorträgen und Seminaren angeregt wurde, war jederzeit interessant, produktiv und inspirierend. In diesem Zusammenhang bedanke ich mich auch bei der Deutschen Forschungsgemeinschaft für die finanzielle Unterstützung.

Ich möchte mich insbesondere auch bei allen Kolleginnen und Kollegen, sowohl am Institut als auch aus dem SFB 1194, bedanken. Neben der fachlichen Zusammenarbeit haben auch die zahllosen Diskussionen inner- und außerhalb der Universität maßgeblich zum Gelingen dieser Arbeit beigetragen. Dieser Dank gilt auch allen Studierenden, die ich betreuen durfte. Besonders bedanke ich mich bei Matthias Zimmermann, nicht nur für die detaillierte Durchsicht dieser schriftlichen Ausarbeitung, sondern auch für die enge Zusammenarbeit im Labor.

Mein ganz besonderer Dank gilt meiner Frau Glorivic für ihre jahrelange Unterstützung in allen Lebenslagen, insbesondere während der Fertigstellung dieser Ausarbeitung.

13. September 2021

Kai Schweikert

Abstract

English

Evaporating thin liquid films, so called microlayers, are of particular importance to two phase heat transfer processes, such as pool boiling or boiling in microchannels. The microlayer can form between wall and growing or moving vapor bubble, elevating heat flux due to its evaporation, and contributing to overall bubble growth. However, a microlayer is not always observed. In this case, heat flux is found to concentrate near the three-phase contact line - the location where solid, liquid, and vapor meet. This mode of heat transfer is thus known as contact line evaporation.

Many aspects of microlayer and contact line evaporation are not sufficiently understood, which limits the modeling and design of boiling applications. For instance, the physical parameters contributing to the formation process of the microlayer and the local heat flux largely remain unclear. Previous studies have indicated a complex interaction between the microscopic processes at the contact line, the wall material, the fluid properties, the wall superheat, and the dewetting velocity. Addressing the individual influence of these parameters directly within a boiling application, however, is rather difficult, as they are coupled in a boiling scenario. Therefore, generic experiments, in which these parameters are decoupled, are carried out in this thesis to investigate the formation and evaporation process of the microlayer on a fundamental level.

German

Verdampfende dünne Flüssigkeitsfilme, sogenannte Dünnfilme, sind von besonderer Bedeutung für Zweiphasen-Wärmeübertragungsprozesse, zum Beispiel für das Sieden. Bildet sich ein Dünnfilm zwischen Wand und wachsender, bzw. sich bewegender Dampfblase, so kann dessen Verdampfung den Wärmestrom stark erhöhen und signifikant zum Blasenwachstum beitragen. Ein Dünnfilm wird jedoch nicht immer beobachtet. Fehlt ein Dünnfilm, dann konzentriert sich der Wärmestrom vorwiegend nahe der Dreiphasen-Kontaktlinie - der Stelle, an der Feststoff, Flüssigkeit und Dampf aufeinandertreffen. Dieser Verdampfungsmodus ist daher als Kontaktlinienverdampfung bekannt.

Viele Aspekte der Dünnfilm- und Kontaktlinienverdampfung sind bisher nur unzureichend verstanden, was die Modellierung und Auslegung von Siedeanwendungen erschwert. Hierzu zählen besonders die genauen physikalischen Zusammenhänge, die für die Entstehung des Dünnfilms und die Beschreibung des lokalen Wärmestroms von Bedeutung sind. Bisherige Studien deuten auf eine komplexe Wechselwirkung zwischen den mikroskopischen Prozessen an der Kontaktlinie, den Fluid- und Wandeigenschaften, der Wandüberhitzung und der Entnetzungsgeschwindigkeit hin. Die genaue Untersuchung der einzelnen Einflussparameter direkt in einer Siedeanwendung ist jedoch nur begrenzt möglich, da sie im Siedeprozess gekoppelt sind. In dieser Arbeit werden die

The dip-coating geometry, where a sample is vertically withdrawn from a stationary pool of liquid, is chosen as a basis for the experimental facility. This widely used method is adapted for the use of infrared thermography, with which the temperature at the solid/liquid interface is determined during the dewetting procedure. The experimental set-up is presented and an infrared calibration method, which accounts for the movement of the sample, is developed. The local heat flux is obtained from inverse numerical simulation.

The presented experimental results indicate that microlayer formation occurs at a critical dewetting velocity, which increases with the wall superheat. Both quantities are thereby linked by the evaporation near the contact line. Correlations for this regime boundary are presented and compared with analytical descriptions from literature to illuminate the mechanism responsible for the regime transition. Heat flux near the contact line and across the microlayer is analyzed in detail. The total heat flux dramatically increases, when a microlayer is formed. The local heat flux across the microlayer is shown to be linked to the thermal boundary layer in the solid substrate. An analytical description for the local heat flux is presented, from which an expression for the length of the microlayer is deduced. Good agreement to the experimental measurements is found in both cases.

Einflussparameter daher mithilfe generischer Experimente entkoppelt und der Entstehungs- und Verdampfungsprozess des Dünnfilms so grundlegend untersucht.

Der entwickelte Versuchsaufbau basiert auf einer Probe, die vertikal aus einer stationären Flüssigkeit herausgezogen wird. Der Einsatz von Infrarot-Thermografie wird ermöglicht, um die lokale Temperatur an der Fest-/Flüssig-Grenzfläche während des Entnetzungsvorganges zu bestimmen. Der Versuchsaufbau wird vorgestellt und eine Infrarot-Kalibriermethode entwickelt, in der die Bewegung der Probe berücksichtigt wird. Die Ermittlung des lokalen Wärmestroms erfolgt mittels inverser numerischer Simulationen.

Die präsentierten experimentellen Ergebnisse zeigen, dass ein Dünnfilm erst oberhalb einer kritischen Entnetzungsgeschwindigkeit, die mit der Wandüberhitzung zunimmt, entsteht. Beide Größen sind dabei über die Verdampfung nahe der Kontaktlinie gekoppelt. Korrelationen für die Regimegrenze werden abgeleitet und mit analytischen Beschreibungen aus der Literatur verglichen, um den für den Regimewechsel verantwortlichen Mechanismus näher zu untersuchen. Der Wärmestrom nahe der Kontaktlinie und im Bereich des Dünnfilms wird im Detail analysiert. Der insgesamt übertragene Wärmestrom steigt drastisch an, sobald ein Dünnfilm entsteht. Es wird gezeigt, dass der lokale Wärmestrom im Bereich des Dünnfilms mit der thermischen Grenzschicht im Feststoff gekoppelt ist. Der lokale Wärmestrom wird analytisch beschrieben und ein Ausdruck für die Dünnfilmlänge abgeleitet. In beiden Fällen zeigt sich eine gute Übereinstimmung mit den experimentellen Ergebnissen.

Contents

Nomenclature

Latin Symbols

Symbol	Description	unit
a, b	coefficients	-
$Ai(s_{max})$	maximum of the Airy function	-
B	boundary	-
c	calibration coefficient	-
c_p	specific heat capacity	$\mathrm{J\,kg^{-1}\,K^{-1}}$
C	empirical constant	-
d	diameter	m
e	measurement uncertainty	various
f	frame rate	$\mathrm{s^{-1}}$
F	frame number	-
g	gravitational acceleration	$\mathrm{m\,s^{-2}}$
h	microlayer length in steady state	m
I	intensity	counts
l_c	capillary length	m
l_i	microscopic length scale	m
l_{slip}	slip length	m
m_{ev}	evaporated mass flow	$\mathrm{kg\,s^{-1}}$
m_{ml}	mass flow entrained into the microlayer	$\mathrm{kg\,s^{-1}}$
m_{re}	mass flow returning to the bulk liquid region	$\mathrm{kg\,s^{-1}}$
m_{up}	upward mass flow due to wall drag	$\mathrm{kg\,s^{-1}}$
N	resolution of the calibration	-
p	pressure	$\mathrm{N\,m^{-2}}$
P	Pearson correlation coefficient	-
P_a	auto-correlation function	-
P_{corr}	correlation limit	-
P_G	P adjacent to the center frame	-
q	local heat flux	$\mathrm{W\,m^{-2}}$
Q	integrated heat flux	$\mathrm{W\,m^{-1}}$
r	radius	m
R	thermal resistance	$\mathrm{K\,W^{-1}}$
R_a	roughness (arithmetical mean deviation)	µm
t	time	s
T	temperature	K

T_{IR}	temperature measured by infrared thermography	K
T_{ref}	thermocouple reference temperature	K
T_w	wall temperature in the bulk liquid region	K
u	dewetting velocity	$\mathrm{m\,s^{-1}}$
var	variance	various
U, V, W	position, temperature and calibration reference images	various
x, y, z	Cartesian coordinates	m

Greek Symbols

Symbol	Description	unit
α	ratio of thermal resistance in solid and liquid	-
γ	thermal boundary layer thickness in the solid	m
δ	liquid film thickness	m
δ_{bl}	velocity boundary layer thickness	m
δ_{con}	δ calculated assuming linear heat conduction	m
δ_{IP}	δ measured by interferometry	m
δ_{IPS}	mean of δ_{IP} in steady state	m
Δ	difference	-
Δh_v	specific enthalpy of vaporization	$\mathrm{J\,kg^{-1}}$
ΔT	wall superheat	K
Δy_m	meniscus rise	m
ϵ	positive infinitesimal number	-
θ	contact angle	deg
θ_{app}	apparent contact angle	deg
θ_e	equilibrium contact angle	deg
λ	thermal conductivity	$\mathrm{W\,m^{-1}\,K^{-1}}$
μ	dynamic viscosity of the liquid	$\mathrm{kg\,m^{-1}\,s^{-1}}$
ν	kinematic viscosity of the liquid	$\mathrm{m^2\,s^{-1}}$
ρ	density	$\mathrm{kg\,m^{-3}}$
σ	surface tension	$\mathrm{N\,m^{-1}}$
χ	relative position of sample and infrared sensor	m
Ω	angular velocity	$\mathrm{rad\,s^{-1}}$

Subscripts

Symbol	Description
0	initial / at beginning of microlayer
b	bulk liquid region
B	bubble
cl	contact line
con	obtained by conduction model
cr	critical
dep	deposition
end	end of movement
ev	evaporative
g	gas
i	position index
k	single experiment index
l	liquid
m	pixel index
max	maximum
$mean$	mean during steady state
med	median during steady state
men	meniscus region
min	minimum
mov	moving
M	marker
$noise$	limit due to noise
n	reference temperature index
r	ridge
s	solid
sim	simulation
sta	static
$start$	beginning of movement
t	threshold
tot	total
w	wall

Superscripts

Symbol	Description
eth	ethanol
FC	FC-72
$H2O$	water

Accents

Symbol	Description
$\circ^*$	modified
$\overline{\circ}$	mean of multiple experiments
$\vec{\circ}$	vector

Non-dimensional Groups

Symbol	Description	Definition
Ca	Capillary number	$\mu u/\sigma$
Bo	Bond number	$\rho_l r^2 u_B/\sigma t$
Ja	Jakob number	$\Delta T c_p/\Delta h_v$
Pr	Prandtl number	$\mu c_{p,l}/\lambda_l$
Re	Reynolds number	du/ν
We	Weber number	$\rho_l u^2(d/2-\delta)/\sigma$

Abbreviations

Abbreviation	Description
BC	boundary condition
CaF_2	calcium fluoride
CER	contact line evaporation regime
FC-72	perfluorohexane, C_6F_{14}
FOV	field of view
LLD	Landau-Levich-Derjaguin
MER	microlayer evaporation regime

CHAPTER 1

Introduction

The formation of thin liquid films is an often encountered phenomenon and can be easily observed at the side of a glass filled with water. Tilting the glass slowly produces no significant effect; the liquid on the rear side of the glass only slowly recedes and the glass above the liquid remains dry. In contrast, if the glass is tilted quickly or one is to swivel the liquid, a thin film is left on the side of the glass[1]. The described process is also referred to as *dynamic (de-)wetting*. The formation of such liquid films is fundamental to many industrial applications, from which printing and coating processes are naturally the most obvious. While this classical application might seem simple, emerging fields, such as printing of electronics or functional coatings, do not only require a deep understanding of the interaction between solid and liquid, but also of additional effects caused by, for example, evaporation or surfactants [7, 112, 126]. In other applications, on the other hand, these films present a technical limitation and their formation is actively avoided, such as in immersion lithography or microfluidic droplet manipulation.

In the field of two-phase heat transfer, liquid films are of particular importance to three fundamental boiling processes, which are illustrated in Figure 1.1. The classic field of nucleate pool boiling is represented by a growing vapor bubble sketched in Figure 1.1a. Underneath these vapor bubbles, thin liquid films have been observed that feed the bubble with vapor as they evaporate [86]. The thickness of these films lies within the range of a few micrometers and they are, thus, often referred to as *microlayers*. Figure 1.1b illustrates a vapor bubble in the context of flow boiling, where the vapor bubble grows in the presence of a convective liquid flow. The bubble is moved across the stationary substrate before detaching, which can influence the microlayer underneath it. As part of the most fundamental heat transfer processes, both pool and flow boiling are essential to countless industrial processes, such as distillation and rectification, power generation or cooling applications. Lastly, Figure 1.1c illustrates boiling in closed microchannels, which is, for example, encountered in microfluidic reactors, high performance cooling of microelectronics or aerospace components. As the vapor bubble moves through the heated capillary, a microlayer can be left between the wall and the moving vapor [82, 148]. Due to the finite length of the microlayer, a dry spot can be created on the wall in all three applications. The location at the end of the microlayer, where liquid,

[1] Please note that the water might spill out of the glass when tilted too far during this experiment.

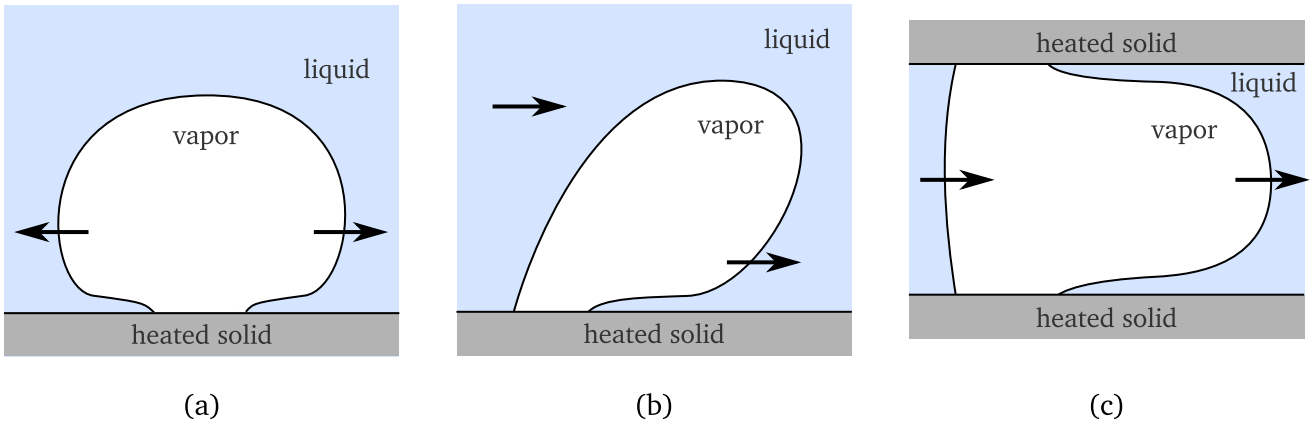

Figure 1.1: Microlayers in three boiling processes: (a) pool boiling, (b) flow boiling, (c) boiling in microchannels. The arrows indicate the direction of flow.

vapor, and solid wall meet, is thereby referred to as the *three-phase contact line* and of large importance to the overall phenomenon. It is important to note that these microlayers are not always observed and their formation remains within the focus of research. Two models thereby exist to describe the heat transfer either without a microlayer, so called *contact line evaporation*, or with a microlayer, so called *microlayer evaporation* [86]. Under what conditions which model is more applicable, however, largely rests on assumptions and empirical evidence, and is subject of ongoing scientific discussion. Furthermore, even when a microlayer is surely present, its overall nature and contribution to heat flux often remains unclear and varies depending on, for example, the used boiling configuration or fluid. Without this understanding, it is clear that the design of new and improved boiling applications, that meet the ever growing demands for efficiency or increased heat flux densities, is very challenging.

However, the generic study of microlayers directly within the boiling processes sketched in Figure 1.1 is rather difficult. Besides geometric constraints that arise from the nature of the experiment, parameters that are likely of large importance to the problem can not be individually varied in a boiling situation. For example, the expansion velocity of a vapor bubble in pool boiling can only be indirectly effected, such as through the fluid properties or the wall temperature. Additional quantities are, therefore, changed in the process of altering the expansion velocity, which complicates the identification of influential parameters and underlying physics. Furthermore, the time and length scales relevant for microlayer evaporation are very small and experimental observation hence challenging. Numerical simulations have, therefore, gained large importance in boiling research. However, these simulations do rely on assumptions and models, especially to describe the physics near the three-phase contact line. Thus, the investigation of microlayer formation remains a joint effort of both numerical and experimental methods, where validation data is supplied by the latter. Highly controlled generic experiments dedicated to the investigation of a single phenomenon thereby offer a convenient way for validation of different numerical approaches, because the

complexity of the numerical computation and possible experimental confounding factors are reduced.

The remarks made above show that a generic experimental study of the formation and evaporation of microlayers is needed. Rather than focusing on one particular boiling configuration, the experimental set-up should be centered around their similarities, i.e. the dewetting area where the microlayer is formed. Observations made in such a configuration could then be applied to the individual boiling processes, and used for the validation of numerical simulations.

Structure of this thesis

The thesis is structured into five chapters, whose contents are briefly outlined below:

Chapter 1: Introduction

A general overview of contact line evaporation and microlayer evaporation and their importance to two phase heat transfer processes is given.

Chapter 2: State of the art

A review of relevant published literature is conducted. Three main topics are identified, namely heat transfer at the contact line, thin liquid films with and without evaporation, and the forced dynamic wetting transition. On the basis of this review, the objective of this thesis is outlined.

Chapter 3: Methods of investigation

This chapter focuses on the experimental and numerical methods used within this work. The experimental set-up is presented, which includes the samples, fluids and measurement equipment. Special attention is given to the calibration method of the infrared camera. This is followed by the presentation of the numerical method used to calculate the local heat flux. The analysis of the obtained measurement data is explained and an error analysis is conducted.

Chapter 4: Results and discussion

The experimental results are presented and discussed. The shape of the microlayer during its various states of existence is presented first, which is followed by a discussion of the regime boundary. The experimental data is compared to expressions and data from literature to illuminate the mechanism responsible for microlayer formation. Afterwards, heat flux in both the contact line evaporation regime and the microlayer

evaporation regime is discussed in detail. Analytical expressions are derived to describe the local heat flux across the microlayer and the microlayer length. The chapter ends with an interpretation of the presented results within the context of nucleate boiling.

Chapter 5: Summary, conclusion, and outlook

The obtained results are briefly summarized and concluding remarks are made. An outlook on the possible direction of further study is given at the end of the thesis.

CHAPTER 2

State of the art

2.1 Hydrodynamics and heat transfer near the three-phase contact line

The way a liquid wets a surface is largely determined by the processes near the three-phase contact line, the location where solid, liquid, and vapor physically meet. In this section, two different, but widely used, modeling approaches for the contact line are introduced. Both approaches fundamentally differ because they were originally developed to describe different effects. The first approach is referred to as the *micro angle* approach and assumes a finite contact angle at the wall. This is commonly done in the field of dynamic wetting of partially wetting liquids without evaporation. The second concept was developed to describe the evaporation of perfectly wetting liquids and is referred to as the *micro region* approach.

2.1.1 Hydrodynamics of moving contact lines of partially wetting liquids

Figure 2.1 illustrates the meniscus region of a partially wetting fluid on a vertical wall. The static case, in which neither fluid nor solid wall are in motion, is shown in Figure 2.1a. The liquid meets the wall at a finite equilibrium contact angle θ_e, which is determined by a balance of the interfacial forces at the contact line:

$$\cos(\theta_e) = \frac{\sigma_{sg} - \sigma_{sl}}{\sigma_{lg}}. \tag{2.1}$$

Equation 2.1 is known as Young's equation. σ_{sg},σ_{sl}, and σ_{lg} refer to the surface tension of the interface between solid-gas, solid-liquid and liquid-gas, respectively. For simplification, σ_l is used to describe σ_{lg} in the following. $\theta_e = 0°$ is commonly referred to as *perfect wetting*, while $\theta_e > 0°$ is known as *partial wetting*. Far away from the wall illustrated in Figure 2.1a, the free liquid surface is horizontal, while $\theta_e < 90°$ exists at the wall. Close to the wall, in the so called liquid meniscus region, the liquid interface thus has to curve upwards to connect the contact angle to the horizontal free liquid surface. This creates a Laplace pressure

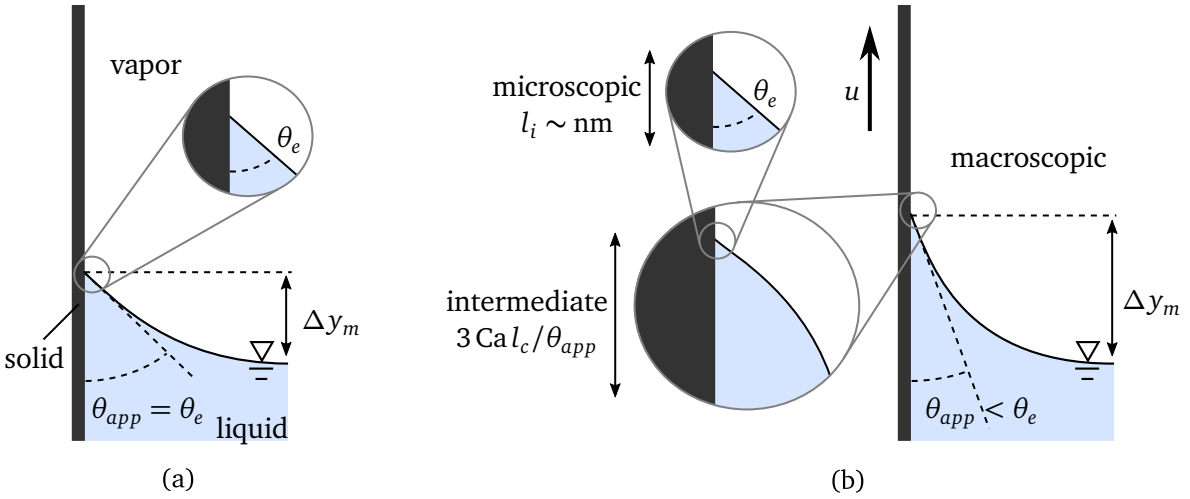

Figure 2.1: Illustration of the (a) static liquid meniscus and (b) multiscale structure of a dynamic liquid meniscus on a vertical wall according to the micro angle approach.

difference across the interface and causes the contact line to rise above the horizontal liquid surface by the meniscus rise Δy_m [94, 95]:

$$\Delta y_m = l_c \sqrt{2\left(1 - sin\left(\theta_{app}\right)\right)}, \tag{2.2}$$

where the length scale l_c is the capillary length

$$l_c = \sqrt{\frac{\sigma_l}{\rho_l g}}. \tag{2.3}$$

In Equation 2.3, ρ_l is the density of the liquid and g the gravitational acceleration. In the static case, the macroscopically observed apparent contact angle θ_{app} is equal to θ_e. This situation changes once the wall is moved relative to the bulk fluid with the dewetting velocity u, in a so called dynamic wetting situation, which is illustrated in Figure 2.1b. Please note that opposed to the convention followed in many other works, positive values of u correspond to a dewetting situating throughout this work. As the system is driven out of equilibrium by the upward motion of the wall, the contact line rises above its equilibrium and, according to Equation 2.2, θ_{app} determined on the macroscopic length scale l_c decreases below θ_e. Near the contact line, on a microscopic length scale of l_i, however, θ_e is still determined by Equation 2.1 and, therefore, remains unchanged. Both regions are connected by an intermediate region, where the shape of the liquid interface changes from θ_{app} to θ_e. At very low u, the relationship between u, θ_e, and θ_{app} can be described by the Cox-Voinov law [10, 20, 137, 157]:

$$\theta_{app}^3 = \theta_e^3 - 9\,\mathrm{Ca}\,\ln\left(\frac{a l_c}{l_i}\right), \tag{2.4}$$

where a is a problem dependent constant [10, 137] and the velocity scale Ca is the capillary number

$$\mathrm{Ca} = \frac{\mu u}{\sigma_l}, \tag{2.5}$$

with the dynamic viscosity of the liquid μ. The size of the intermediate region can be estimated to $3\,\mathrm{Ca}\,l_c\theta_{app}^{-1}$ [10]. However, Equation 2.4 does not generally describe the dynamic meniscus shape of a dewetting situation very accurately, but a full solution of the hydrodynamic problem is needed if $\ln(l_c/l_i) \geq \theta_e^3/9\,\mathrm{Ca}$ [10, 28, 137]. In particular, Equation 2.4 is not valid as θ_{app} approaches zero [137].

2.1.2 Heat transfer at the contact line in perfectly wetting liquids

In perfectly wetting liquids, the equilibrium contact angle is zero. However, it is well known that in both partially and perfectly wetting liquids the apparent contact angle increases with the level of wall superheat $\Delta T = T_{ls} - T_{sat}$, which is the difference between the temperature of the solid substrate at the solid-liquid interface T_{ls} and the saturation temperature of the fluid T_{sat} [2]. Hence, the apparent contact angle of a perfectly wetting liquid can be finite due to the effects of evaporation, even though the equilibrium contact angle of the isothermal system is zero. To describe this phenomenon, Potash and Wayner [116] assumed that a physical contact line is in fact non-existent because the solid surface is covered by a very thin *adsorbed* layer. This modeling approach saw further development by Wayner et al. [161], Moosman and Homsy [108], Stephan [145], Stephan and Busse [144] and Kunkelmann [90]. The concept of the model is sketched in Figure 2.2.

In the adsorbed layer region, the film thickness δ is very small, but evaporation does not occur due to strong adhesion forces, which are described by disjoining pressure in the modeling approach. As δ increases, the disjoining pressure weakens, while the distance between wall and liquid-vapor interface remains low. Consequently, high evaporative flux occurs in the micro region, which spans approximately 0.5 µm along the wall [128]. With increasing δ, the resistance for heat conduction increases, evaporative heat flux reduces, and the liquid interface converges with the macroscopic liquid (macro region) forming the evaporative contact angle θ_{ev}. A Laplace pressure difference thereby exists between micro and macro region due to the high curvature of the liquid interface in the micro region, which induces a liquid flow from macro to micro region and replenishes the mass lost by evaporation. The described process causes a strong cooling effect in the micro region and a subsequent decrease in substrate temperature [144]. This local temperature drop, which indicates high local heat flux, has been observed by many researches, for example in generic experiments of static evaporating menisci [25, 70, 71], dynamic evaporating menisci [35], drop impingement [44, 45, 67, 105], and boiling [111, 132, 135, 160]. The latter case will be discussed in more detail in section 2.2.1, as it is of particular relevance to this thesis. Furthermore, Raj et al. [122] found good overall agreement of θ_{ev} obtained by the micro region model with the apparent contact angle measured on static evaporating droplets of FC-72 (perfluorohexane, C_6F_{14}).

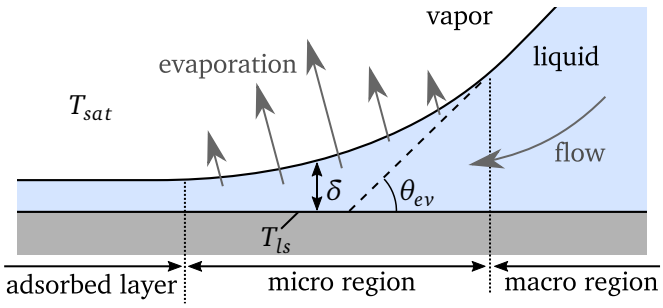

Figure 2.2: Illustration of the contact line according to the micro region model.

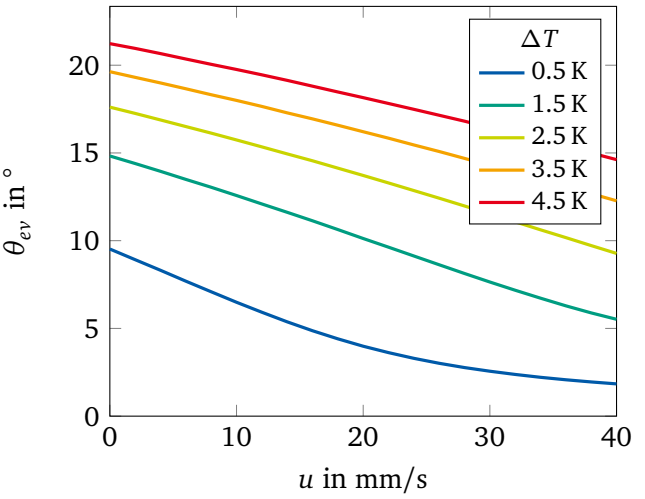

Figure 2.3: θ_{ev} in FC-72 calculated with the micro region model by Schlawitschek [128] for varying u and ΔT.

The micro region model as presented above does not consider the effects of contact line motion and θ_{ev}, therefore, coincides with the macroscopically observable static apparent contact angle θ_{app}. Different approaches exist to consider the effects of contact line motion. One is to assume the micro region decoupled from the dynamic effects in the macro region, which is adopted by, for example [73, 74, 110, 123, 124, 125]. Thus, θ_{ev} remains only a function of ΔT. It is argued that, in a hydrodynamic sense, θ_{ev} obtained by the micro region model is comparable to θ_e for partially wetting liquids of the micro angle approach. The dynamic contact angle can hence be obtained with Equation 2.4 by substituting θ_e for $\theta_{ev}(u = 0)$ [75, 123, 124].

A different approach was taken by Batzdorf [5], who included the effects of contact line motion directly in the micro region model. In this approach, θ_{ev} is a function of both u and ΔT. The model served as the basis for numerical studies of drop impingement [67, 68] and boiling [27, 39]. Schlawitschek [128] introduced the Kapitza resistance, which describes an additional thermal resistance at the solid-liquid interface. θ_{ev} of FC-72 calculated with the micro region model presented by Schlawitschek [128] for varying levels of ΔT and dewetting velocity u is shown in Figure 2.3. The trends observed are in general agreement with the already mentioned dependency of θ_{app} on ΔT and u: For $u = const.$, θ_{ev} increases with ΔT. With increasing u, however, θ_{ev} decreases and asymptotically approaches zero for large u or small ΔT. The heat flux in the microlayer region, however, largely increases with ΔT and shows little dependency on u. The latter has also been observed experimentally by Fischer [35].

For the sake of completion, it is pointed out that efforts have been made to apply the approach of the micro region model to partially wetting liquids, for example by Ajaev et al. [1] by assuming a non-monotonous shape of the disjoining pressure. However, Janecek [73] argued that such an approach is impractical because it relies on (as of now) unmeasurable surface forces. Instead of an adsorbed layer, Janecek proposed the

existence of a finite contact angle at the end of the micro region similar to the micro angle approach. By assuming this angle to be very small (8° for FC-72), this hybrid model has been shown to also describe perfectly wetting liquids and give practically the same result for θ_{ev} as the micro region model used by Kunkelmann and Stephan [91] and Raj et al. [122], i.e. without the consideration of contact line motion [73, 74]. Good comparison to experiments has also been obtained for ethanol [38].

2.2 Thin liquid films and microlayers in various processes

In this section, research concerning thin liquid films found in various experimental configurations is presented. The research is thereby structured by the geometric configuration, namely nucleate pool boiling, microchannels, and dip-coating, to emphasize similarities and differences of the liquid films between them. For microchannels and dip-coating, studies without evaporation are discussed before studies with evaporation. For the sake of consistency, an evaporating thin liquid film is thereby always referred to as a microlayer.

2.2.1 Nucleate pool boiling

Shape and thickness of the microlayer

The idea that a microlayer can be left underneath a growing vapor bubble is widely credited to Snyder and Edwards [140][1]. They proposed that the evaporation of the microlayer should cause rapid fluctuations of the local temperature underneath the bubble. The first experimental evidence for such fluctuations was supplied by Moore and Mesler [107], who measured the temperature changes with a small thermocouple and an oscilloscope. Using an energy balance, the thickness of the microlayer was estimated to approximately 2 µm. Hendricks and Sharp [66] carried out similar experiments, but also included an image capturing system, which allowed them to show these fluctuations do indeed correlate to the growth of the bubble. The first direct measurements of microlayers were performed by Sharp [134] using interferometry. The thickness was evaluated to be of the order of 0.4 µm. The experiments also showed the thinning of the microlayer due to evaporation proposed by Snyder and Edwards [140], which led to a growing dry patch underneath the bubble. Interferometry was also used by Jawurek [76], who measured a microlayer thickness of 0.2 µm and 0.8 µm using the fluids methanol and ethanol, respectively. In addition, the initial shape of the microlayer resembled a wedge, whose thickness increased linearly with the distance from the center of the bubble. This wedge-like shape is illustrated in Figure 2.4a. The earliest thickness values reported by Sharp [134] and Jawurek [76], however, most likely carry an error stemming from insufficient monochromatic illumination [158] or insufficient resolution [99]. It has since been determined by many researchers that the general thickness of the microlayer is about one order of magnitude larger.

[1] For example according to [86]. The original source was not available to the author.

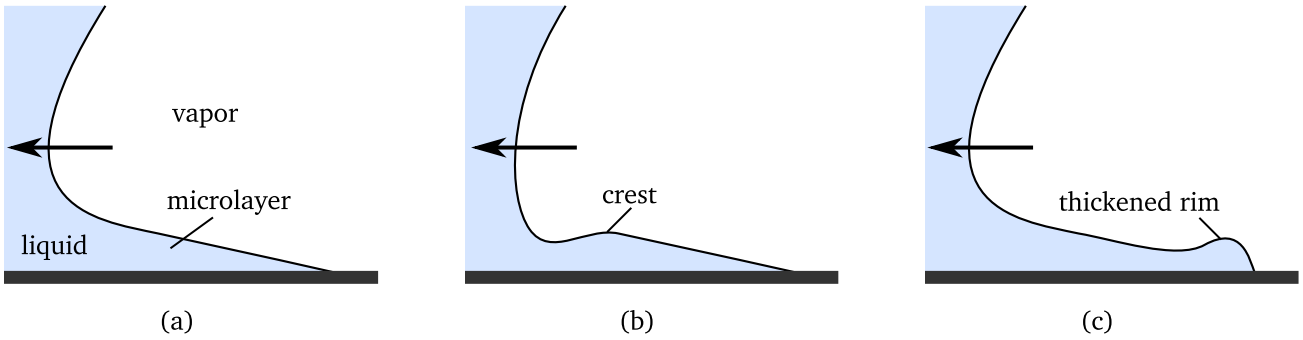

Figure 2.4: Illustration of the microlayer shape underneath a growing vapor bubble in nucleate pool boiling, where the arrow indicates the expansion direction of the bubble: (a) wedge-shape, (b) crest-like shape observed by Chen et al. [15], (c) thickened rim observed by Gion [47] and Urbano et al. [151].

A wedge-like shape is also assumed by Cooper and Lloyd [19], who estimated the microlayer thickness from temperature changes underneath the bubble measured using thermocouples. Based on an analytical model, they proposed Equation 2.6 to estimate the initial thickness of the microlayer δ_0, i.e. the thickness before thinning due to evaporation, from the kinematic viscosity of the liquid ν and the growth time of the bubble t:

$$\delta_0 = C\sqrt{\nu t}. \tag{2.6}$$

The empirical constant C was found to be of the order 0.8 for their working fluids toluene and isopropyl alcohol, which corresponds to a thickness value in range of $6-56\,\mu m$. Voutsinos and Judd [158] quantified the initial microlayer thickness to approximately $5\,\mu m$ for dichloromethane using laser interferometry. For ethanol and water, the experiments conducted by Koffman and Plesset [87] agreed well with $C = 0.3-0.4$ ($3\,\mu m$), while Gao et al. [42] found $C = 0.22$ ($4\,\mu m$). MacGregor and Jawurek [99] reported a thickness value of $5\,\mu m$ and $C = 0.27$ for methanol. Koffman and Plesset [87] also noted that the microlayer thickness in ethanol was about 1.6 times higher than in water, when compared at the same distance from the bubble center. This trend is in agreement with experiments carried out by Utaka et al. [153], who applied a laser extinction method to determine δ_0. Microlayers formed in ethanol were found to be of the same wedge-like shape as those formed in water but to be about twice as thick. Utaka et al. present the following correlations for δ_0:

$$\delta_0^{H2O} = 4.46\times10^{-6}\ r_B \qquad \text{for water,} \tag{2.7}$$

$$\delta_0^{eth} = 10.2\times10^{-6}\ r_B \qquad \text{for ethanol,} \tag{2.8}$$

where r_B describes the bubble radius measured from the center of the bubble. In the study of Utaka et al. [153], heat flux had little effect on the microlayer thickness, which is also reported by Chen et al. [17].

The authors used interferometry to determine the microlayer thickness of water at high heat fluxes, where smaller bubbles and faster bubble growth rates were observed. While the microlayer thickness showed little change, the microlayer length decreased with increasing heat flux, which is accounted by decreasing bubble radii. Yabuki and Nakabeppu [165] evaluated microlayer thickness based on wall temperature measurements using a micro-electro-mechanical systems sensor and noted that thicker microlayers are observed at higher levels of wall superheat. In contrast to Utaka et al. [153] and Chen et al. [17], the increase is accounted to higher bubble growth velocities at increasing ΔT. A correlation was proposed, which predicted their own data within ±30% and showed good agreement with the measurements by Utaka et al. [153]. In a later study, Yabuki and Nakabeppu [167] observed an opposite trend, i.e. δ_0 decreasing with the bubble growth velocity. It was argued that this might be due to the effect of acceleration, which is also observed in microchannels and is discussed in section 2.2.2. Based on this premise, Yabuki and Nakabeppu [166] correlated δ_0 to the thickness of the velocity boundary layer δ_{bl} near the bubble foot and the Bond number Bo:

$$\delta_0 = 0.13\,\delta_{bl}\mathrm{Bo}^{0.38} \qquad \text{with} \qquad \mathrm{Bo} = \frac{\rho_l r_B^2 u_B}{\sigma_l t}, \tag{2.9}$$

where u_B describes the expansion velocity of the bubble and ρ_l the density of the liquid. Bure and Sato [12] compared the correlations by Utaka et al. [153] (Equation 2.7 and Equation 2.8) to an expression for the microlayer thickness originally derived by van Stralen et al. [156]:

$$\delta_0 \sim \sqrt{\mathrm{Pr}}\; r_B \qquad \text{with} \qquad \mathrm{Pr} = \frac{\mu c_{p,l}}{\lambda_l}, \tag{2.10}$$

where Pr is the Prandtl number, with the specific heat capacity of the liquid $c_{p,l}$ and the thermal conductivity of the liquid λ_l. Bure and Sato [12] noticed that the ratio of Equation 2.7 to Equation 2.8 is very similar to the ratio of $\sqrt{\mathrm{Pr}}$ of the same fluids and called for further study on the matter.

A deviation from the wedge-like shape was reported by Chen et al. [15], who measured a reduction in microlayer thickness near the outer radius of the bubble using interferometry. This crest-like shape is illustrated in Figure 2.4b. However, this was only observed near the end of the initial bubble expansion and is proposed to be a result of the buoyancy forces and the beginning of bubble detachment. A later study revealed that the same bent shape also exists for ethanol [152]. Results of direct numerical simulations by Gion [47] and Urbano et al. [151] both suggest another deviation from the wedge-like shape near the contact line, which is illustrated in Figure 2.4c. Here, a thickened rim or bulge formed during the expansion phase of the bubble, when the microlayer was formed. A similar effect occurs during spontaneous dewetting of a partially wetting liquid [139] or an evaporating perfectly wetting liquid [38][2]. However, Bure and Sato [12] point out that the formation of the rim might be of numerical nature in the study of Urbano et al. [151].

[2]Please note, that this bulge is different from the dewetting rim discussed in Equation 2.3.

Influence of the microlayer on heat flux

The importance of the microlayer to the overall heat flux caused by a single bubble was first studied by Judd and Hwang [79] using the results of Cooper and Lloyd [19]. They concluded that the contribution of the microlayer increases with the overall heat flux. A similar trend was observed for decreasing system pressure by Fath and Judd [32], who suggested that the microlayer might not contribute to heat flux at very high pressures at all. At lower pressure and high heat flux, they evaluated the contribution of the microlayer to a maximum of 40%. A slightly higher contribution of 50% was gained by Koffman and Plesset [87]. Kim [86] concluded in a review of numerous experimental and theoretical works that the contribution of the microlayer to overall heat flux does not exceed 25%. According to the author, other effects, such as the re-wetting process or evaporation through the bubble cap, need to be considered to a larger degree. Furthermore, Kim points out that no heat flux model at the time could fully describe the whole bubble cycle. Therefore, quantifying the contribution of the microlayer to overall evaporation is highly difficult and the absolute value may vary depending on the assumptions or models used by each author.

Guo and El-Genk [55] developed a model in which the microlayer is coupled with the heat conduction in the solid substrate, and compared their solutions to the experiments reported by Koffman and Plesset [87]. The deduced heat flux showed a peak near the contact line, which increased significantly with the value chosen for the accommodation coefficient of evaporation (the fraction of evaporated molecules that reach the bulk vapor phase and do not condense back into the liquid). Furthermore, the model suggested that heat flux caused by the microlayer increases with the thermal conductivity of the wall, and that the lateral heat conduction in the solid could be a limiting factor. Yabuki and Nakabeppu [165] point out that the contribution of the microlayer may depend on the physical properties of the fluid, especially the latent heat of evaporation. A similar conclusion is drawn by Utaka et al. [154], who used a model to evaluate the heat flux from their experimental data presented in [153]. Microlayers formed in ethanol only transferred 1/3 of the heat transferred in water, which was mainly accounted to the thicker microlayers of ethanol presenting larger resistance to heat conduction. Furthermore, the heat flux increased with the wall superheat. Overall, the authors concluded that the microlayer's contribution to evaporation can vary within a broad range of 15% — 70%.

Heat flux caused by a microlayer in water was evaluated using three different methods by Jung and Kim [80, 81]. A constant heat flux profile across the microlayer was observed, which accounted for approximately 17% of evaporation. While their results agreed well with the heat flux evaluated by Golobic et al. [50, 51], the absolute values gained by calculating the heat flux using the conduction through the microlayer did not match those of the two other methods used in the study. This problem is addressed by two studies of Giustini et al. [48, 49]. In agreement with Guo and El-Genk [55], the authors concluded that the evaporation thermal resistance of the microlayer has a significant effect on the obtained heat flux. The disagreement was resolved by assuming a very low value of 0.02 for the accommodation coefficient of evaporation, which is further supported by a direct numerical simulation conducted by Hänsch and Walker [59].

Absence of a microlayer

While the existence of a microlayer underneath growing vapor bubbles has been experimentally confirmed, a microlayer is not always observed. Stephan and Hammer [143] proposed a model, which describes the heat flux underneath a growing vapor bubble as largely driven by the evaporation near the three-phase contact line using the micro region model. The model was validated using nucleate boiling experiments with the test liquid R-114 conducted by Barthau [4], showing good agreement within the measurement accuracy. However, the strong evaporation in the vicinity of the contact line theorized by Stephan and Hammer [143] could not be directly observed. The model saw further development by Kern and Stephan [84], Fuchs et al. [40], and Kunkelmann and Stephan [92].

Since the model proposed by Stephan and Hammer [143] does not seem to agree with the evidence provided for the existence of the microlayer gained by interferometry, this modeling approach has since been highly debated, as discussed by Kim [86]. However, the absence of a microlayer was already hypothesized by Cooper and Lloyd [19]. As their model suggests that the microlayer is a result of the contact line being overtaken by the growth of the vapor bubble, they theorized that microlayer formation might be prevented if the contact line is mobile enough to keep up with the expanding vapor bubble. According to the authors, this might be the case for either strongly non-wetting liquids or slowly growing bubbles.

First direct experimental evidence in favor of the model proposed by Stephan and Hammer [143] and the absence of a microlayer was supplied by Sodtke et al. [141], who measured the temperature field underneath a growing vapor bubble in micro-gravity conditions using the refrigerant FC-72 as a working fluid. A ring-shaped drop in local temperature was observed underneath the growing vapor bubble utilizing thermochromic liquid crystals and a similar temperature distribution was obtained using the model of Stephan and Hammer [143]. Similar observations were made by Wagner and Stephan [160], Schweizer [132], Fischer et al. [37], and Nejati et al. [111] using high speed infrared thermography and refrigerants as test liquids. These studies observed that heat flux was indeed concentrated within a small region at the foot of the bubble, where the contact line was assumed. Kim [86] argues, however, that the peak in heat flux observed by Wagner and Stephan [160] does not have to be entirely caused by contact line evaporation alone, but that convection near the foot of the bubble, a short microlayer, or a combination of all three mechanisms could as well be the cause. Sielaff [135] observed in single bubble boiling experiments that the bubble expansion velocity correlates with the local heat flux underneath the bubble. For slow bubble expansion velocity, heat flux was rather concentrated and, thus, associated with the contact line evaporation model. For large bubble expansion velocity, on the other hand, local heat flux was spread over a larger area and, thus, associated with the existence of a microlayer. The bubble expansion velocity thereby increased with the waiting time in between bubble nucleation.

The first numerical study dedicated to the formation process of the microlayer was conducted by Hänsch and Walker [60]. While the model featured no evaporation, it was shown that the formation of the microlayer is a result of surface tension forces and is dependent on the growth rate of the bubble. Evaporation was first implemented by Urbano et al. [151], who identified the wall superheat, the bubble growth velocity and

the contact angle as the main influential parameters for the formation of the microlayer. In a later study, simulations by Urbano et al. [150] of nucleate boiling in zero gravity showed no microlayer formation, even though the same numerical methods had previously shown microlayer formation for different conditions [151]. Guion [53] and Guion et al. [52] concluded from a further numerical study that the mobility of the contact line dictates if a microlayer is formed. Even though the authors used a static contact angle in their work, they note that a dynamic contact angle model is needed to describe this effect more accurately and should, therefore, be used. Hänsch and Walker [59] incorporated evaporation into their study presented in [60] and showed that a microlayer forms for intermediate growth rates, but is quickly depleted through strong evaporation. Similarly to a suggestion made by Yabuki and Nakabeppu [165], the authors state that the microlayer of liquids with a low specific vapor to liquid volume ratio, such as refrigerants, could thus deplete as it is formed, resulting in evaporation being concentrated in the vicinity of the contact line.

2.2.2 Microchannel slug flow

Two-phase heat transfer in microchannels is generally categorized by the dominating flow pattern inside the channel [61]. In so called *slug-flow*, also referred to as the *elongated bubble* regime, the bubble diameter quickly reaches the diameter of the channel and a microlayer is trapped between wall and vapor-phase as the bubble travels through the channel. Individual bubbles are thereby separated by sections of slower moving liquid, the so called *slugs*. Due to the evaporation of the microlayer, this regime is widely regarded to be most beneficial for heat transfer applications [63, 148] and the research presented in this section is hence limited to it. A detailed comparison of the heat transfer mechanisms found in pool boiling and microchannels can be found in [83]. Furthermore, the discussion below is largely focused on the geometry of round capillaries or two flat parallel plates due to their comparability to nucleate boiling on flat substrates.

Studies without evaporation

Having historically been used for the measurement of bulk velocity, air bubbles traveling through circular capillaries filled with liquid can be seen as a classical problem in fluid mechanics. Taylor [147] studied the thickness of the film remaining on the capillary wall by forcing air through a glass capillary filled with a solution of water and glycerin or sucrose. This scenario is illustrated in Figure 2.5 for a channel of diameter d and a bubble front traveling at the velocity u. Experiments were carried out for different concentrations of the solute, through which it was shown that the thickness of the film increased with the capillary number Ca. Using lubrication theory, Bretherton [11] derived an expression for the film thickness δ valid for low Ca and negligible inertia:

$$\delta/d \sim \mathrm{Ca}^{2/3} \qquad \text{for } \mathrm{Ca} << 1 \text{ and } \mathrm{Re} << 1, \tag{2.11}$$

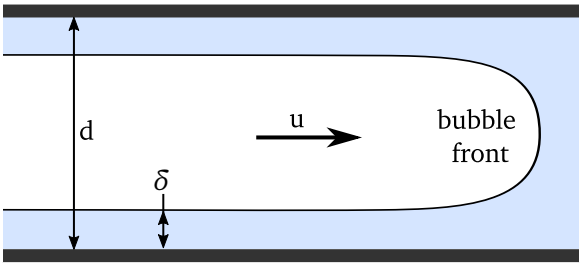

Figure 2.5: Illustration of thin films in microchannels without evaporation.

where Re is the Reynolds number

$$\mathrm{Re} = \frac{du}{\nu}. \tag{2.12}$$

The problem was extended to higher values of Ca by Aussillous and Quéré [3]. The authors obtained a correlation that agreed well with both their own experimental data and the data reported by Taylor [147], and consequently named it *Taylor's Law*:

$$\delta/d = \frac{1.34\,\mathrm{Ca}^{2/3}}{1+2.5\,(1.34\,\mathrm{Ca}^{2/3})} \qquad \text{for } \mathrm{Re} << 1. \tag{2.13}$$

While the coefficient 2.5 is empirical, the coefficient 1.34 was derived by Bretherton [11]. Aussillous and Quéré [3] observed that the film thickness is significantly underestimated by Equation 2.13 if the velocity exceeded $1\,\mathrm{m\,s^{-1}}$. Having observed a similar effect during coating of fibers, they suggested that the thickening is due to inertia effects and proposed the following scaling:

$$\delta/d \sim \frac{\mathrm{Ca}^{2/3}}{1+\mathrm{Ca}^{2/3}-\mathrm{We}} \qquad \text{with} \qquad \mathrm{We} = \frac{\rho_l u^2 (d/2-\delta)}{\sigma_l}, \tag{2.14}$$

in which We describes the Weber number. The effect of inertia was further addressed by a numerical study of Giavedoni and Saita [46], who found that the dependency of the film thickness on Re was not monotonic: At small Re and constant Ca, δ decreases with increasing Re. This effect is then eventually reversed, as Re is increased further. Heil [65] explains this finding by the existence of a vortex close to the dynamic meniscus. The same trend is reported by Kreutzer et al. [89]. Han and Shikazono [56] measured the film thickness with a laser focus displacement meter and concluded that inertia should be considered above $\mathrm{Ca} > 0.02$. Based on Equation 2.14, the authors obtained the following correlation for the film thickness valid across a wide range of Re:

$$\delta/d = \frac{0.67\,\mathrm{Ca}^{2/3}}{1 + 3.13\,\mathrm{Ca}^{2/3} + 0.504\,\mathrm{Ca}^{0.72}\,\mathrm{Re}^{0.589} - 0.352\,\mathrm{We}^{0.629}} \qquad \text{for Re} < 2000. \tag{2.15}$$

In a further study, Han and Shikazono [57] observed that increased bubble acceleration can also lead to a thinning of the film, which is explained by a change in curvature near the bubble front. The authors described the acceleration in terms of the Bond number Bo and presented a correlation for the film thickness of accelerated bubbles.

The research presented above is limited to capillaries with a circular cross section. This geometry, however, is not always suitable for practical application due to limiting factors, such as the manufacturing process or the applied measurement techniques. Therefore, rectangular or square channels are often found in many microfluidic devices and a few remarks on key differences shall be given here. Within these geometries, the fluid accumulates at the corners of the channel, leading to a more complicated shape of the bubble. Wong et al. [164] carried out an analysis for Ca << 1 and proposed that the cross section of the film thickness at the flat sides of the capillary is saddle shaped, experiencing a local maximum at the channel middle and decreasing to a minimum near the liquid-filled corners. While a scaling of $\delta_0 \sim \mathrm{Ca}^{2/3}$ was proposed for the initial liquid film thickness in the middle of the channel, the minima near the edges showed a scaling of $\delta_0 \sim \mathrm{Ca}$. Furthermore, a transversal flow towards the corners changes the shape of the initially deposited film further downstream until it terminates. The saddle shape and scaling laws were supported by numerical works by Hazel and Heil [64] and confirmed experimentally by Chen and Utaka [14, 16], who measured the two dimensional thickness profile using interferometry. As the capillary number increases, the saddle shape is lost and the bubble becomes axisymmetric. Kolb and Cerro [88] and Thulasidas et al. [149] experimentally determined this transition to occur at $\mathrm{Ca} = 0.1$ and $\mathrm{Ca} = 0.4$, respectively. Experimental results by Han and Shikazono [56] showed that the transition is shifted to lower Ca as the Re is increased.

Studies with evaporation

Monde [106] conducted experiments with air bubbles, which passed through a narrow rectangular channel, and measured the temperature change as the bubble moved over a heated section. The microlayer thickness was evaluated from transient temperature changes to $60-80\,\mu\mathrm{m}$. Moriyama and Inoue [109] studied vapor bubbles growing between two superheated parallel plates and measured the temperature change with film thermocouples. The microlayer thickness was calculated to $1-7\,\mu\mathrm{m}$ and decreased with increasing bubble expansion acceleration. The authors presented correlations for the microlayer thickness, which showed a dependency on the Bond number Bo.

Jacobi and Thome [72] proposed that heat transfer in microchannels is dominated by the microlayer. The authors developed a mechanistic *two-zone* model, which was replaced by the now widely accepted *three-zone* model by Thome et al. [29, 148] shortly after. The model is illustrated in Figure 2.6, showing the three zones (1) dry zone, (2) elongated bubble and (3) liquid slug. The microlayer in zone (2) decreases

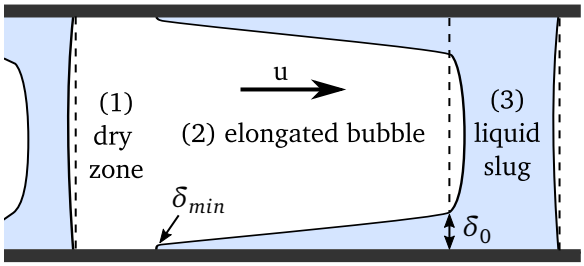

Figure 2.6: Illustration of microlayers in microchannels according to the three zone heat transfer model proposed by Thome et al. [148].

linearly from an initial thickness δ_0 at the border between zone (1) and (2) to a minimum thickness δ_{min} at the border of zone (3) and (1). Three parameters are needed to obtain a heat transfer coefficient, of which two concern the microlayer: δ_{min}, which was assumed to be in the same order of magnitude as the surface roughness, and a correlation factor needed for the calculation of δ_0, which was determined by a modified version of the correlation proposed by Moriyama and Inoue [109]. The rate of decrease in microlayer thickness is modeled to be driven solely by the input wall heat flux q, which is assumed to be constant over the channel length:

$$\frac{d\delta}{dt} = -\frac{q}{\rho_l \Delta h_v}. \tag{2.16}$$

Utaka et al. [155] determined the thickness of the microlayer with the laser extinction method. Microlayer thickness decreased linearly as the bubble passed the measurement location, supporting the linear profile shape assumed in the three-zone model. Furthermore, an increase in microlayer thickness with the velocity was seen. Han et al. [58] concluded from experimental measurements that the correlations for the film thickness derived for adiabatic systems, namely Equation 2.13 or Equation 2.15, are also suited for the calculation of δ_0 in experiments with evaporation. A similar conclusion is drawn in experimental studies by Srinivasan et al. [142] and Harirchian and Garimella [62]. The latter consequentially exchanged the modified correlations by Moriyama and Inoue [109] employed in the three zone model for Taylor's-Law. Simulations carried out by Magnini and Thome [103], however, showed excellent agreement of δ_0 with the correlation of Han and Shikazono [57] (Equation 2.15). The three-zone model was further developed by Magnini and Thome [102], who included the effects of sequential bubbles and fluid circulation studied by Magnini et al. [100, 101]. Zhang and Utaka [168] measured the microlayer thickness using the laser extinction method and developed a correlation for the microlayer thickness that depends on Ca, Bo and We.

Bigham and Moghaddam [8] resolved the thermal field underneath a moving bubble with miniature temperature sensors embedded in the rectangular channel wall, from which the local heat flux was calculated. Heat flux was highest across the microlayer and declined rapidly in the dry region. Sun

et al. [146] used the laser displacement method to measure the transient microlayer profile with water and observed that the microlayer thickness most often decreased much faster than when calculated with Equation 2.16, as assumed in the three-zone model. The authors account this discrepancy to local changes in the wall temperature, as measured by Bigham and Moghaddam [8], which lead to locally varying heat flux. The constant heat flux assumption of the three-zone model was further addressed in a numerical study by Okajima and Stephan [114], in which the evaporative heat flux is calculated from the temperature difference between wall and liquid-vapor interface. It is concluded that a linear temperature profile may only be assumed if the wall superheat is low. For high wall superheat, the film may be thicker than the thermal boundary layer, leading to a reduced contribution of the microlayer to overall heat flux. Furthermore, Okajima and Stephan [114] point out that an increased level of wall superheat leads to higher bubble growth acceleration and, therefore, limits the usability of Equation 2.13 or Equation 2.15.

Guo et al. [54] carried out similar measurements of the microlayer profile as Sun et al. [146] with water, ethanol, and FC-72. Microlayer thickness decreased fastest in FC-72, while water showed the most gradual decline, which was explained by their difference in enthalpy of vaporization and interfacial sheer. Furthermore, δ_0 followed Taylor's law (Equation 2.13) and showed no dependency on heat flux or wall superheat. As also observed by Sun et al. [146] and Okajima and Stephan [114], the measured microlayer lengths did not agree with the three-zone model.

A new empirical correlation for the microlayer thickness was proposed by Guo et al. [54] that agreed well with their own experimental data, as well as the results reported by Sun et al. [146]. The effects of channel geometry on the microlayer and heat transfer were studied by Ferrari et al. [34] using numerical simulation. In contrast to circular channels, the microlayer reduced quickly over the length of the bubble due to the additional drainage induced by the corners. Heat flux showed to depend highly on the thickness of the microlayer and reduced drastically when the bubble shape became axisymmetric.

Fischer [35] and Fischer et al. [36] studied the evaporation near the contact line of moving menisci in a vertical capillary slot and observed the formation of a microlayer for the receding case towards low ΔT and high u. An analytical model for the length of the microlayer was presented, in which the wall temperature was assumed constant. It was theorized that a microlayer forms if the mass flux toward the contact line exceeds the evaporation in this region.

2.2.3 Dip-coating

Similar liquid films to those described in the previous chapters are observed in the field of dip-coating. In this process a thin liquid film is deposited on a solid, usually a flat plate or a round fiber, by withdrawing it from a static pool of liquid. The expressions given in this chapter, however, are limited to the geometry of a flat plate. Film and microlayer formation in a dip-coating set-up is illustrated in Figure 2.7.

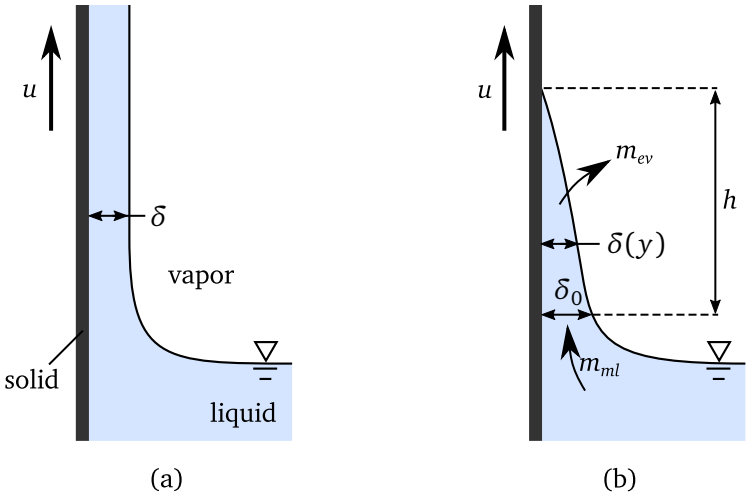

Figure 2.7: Illustration of film formation in a dip-coating set-up: (a) without evaporation, (b) with evaporation as described by Qu et al. [118].

Studies without evaporation

Fundamental work was carried out by Landau and Levich [94] and Derjaguin [23], who considered an infinitely long substrate and a perfectly wetting liquid. Motivated by the production of photographic film, the thickness δ of the liquid film remaining on the moving substrate far away from the stationary meniscus was analyzed. This situation is sketched in Figure 2.7a. The authors derived a relationship between δ and the capillary number Ca by matching the curvature of the meniscus with that of an almost vertical film, which is today regarded as the classic Landau-Levich-Derjaguin (LLD) relation

$$\delta = 0.946\, l_c\, \mathrm{Ca}^{2/3} \qquad \text{for } \mathrm{Ca} < 10^{-3}. \tag{2.17}$$

In addition, Landau and Levich give an expression for the mass of the fluid carried along with the slow moving substrate, showing that it is directly proportional to the velocity u to the power of $5/3$. As Ca is increased, the film becomes thicker and with it drainage due to gravity, which is neglected in Equation 2.17. Film thickness for very large Ca, the so called *visco-gravitational regime*, was first analyzed by Derjaguin [22] and the regime is hence also referred to as the Derjaguin regime. Here, Derjaguin obtained

$$\delta = l_c \sqrt{\mathrm{Ca}} \qquad \text{for } \mathrm{Ca} > 10^{3}. \tag{2.18}$$

The range of Ca in between the validity of Equation 2.17 and Equation 2.18, where both gravitational and capillary effects are of importance, is very broad [127]. White and Tallmadge [162] first acquired an expression for the film thickness within this intermediate regime by numerical integration of a linearized form of the full hydrodynamic problem:

$$\mathrm{Ca} = 1.09\,(\delta/l_c)^{3/2} + (\delta/l_c)^2. \tag{2.19}$$

Using a similar approach, White and Tallmadge [163] also gained an expression for the geometry of a cylinder, which is remarkably similar to Taylor's Law (Equation 2.13). The authors show the solution transfers into that of a flat plate if the radius of the cylinder becomes very large. A fully numerical solution was proposed by Ryck and Quéré [127]. The authors also discuss the importance of inertia, which has also been neglected above and can lead to a thickening of the deposited film above a velocity threshold. It is stressed that this is of particular importance to liquids of low viscosity, as a thickening can already be observed for $\mathrm{Ca} << 1$ and $\mathrm{Re} \approx 1$ for these fluids. Similar work was carried out by Jin et al. [77], who proposed that the exponent in Equation 2.17 approaches a value of 0.582 for $\mathrm{Ca} \to \infty$. The authors also observed the formation of a wavy but steady pattern of the liquid-air interface with increasing Re.

Studies with evaporation

As the dip-coating geometry is not directly connected with heat transfer applications, studies involving evaporation are rather scarce and largely deal with the preparation of coatings from volatile solutions, where a colloid is left on the moving substrate after the solvent has evaporated. As these studies focus on the coated colloid film, rather than the evaporating film itself, they are beyond the scope of this work and only one feature shall be mentioned here: Below some critical Ca_{dep}, colloid deposition is dependent on the evaporation near the contact line, while above Ca_{dep} it is dominated by the thickness of the deposited liquid film[3] [6, 7, 33, 78, 96]. As a result, the deposition of colloids and, therefore, the thickness of the colloid film, decreases with increasing velocity below Ca_{dep}, while it increases with increasing velocity above Ca_{dep}. Consequently, the thickness of colloids deposited on the solid reaches a minimum at Ca_{dep}.

Apart from studies concerning colloid deposition, to the best of the authors knowledge, the only generic experimental study of evaporating dip-coated films up to now was carried out by Qu et al. [118], who used pure volatile silicone oils to vary the rate of evaporation into an air atmosphere. This situation is illustrated in Figure 2.7b. While the initial thickness of the film δ_0 near the meniscus followed the LLD-Law (Equation 2.17), the stationary finite length of the film h scaled $h \sim \mathrm{Ca}^{5/3}$. In agreement with the analysis of Landau and Levich [94], the power of this scaling was also found for the mass flow entrained into the film m_{ml} and, consequently, the overall mass flow lost by evaporation m_{ev}. The profiles of the evaporating films were of similar shape and collapsed into a single profile when scaled by the identified power laws and the bulk evaporation rate. Furthermore, the contact angle at the end of the film, which was measured using laser interferometry, decreased with the velocity and increased with the evaporation rate. Lee and Son [97] studied evaporating LLD-films on a heated wall using numerical simulations, which showed good agreement with the scaling laws observed by Qu et al. [118]. While the wall temperature was assumed

[3] In the given references, this capillary number is also referred to as the critical capillary number, but renamed here to avoid confusion with Ca_{cr} discussed below.

to be constant, the gas-phase was also resolved, which showed a variation of the temperature along the liquid-gas interface.

2.3 The dynamic wetting transition

For perfectly wetting liquids, the LLD-Law (Equation 2.17) stays valid towards the limit of $\mathrm{Ca} \to 0$ up to very small δ, until instability effects driven by intermolecular forces become relevant [121]. For partially wetting liquids, however, a critical value dewetting velocity u_{cr}, generally described by a critical capillary number Ca_{cr}, exists, below which no film is deposited. This transition between moving contact line and film entrainment is thereby referred to as the *forced dynamic wetting transition*[4] and sketched in Figure 2.8. Derjaguin [24] and Blake and Ruschak [9] proposed that this transition occurs at a vanishing apparent contact angle $\theta_{app} = 0$, which is also implicitly included within the analysis of Landau and Levich [94]. The proposition is based on the meniscus rise, Equation 2.2, which reaches a maximum of $\Delta y_m = \sqrt{2} l_c$ for $\theta_{app} = 0$. If the dewetting velocity is increased further, a film of thickness δ emerges. This situation is sketched in Figure 2.8a. At the contact line, however, the contact angle remains equal to θ_e (micro angle approach). Quéré [119] studied the forced dynamic wetting transition experimentally using sliding plugs inside a capillary and found $\mathrm{Ca}_{cr} \sim \theta_e^3$. The same relation was subsequently also found for drops sliding along an inclined plane [120]. Mathematical analysis by Hocking showed that Ca_{cr} indeed depends on the equilibrium contact angle θ_e and the slip length l_{slip}. An expression for Ca_{cr} was first derived by Eggers [30, 31] using matched asymptotics. While Eggers assumed the angle between moving plate and liquid bath to be small, Chan et al. [13] adapted the analysis to derive an expression of Ca_{cr} for vertical withdrawal:

$$\mathrm{Ca}_{cr} = \frac{\theta_e^3}{9} \left[\ln\left(\frac{3^{1/3} \mathrm{Ca}_{cr}^{1/3} \theta_e l_c}{2^{5/6} 3\pi (\mathrm{Ai}(\mathrm{s}_{\max}))^2 l_{slip}} \right) \right]^{-1}, \tag{2.20}$$

where $\mathrm{Ai}(\mathrm{s}_{\max})$ describes the global maximum of the Airy function (0.53566...). l_{slip} is the slip-length needed to resolve the hydrodynamic singularity at the contact line within the micro angle approach. In Equation 2.20, it is assumed that inertia and gravity effects are negligible and that θ_e is small.

While a vanishing apparent contact angle, i.e. a maximum meniscus rise of $\Delta y_m = \sqrt{2} l_c$, at the onset of film deposition is experimentally supported [104, 133] and often assumed [13, 30, 31], film deposition has also been observed to occur before this condition was met [21, 69, 138]. Hocking [69] identified a velocity range below Ca_{cr}, where the receding motion of the contact line leads to a much slower film growth. Similarly, Snoeijer et al. [138] showed, both experimentally and theoretically, that a thickened ridge can form very close to the contact line, which is illustrated in Figure 2.8b. In this scenario, the onset of film deposition is not determined by a vanishing apparent contact angle, but by the relative velocity to the moving plate, i.e. the difference in velocity of the plate u and contact line at the top of the ridge u_r:

[4] This should not be confused with the *wetting transition*, i.e. the Cassie-Wenzel transition on rough surfaces.

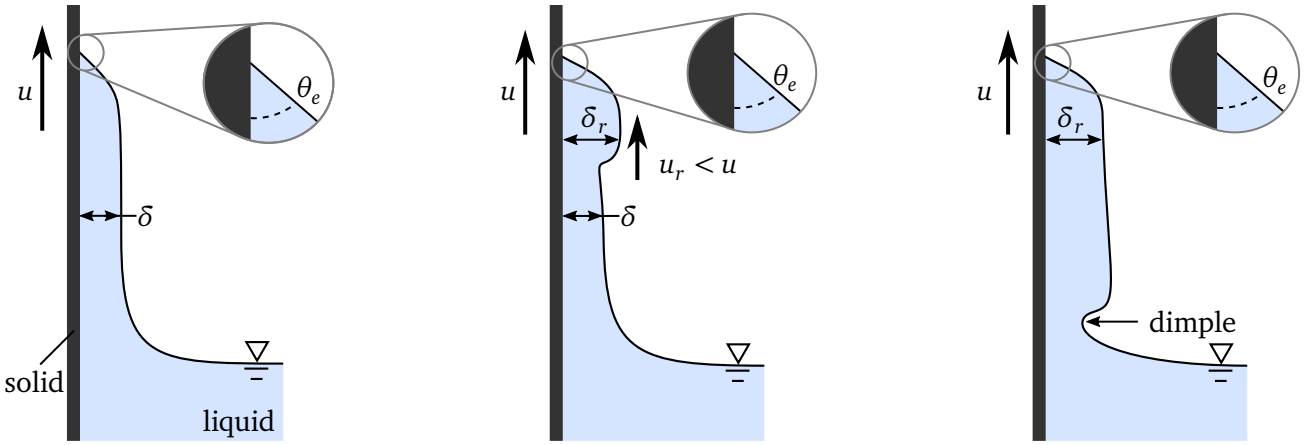

Figure 2.8: Illustration of the dynamic wetting transition of partially wetting liquids at $\mathrm{Ca} > \mathrm{Ca}_{cr}$: (a) film emergence according to classical conjecture of maximum meniscus rise. (b) film emergence determined by dewetting ridge of thickness δ_r [138]. (c) formation of a thick film for $\mathrm{Ca} \approx \mathrm{Ca}_{cr}$ [136].

$$\mathrm{Ca}_{cr} = (u - u_r)\frac{\mu}{\sigma}. \tag{2.21}$$

As u_r is smaller than u, liquid dragged upwards by the motion of the plate accumulates near the contact line, where a dewetting ridge of thickness δ_r forms. δ_r is thereby determined by θ_e and is also related to Ca_{cr}:

$$\mathrm{Ca}_{cr} = \frac{\delta_r^2}{3l_c^2}. \tag{2.22}$$

Ca_{cr} described by Equation 2.21 and Equation 2.22 is generally lower than Ca_{cr} inferred from the condition of vanishing contact angle and is, therefore, also referred to as *pre-critical* [138]. As the plate velocity is increased, the ridge is pulled upwards and the thinner film emerges, connecting the ridge with the meniscus. In the work of Snoeijer et al. [138], this thinner film followed the LLD-law. However, in a later work Snoeijer et al. [136] demonstrated that the appearance of the LLD-film can be entirely avoided if u remains very close to the receding velocity of the contact line. This situation is illustrated in Figure 2.8c. A film of thickness δ_r is deposited, which is connected to the meniscus by a dimple. As noted by Chan et al. [13], this behavior is not modeled by Equation 2.20 because gravity effects were neglected during the derivation of the latter. Further analysis by Ziegler et al. [169], and later by Galvagno et al. [41], suggested that the appearance of a ridge according to Equation 2.21 is omitted for low inclinations of the plate relative to the liquid bath, leading to the immediate formation of the LLD-film above Ca_{cr}. Numerical simulations carried out by Gao et al. [43] agreed well with the findings of Snoeijer et al. [136, 138], and showed that a film of homogeneous thickness could be obtained if the LLD-film reaches the thickness of the ridge. In contrast to the experiments, however, a meniscus rise of $\sqrt{2}l_c$ was found at Ca_{cr}, even though a ridge did form.

2.4 Conclusions of the literature review and objectives of the thesis

As can be seen from the literature review conducted above, microlayers themselves have been studied widely over the past decades. The formation process of the microlayer, however, remains unclear. This shortcoming is especially prominent in the field of nucleate boiling, where experimental and numerical evidence has been presented in favor of both the existence and absence of a microlayer. Recent numerical work suggests that a transition between the two modes of heat transfer, namely contact line evaporation and microlayer evaporation, might depend on the wall superheat, the bubble growth velocity, or the contact angle. However, this has not been experimentally explored, not least because these quantities are inherently linked with each other inside a growing vapor bubble. A fundamental investigation of the physical processes involved in microlayer formation using a boiling apparatus is, therefore, highly difficult.

Apart from the formation process, further shortcomings concerning the microlayer itself can be identified. A great number of studies and models analyze the heat flux caused by the microlayer, but both the shape of the heat flux profile and the overall amount are not reported uniformly across the literature. Possible reasons for this discrepancy, however, are still unclear but seem to include the influence of the liquid and solid material. Furthermore, while the thickness of the microlayer found in different heat transfer applications has been studied considerably, and experimental correlations are described in literature, the length of the microlayer has received far less attention.

Taking into account the similarities of both the liquid films and microlayers encountered across boiling, microchannels, and dip-coating, one can argue that microlayer formation can be seen as a dynamic wetting transition in the presence of temperature driven phase change. This conjecture has been discussed or implicitly assumed before, for example by Cooper and Lloyd [19] or Guion et al. [52]. Experimental evidence in support of it can be found in the velocity dependency of the microlayer observed by Sielaff [135] or Yabuki and Nakabeppu [165]. However, the effect of evaporation on the critical capillary number Ca_{cr}, especially through the effect of the evaporation induced contact angle, has not received much attention in literature. As a matter of fact, this is also overlooked in many numerical studies, where the contact angle imposed at the wall is often assumed constant. Consequently, understanding the interplay between evaporation and Ca_{cr} in a dip-coating configuration might also offer valuable insight into the microlayer formation in boiling processes. In addition, the dip-coating geometry allows for a decoupling of wall superheat and dewetting velocity and, therefore, for a more fundamental investigation of microlayer formation. The analytical expressions known for the dip-coating geometry thereby offer the opportunity to compare against experimental data. Some of the results presented in this work and published by Schweikert et al. [129] have recently been used by Bure and Sato [12] for the development of a correlation-based transitional criterion between contact line evaporation and microlayer evaporation in nucleate boiling, which is based on this conjecture.

Considering the paragraphs above, the aim of this thesis is the experimental investigation of microlayer formation and evaporation through the means of dip-coating. The specific objectives can be summarized as

follows:

- Investigation of the role of wall superheat, dewetting velocity, and contact angle on the transition between contact line evaporation and microlayer evaporation.
- Analysis of the heat flux within both regimes, from which influential parameters are to be identified.
- Analysis of the length and thickness of the microlayer.
- Interpretation of the results in the context of boiling heat transfer.

To accomplish these objectives, an experimental facility is constructed, in which highly controlled dewetting experiments of a heated wall can be conducted within a pure vapor atmosphere. Wall superheat, dewetting velocity, and film shape have been identified as key parameters of interest, which need to be measured during the dewetting process. From the field of boiling research, infrared thermography is found to be a suitable measurement technique for the determination of wall temperature and heat flux, while it has been shown that the microlayer thickness can be accurately determined by the means of interferometry.

CHAPTER 3

Methods of investigation

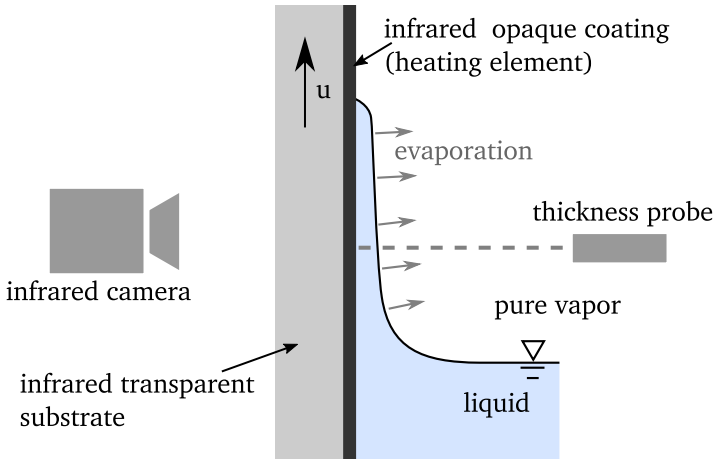

Figure 3.1: Overview of the experimental principle.

From the scientific goals defined in section 2.4, the key requirements for the experimental facility can be summarized as follows:

- The dewetting velocity u and the wall superheat ΔT can be independently varied.
- Measurement of the local wall temperature.
- Measurement of the microlayer thickness.
- Pure substance and vapor atmosphere for the comparison with boiling studies.

Most of these requirements are achieved by a dip-coating set-up, i.e. a sample being drawn from a stationary pool of liquid. Furthermore, in such a set-up the dynamic meniscus region remains stationary with respect to the measurement equipment. This offers several experimental advantages over the meniscus moving through the measurement location, because the latter highly limits the duration of the experiment. In literature, infrared thermography has been demonstrated to be most suitable for the measurement of the temperature at the solid-liquid interface, deduction of the local heat flux, and calculation of the local

microlayer thickness, for example in [35, 36, 81, 86, 85, 135]. Hence, it shall be applied in this study. Since the thickness calculated from infrared measurements has been shown to carry possible errors [81, 49], a one-dimensional interferometric thickness probe is used as a means of validation.

A withdrawing plate experiment adapted for these measurement techniques is sketched in Figure 3.1. The wall consists of an infrared transparent substrate, which can be moved out of the liquid pool with the velocity u. The substrate is coated with an infrared opaque layer, which serves as a joule heater and an emissive surface for the infrared thermography. Unfortunately, two main issues arise when combining infrared thermography and the withdrawing plate method: First, in a classical withdrawing plate method both sides of the sample are covered by the liquid it is withdrawn from. To ensure accurate infrared thermography, however, the backside of the sample has to be kept dry, or the liquid would otherwise obscure the view of the infrared camera. This problem is addressed through the design of the test-cell presented in section 3.1.1. Secondly, a conventional calibration method of the infrared camera requires that the relative position of the sample and infrared camera does not change during the measurement. Therefore, a novel calibration routine developed within the frame of this work is presented in section 3.2. The deduction of the local heat flux and analysis of the measurement data are described in section 3.3 and section 3.4, respectively. Measurement uncertainty is discussed separately in section 3.5.

3.1 Experimental method

Keeping the back of a moving sample dry, while the front side is being dewetted, proved to be a major challenge during the design of the experimental set-up, because applying this constraint directly to the purely linear motion of the withdrawing plate method is tied to major constructional difficulties. Naturally, this obstacle can be avoided by moving the liquid instead, as done for example in microchannels, which allows both sides of the sample to be easily sealed, as the sample itself is not in motion. On the contrary, the contact line velocity cannot be controlled and determined as accurately as using the withdrawing plate method because the bulk fluid has to be moved by a pressure difference. These features, however, were evaluated to be of high importance for examining the scientific questions asked in this work. To overcome the challenge of sealing both sides of a moving sample, the purely linear sample motion was compromised and changed to a circular path, which can easily be sealed using a conventional shaft seal.

3.1.1 Design of the test cell

A sketch of the test cell is given in Figure 3.2, while a detailed view into the test cell is shown in Figure 3.3. The sample (1) is mounted eccentrically onto a central disk (2), which is sealed by a shaft seal (3) made of polytetrafluoroethylene (PTFE). Side (A) of the test cell is filled with the test liquid (4) precisely to the diameter of the cell, while the back of the disc, side (B), remains dry. A wetting situation on the sample is caused by a clockwise rotation of the central disc, while a dewetting situation is achieved through

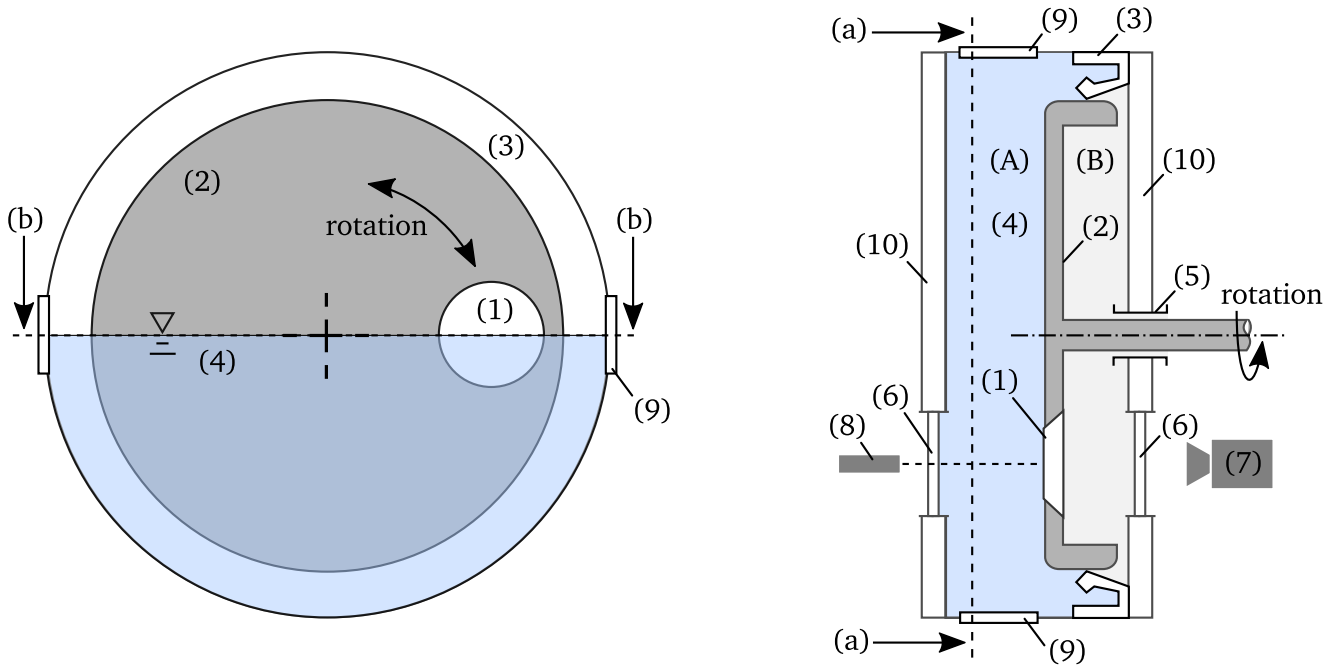

(a) front view

(b) top view

Figure 3.2: Sketch of the test cell: (1) sample, (2) central disc, (3) shaft seal, (4) liquid, (5) rotary feed through, (6) CaF_2 window, (7) infrared camera, (8) interferometric thickness sensor, (9) glass window, (10) thermalisation channels.

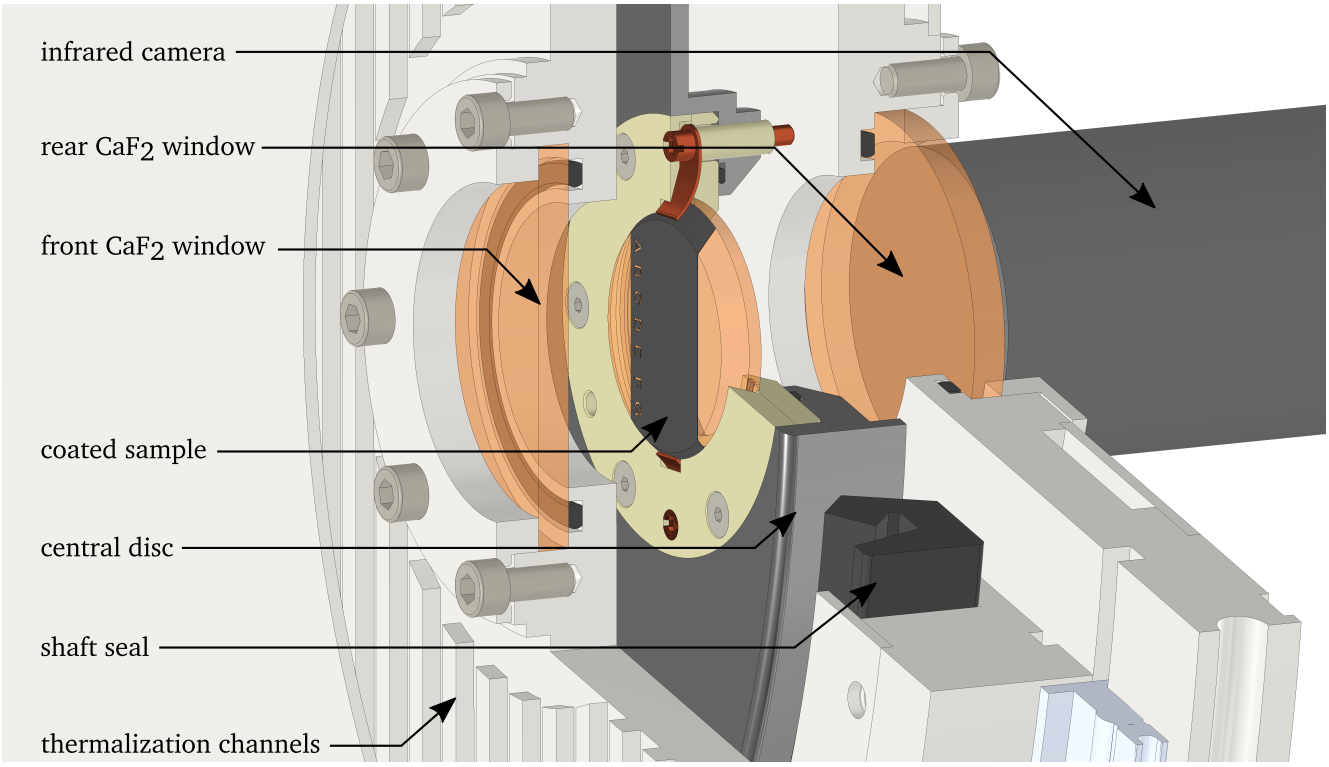

Figure 3.3: Break out view of the test cell showing the major components.

anticlockwise rotation (see Figure 3.7 below). As the distance from the rotational axis to the center of the sample is much larger than the horizontal area of interest on the sample (113 mm and 1 mm, respectively), vertical movement of the sample is approximated. For rotation of the central disc, a shaft located on the axis of rotation is transferred to the outside of the test cell by a vacuum feed through (5). An electrical connection between the central disc and the stationary environment is established by a high performance slip ring located inside of the test cell on the axis of rotation. This allows the sample to be heated by an external power source through joule heating, even when the sample is in motion. Two infrared transparent windows (6) made from calcium fluoride (CaF_2) provide optical access to the front and back of the sample. This access is used by the infrared camera (7) and the interferometric probe (8). The distance between the surface of the sample and the front CaF_2 window is 10 mm. Additional glass windows (9) allow visual access to the (de-)wetting process from the sides. The temperature of the test cell is controlled by a temperature controlled fluid cycle, which is connected to thermalisation channels (10) built into the walls of the test cell. To enable measurements in saturated conditions, vacuum grade components are chosen for construction.

3.1.2 Periphery and measurement devices

A photo of the opened up test cell including the piping and periphery in its immediate surroundings is shown in Figure 3.4. A process diagram of the whole experimental set-up is sketched in Figure 3.5. In contrast to the sketch of the test cell in Figure 3.2 above, the test cell in the process diagram is viewed from the side. Manufacturer and model details of any electronic equipment mentioned in this section is given in the appendix in Table A.1.

The central disc is rotated by a high accuracy brushless rotary motor (1) connected to a planetary gear box to increase motor torque. While the chosen motor type is very similar to a stepper motor, smooth velocity profiles are obtained because it does not make use of finite steps. The pressure on each side of the central disc is measured by a pressure transducer and can be equalized through external piping. The piping includes sections of flexible tubing to allow the test cell to be opened. The liquid level on side (B) is monitored through a level indicator (2) and a gear pump transfers any condensed or leaked liquid from side (B) back to side (A). A storage tank (3) is directly connected to the test cell, and is used to store the degassed liquid and for filling the test cell. The temperature within the test cell is measured by a total of six Pt-1000 temperature sensors, three above and three below the liquid fill hight of side (A), distanced approximately 1 mm orthogonally from the surface of the moving sample. The analog signals of the temperature and pressure sensors are read by a source measure unit (4). A dynamic temperature control unit (5) is used to control the temperature within the test cell through a fluid heating/cooling cycle. As shown earlier in Figure 3.3, the heat exchanger for this heating/cooling cycle is implemented directly within the walls of the test cell on side (A) and (B). A dedicated condenser is not needed, as the amount of fluid evaporated at the heated sample during the experiment is very small and can thus recondense within the test cell.

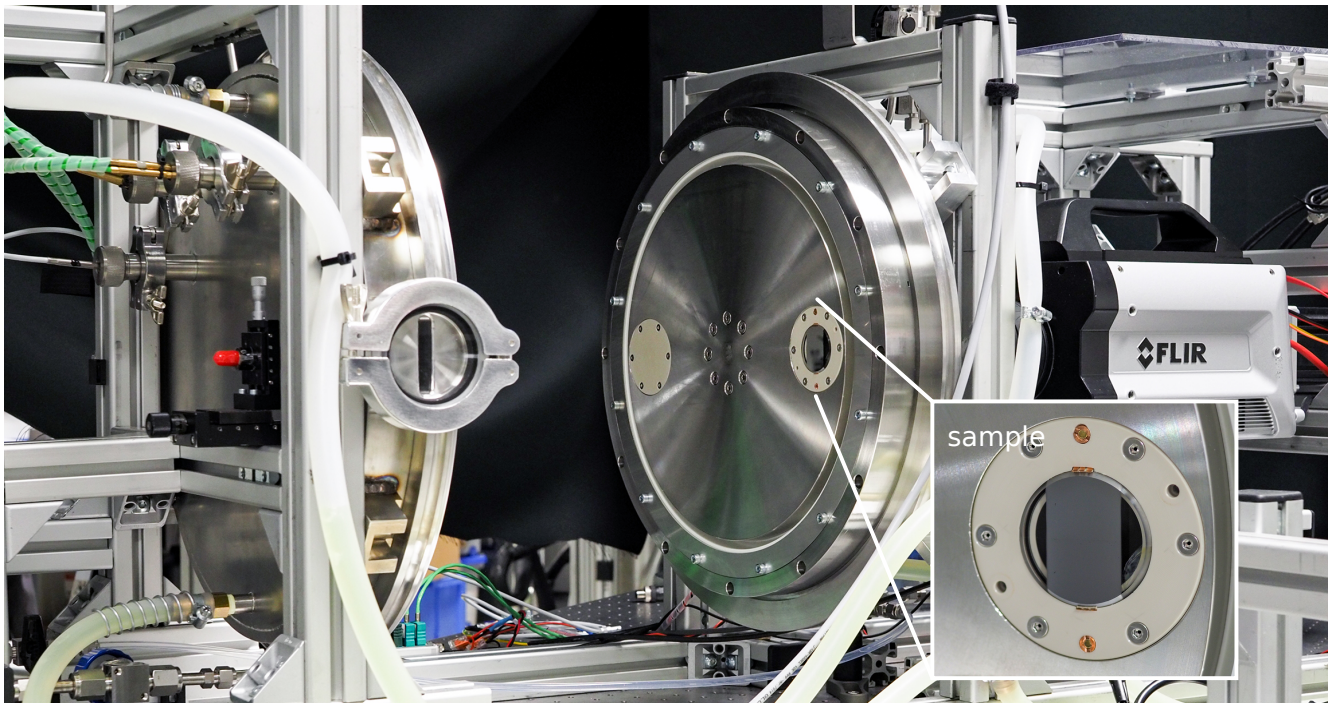

Figure 3.4: Photo of the experimental test cell (opened up).

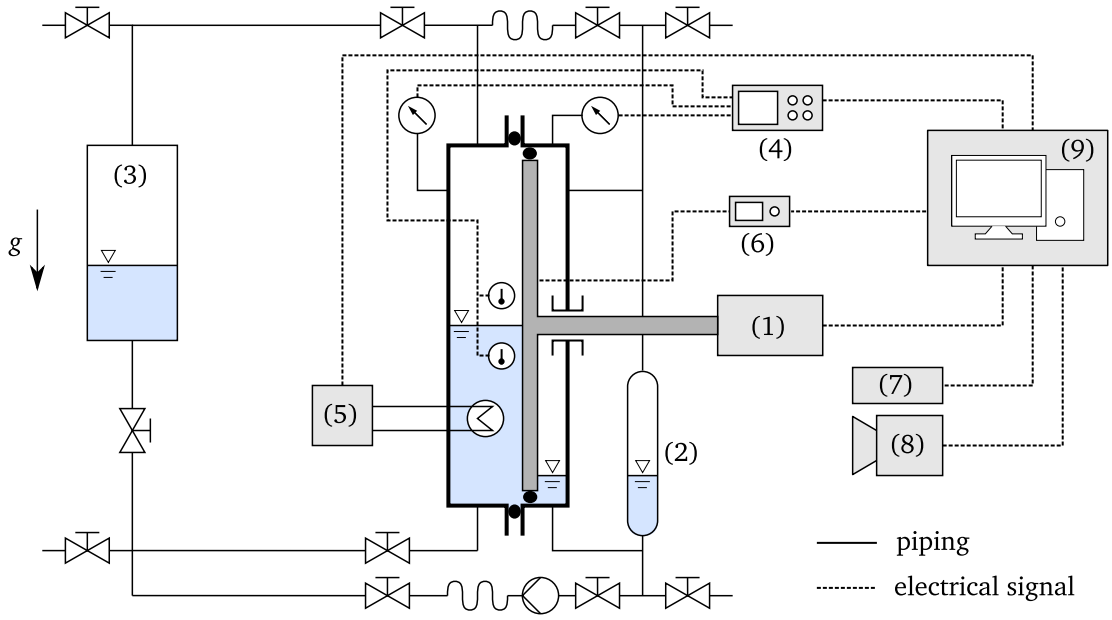

Figure 3.5: Process diagram of the experimental setup: Motor (1), level indicator (2), storage tank (3), source measure unit (4), temperature control unit (5), sample heater power source (6), interferometer (7) and infrared camera (8) and computer system (9).

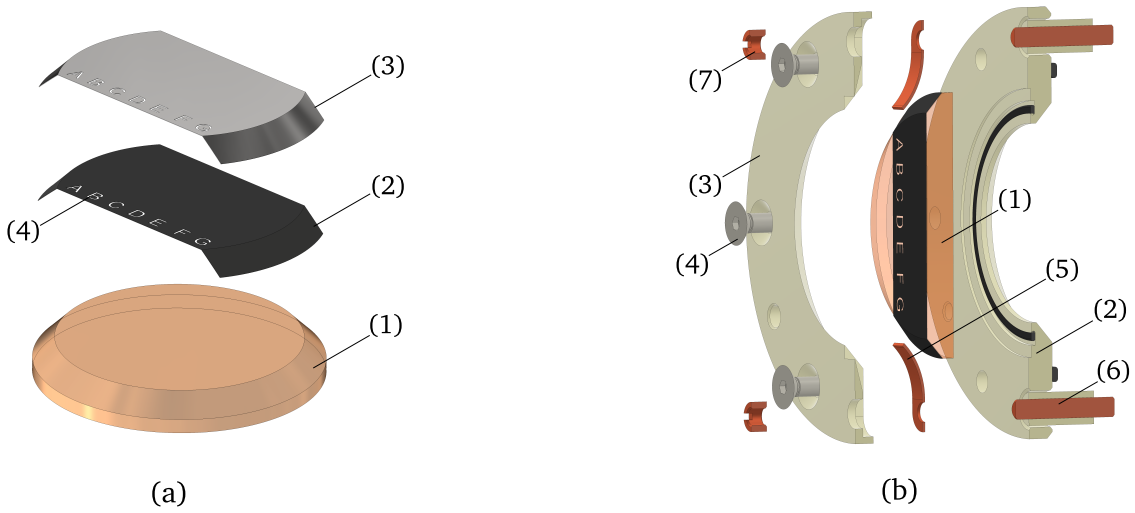

Figure 3.6: (a) Illustration of the samples design with (1) CaF_2 carrier substrate, (2) 500 nm CrN coating, (3) 500 nm Cr coating, (4) markings. (b) Sample holder and electrical connections with (1) sample, (2) bottom holder, (3) top holder, (4) screws, (5) copper spring contacts, (6) supply contacts, (7) nut

Motor (1), source measure unit (4), temperature control unit (5), sample heater power source (6), interferometer (7) and infrared camera (8) are connected to a computer system (9), which controls the measurement process and records all measurement data.

3.1.3 Samples and fluids

The design of the samples is adopted from Fischer [35] and is shown in Figure 3.6a. All samples consist of a carrier substrate (1), which is 40 mm in diameter and 5 mm thick. The top edge of the substrate carries a 3 mm wide chamfer, which is used to secure the sample within the sample holder. The carrier substrate is made of infrared transparent calcium fluoride (CaF_2), whose material properties are listed in Table 3.1. The carrier substrate is sputter coated with two metallic layers, each approximately 500 nm in thickness. The first layer (2) is made of chromium nitrate (CrN) and enhances the signal quality received by the infrared camera due to its high emissivity within the observed spectrum. The second layer (3) is made of pure chromium (Cr), which is used for joule heating and also improves the overall mechanical stability of the double layer. The width of the coating is 20 mm. A detailed discussion of the fabrication process and the properties of the coatings can be found in [111]. Thin markings (4) are manually worked into the coatings for optical position detection, which is further explained in section 3.2.

The sample holder is illustrated in Figure 3.6b. It consists of two parts: The sample (1) is placed into the bottom holder (2). An O-ring between sample and bottom holder thereby prevents leakage between both sides of the sample. The seal is pressurized by the top holder (3), which is pressed onto the chamfer of the substrate by screws (4) directly screwed into the central disc (not shown). Copper spring contacts (5) between top and bottom holder establish an electrical connection between sample and the supply

Table 3.1: Material properties of calcium fluoride (CaF_2) at 25 °C.

ρ_s in kg/m^3	λ_s in W/mK	$c_{p,s}$ in J/kgK
3180	9.71	854

Table 3.2: Fluid properties of ethanol [98] and FC-72 (perfluorohexane, C_6F_{14}) [115] at 25 °C.

	p_{sat} in kPa	μ in kg/ms	ρ_l in kg/m^3	σ_l in N/m	Δh_v in kJ/kg	λ_l in W/mK	$c_{p,l}$ in kJ/kgK
ethanol	7.89	1.0817×10^{-3}	785.05	21.93×10^{-3}	920.67	163.45×10^{-3}	2.4346
FC-72	32.4	0.647×10^{-3}	1684.44	11.115×10^{-3}	93.102	55.844×10^{-3}	1.0396

contacts (6), which are embedded into the central disc. Top and bottom holder are made from polyether ether ketone (PEEK) to provide electrical isolation between sample and test-cell. The contacts are secured by a nut (7). Put together, the sample's coated surface extends 1 mm above the top holder, which is in turn flush with the surface of the central disc. This is done to reduce any possible disruptive effects of the sample holder on the fluid dynamics close to the measurement area and allow observation of the dynamic meniscus from the side through the windows (9) in Figure 3.2. While the latter is indeed possible, the resolution of the measurement data was not sufficient to provide any relevant additional information, and is hence not further discussed throughout this thesis.

Ethanol (C_2H_6O) and the refrigerant FC-72 (perfluorohexane, C_6F_{14}) are used as test fluids. For both fluids, an equilibrium contact angle on the smooth chromium surface (roughness $R_a < 0.05\,\mu$m) could not be obtained ($< 10°$) in a sessile drop experiment under atmospheric conditions. Therefore, both fluids are assumed to perfectly wet the chromium surface in equilibrium. The material properties of both ethanol and FC-72 are given in Table 3.2.

3.1.4 Experimental procedure

Before each set of experiments, the cell is thoroughly evacuated and then filled with the test liquid by expansion into the low-pressure atmosphere of the cell, where the liquid condenses on side (A). Non-condensable gases are removed with a vacuum pump, while the liquid is further degassed by boiling within the test cell. This process is repeated until the pressure of the cell equals the vapor pressure of the fluid to ensure a pure vapor atmosphere. The liquid level is adjusted so half of the central disc is covered with liquid. The cell is then heated until temperature and pressure are stationary. All experiments presented in this thesis are conducted at a cell temperature of 25 °C. Before starting a set of experiments, the measurement location of the interferometric sensor is placed by lowering the sensor towards the liquid pool until a reading is achieved. During this process, the sample is heated to ensure that it is completely dry above the contact line. The senor is then raised by 1.5 mm. This is done to ensure measurement above the dynamic meniscus region and to increase comparability of the measurements.

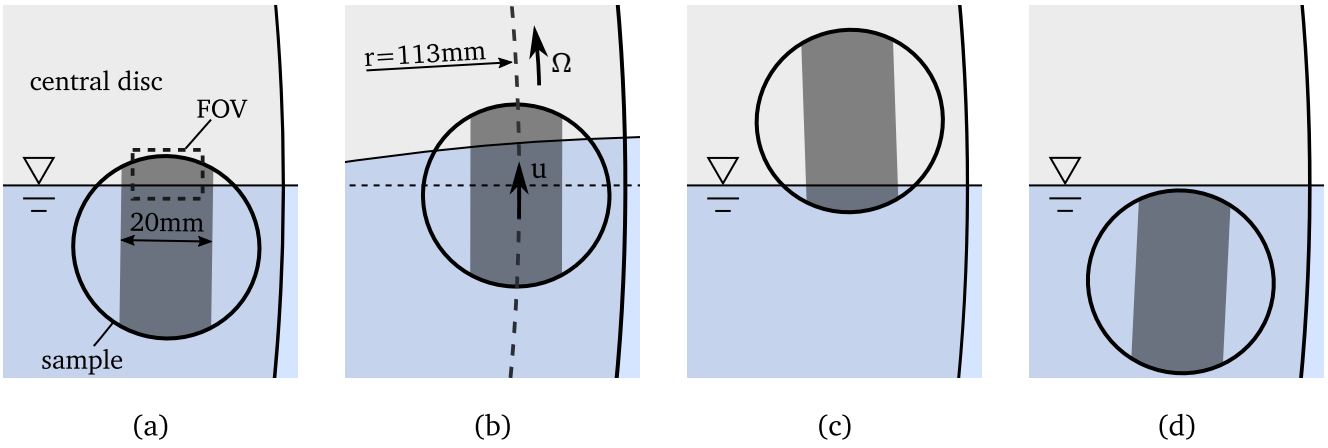

Figure 3.7: Sketch of the sample position during the measurement: (a) Initial position during heating phase. (b) Rotation of disc with angular velocity Ω causes dewetting of the sample with velocity u and microlayer formation. (c) Maximum height of the sample above the liquid pool after movement. (d) Complete immersion of the sample.

The measurement process is sketched in Figure 3.7. Please note, that the depicted tilting of the sample during the dewetting process is exaggerated, as the sketch is not to scale. However, the actual amount of tilt does contribute to measurement uncertainty, which is discussed in section 3.5. The sample is lowered into the liquid pool by clockwise rotation of the central disc until only the very top remains above the liquid surface, as shown in Figure 3.7a. The sample is not lowered further to ensure that the top edge of the sample does not influence the formation process of the microlayer. A voltage is then applied to the coating to heat the sample by joule heating. Different magnitudes of wall temperature are achieved by altering the duration and magnitude of the current that is run through the coating. The heating duration is precisely timed to achieve comparable levels of wall temperature between experiments.

The voltage is then turned off and the disc rotated in anticlockwise rotation with the angular velocity Ω, as shown in Figure 3.7b. Hence, the sample is moved out of the liquid with constant velocity u. Microlayer formation can occur during this phase. The movement is continued until only the very bottom of the sample remains inside the liquid. This state is shown in Figure 3.7c, where it is held for a few seconds. The sample is not moved upwards any further to also capture the contact line both during and after the collapse of the microlayer in the infrared recordings. Afterwards, the sample is lowered below the liquid surface through clockwise rotation of the central disc, as shown in Figure 3.7d.

The sample is then returned to its initial position, shown in Figure 3.7a. Before starting the next experiment, the sample is given sufficient time to return to ambient temperature. The whole measurement process described above was fully automated to ensure a high level of reproducibility.

3.2 Infrared calibration

The calibration approach developed for this thesis, and described in the following section, has already been published by the author (Schweikert et al. [130]). Therefore, the following is limited to the application of the calibration approach to the experimental facility used within this work. A more general context and a detailed discussion on influential factors, computational considerations, and achievable measurement uncertainty can be found in the original publication [130]. The measurement uncertainty achieved with the calibration method in this work is assessed in section 3.5.

In infrared thermography, an object's temperature is obtained by measuring the intensity of the thermal radiation emitted by it. The conversion from the measured intensity values I to temperature values T is referred to as the calibration process, which largely determines the uncertainty in T. Best results are generally obtained by a so called *in situ* calibration of the sensor and sample [135]. In this method, a sufficient amount of reference measurements are taken at known sample temperatures, which should include values both below the minimum and above the maximum sample temperature anticipated in the actual experiments. These measurements are then fitted to a suitable equation, for example Equation 3.1 [135]:

$$T = c_1((I + c_2)^{1/4} + c_3) \tag{3.1}$$

After the constants c_1, c_2, and c_3 have been determined from the reference measurements, Equation 3.1 can be used to calculate T in further measurements. As the infrared camera uses a sensor array, the described fitting procedure is carried out for each pixel. It is important to note that this *pixel-wise in situ* calibration requires the relative position between sensor and sample to remain the same throughout the calibration procedure and measurements. Otherwise, inaccurate results could be obtained due to both the spacial inhomogeneity of the sample's emissivity and changes in the scene itself, such as background or scatter radiation. This requirement makes it impossible to directly apply the pixel-wise in situ calibration technique to the experimental facility used in this work, where the sample is in motion during the experiment. As the sample follows a fixed path, however, the relative position between sample and sensor, χ, can be reproduced. Therefore, if χ can be measured with sufficient accuracy during both the calibration and the experiments, it can be used to link between them.

The approach described above is illustrated in Figure 3.8, where χ is shown for all frames F of a hypothetical measurement. Assuming an in situ calibration performed at a discreet position χ_i is also valid for small shifts in χ, i.e within the discrete calibration interval $\Delta\chi_i$, then all frames within the interval ΔF_i can be calibrated. Another in situ calibration performed at χ_{i+1}, valid within $\Delta\chi_{i+1}$, can then be used to increase the amount of the calibratable frames. Consequently, the entire duration of the measurement can be calibrated if the whole distance $\chi_{max} - \chi_{min}$ is discretized into N intervals, for which a unique in situ calibration is performed each.

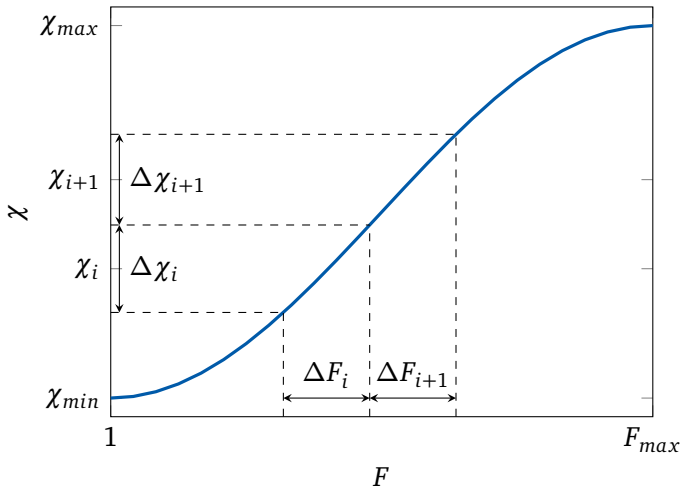

Figure 3.8: Relative position χ over all frames F of a hypothetical measurement. An *in situ* calibration performed at χ_i valid within $\Delta\chi_i$ can be used to calibrate frames within ΔF_i.

The accuracy in χ needed for this approach to work, however, is difficult to achieve with additional external sensors, like a high resolution incremental encoder placed on the axis of rotation, because a high degree of synchronization between sensor and infrared camera would be required. To avoid this, χ is determined directly from the infrared recordings using a correlation approach with sub-pixel accuracy. This method is described in the next section, followed by the description of the calibration procedure.

Movement detection by 2-D auto-correlation

The similarity between two images can be expressed by their Pearson correlation coefficient P. A value of unity indicates maximum similarity, which is found when the image is correlated to itself. Consequently, two recordings can be correlated with each other by calculating P for every pair of frames between them. If the two correlated recordings are identical, i.e. a recording is correlated to itself in this manner, the resulting function is called the *auto-correlation* function P_a of this recording. Naturally, P_a is a matrix of size $F_{max} \times F_{max}$. Therefore, the auto-correlation function of a single frame F_1 with all other frames in the recording is indicated by P_{a,F_1}. This frame F_1 is thereby referred to as the *center frame*, because the auto-correlation function P_{a,F_1} reaches unity at this point, $P_{a,F_1}(F_1) = 1$.

In the case of infrared recordings, P_a can deviate from unity due to local temperature changes, changes of the scene due to sample motion, and due to noise effects. A change in P can, therefore, be used to detect one of these effects if it is ensured that its magnitude is significantly higher than that of the other two effects. As the goal is the detection of sample motion, two measures are taken: Firstly, distinct markings are worked into the coating of the sample near the edge of the field of view (FOV), as mentioned in section 3.1.3. These markings cause a sharp change in local emissivity, through which the effect of motion on P is enhanced. Secondly, a two dimensional high-pass Butterworth filter is applied to the images before correlation to dampen the effects of temperature changes on P. The filtering process is shown in Figure 3.9.

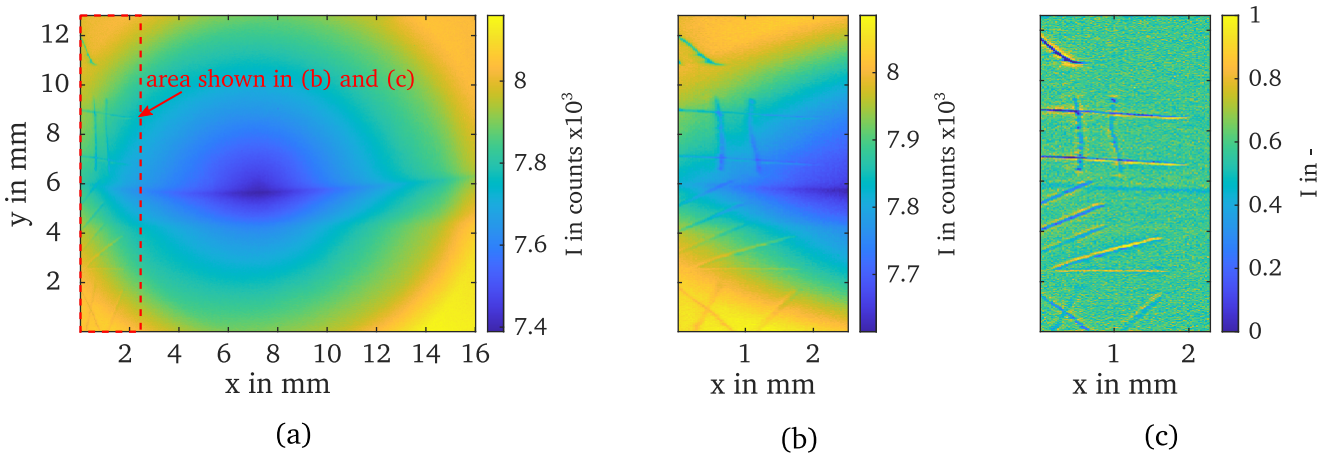

Figure 3.9: Filtering process: (a) whole uncalibrated and unfiltered FOV, (b) unfiltered markings on the left of the FOV, (c) image shown in (b) after the filtering process.

An unfiltered and uncalibrated image taken from a measurement of a superheated dewetting process is shown in Figure 3.9a, where the markings are visible on the left of the FOV. Only the area around the markings, which is shown in Figure 3.9b, is used for the filtering and correlation process. In addition to the markers, local changes in I due to temperature are visible. The filtered image is displayed in Figure 3.9c. While the sharp edges of the markings are enhanced, the more gradual changes due to temperature and vignetting are less pronounce. In addition, the image is normalized, through which the correlation of images with different base temperature value is improved. This is especially important during step 3 of the calibration process described in the next section.

Two auto-correlation functions of filtered frames are shown in Figure 3.10. Both describe the correlation of one single arbitrary frame (the center frame) with all frames F of an arbitrary measurement. $P_{a,sta}$ is taken from a static measurement, where χ remains constant during the measurement. In contrast, $P_{a,mov}$ is taken from a measurement, where the sample is in motion and χ changes during the measurement. $P_{a,sta}$ and $P_{a,mov}$ show a distinct difference in their behavior with increasing distance away from the center frame ($F = 350$ for $P_{a,sta}$ and at $F = 250$ for $P_{a,mov}$): $P_{a,mov}$ quickly decreases and resembles a Gaussian distribution, which is caused by the motion of the sample changing the appearance of the infrared image. The maximum height of the Gaussian distribution P_G (excluding the peak at the center frame) is thereby determined by the change in χ in between frames, i.e. by the sample velocity and the frame rate of the infrared camera. In contrast, $P_{a,sta}$ stays high for all F, only showing slight variation.

Since both χ and T are constant in the case of $P_{a,sta}$, the decrease from unity to approximately $P_{noise} = 0.8$ must be entirely caused by noise. Consequently, a value below this noise limit P_{noise} indicates that χ has changed between two frames. Please note that the given value for P_{noise} is not generic, because it depends on, for example, the experimental set-up, the infrared camera, the integration time, and the temperature of the sample. Therefore, P_{noise} is determined for each measurement individually.

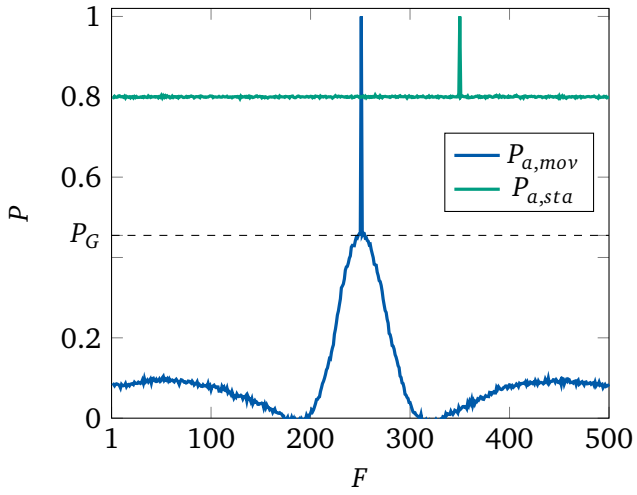

Figure 3.10: Comparison of the auto-correlation function of a static measurement $P_{a,sta}$ to that of a measurement, where the sample is in motion $P_{a,mov}$.

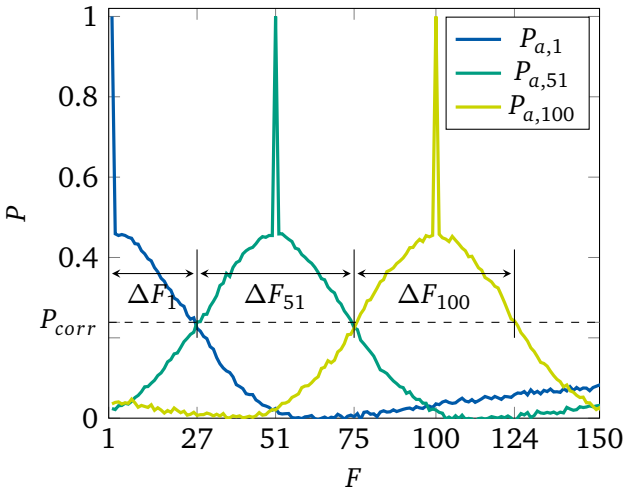

Figure 3.11: Illustration of the discretization process by auto-correlation.

Discretization procedure

Figure 3.11 illustrates how the sample movement is divided into N discrete positions χ_i using the auto-correlation function P_a. A sequence at $T = const.$ is chosen and a correlation limit $P_{corr} < P_G < P_{noise}$ is set. Please note that the displayed frames only correspond to a fraction of the distance between χ_{min} and χ_{max}. For each frame F in the sequence, the correlation width ΔF describes the number of adjacent frames for which $P > P_{corr}$ is true. Assuming that temperature effects on P can be neglected as discussed earlier, the continuous distance χ is discretized into N discrete positions χ_i as follows:

Starting with the first frame $F = 1$, all images within ΔF_1 are allocated to the first position $\chi_1 = \chi_{min}$. All frames within ΔF_1 are merged by calculating their mean, resulting in one single *position reference image* U_1 representing χ_1. U_2, representing χ_2, is obtained by locating the next frame in the sequence, whose correlation width is adjacent to that of ΔF_1. In the example given in Figure 3.11, this is true for $F = 51$. Therefore, all frames within ΔF_{51} are allocated to position χ_2, from which U_2 is calculated as above. The image representing the following position χ_3 is produced in the same manner, i.e. from the mean of all frames contained within ΔF_{100}.

The process described above is continued until all images within the sequence are accounted for. Consequently, if the chosen sequence contains a continuous motion between χ_{min} and χ_{max}, the movement path is discretized into N intervals, which are each represented by one U_i. With increasing correlation limit P_{corr}, the size of the discrete intervals $\Delta\chi_i$ become shorter, and the movement between χ_{min} and χ_{max} is represented by more images. The amount of these images N is, therefore, also referred to as the *resolution of the calibration*.

Calibration procedure

The whole calibration routine consists of six consecutive steps, which are outlined below:

1. Data collection at constant reference temperatures $T_{ref,n}$
   Side (A) of the test cell is completely filled with liquid and is homogeneously heated to a chosen reference temperature $T_{ref,n}$, where n is the index referring to a specific level of $T_{ref} = const.$. When the temperature of the facility has reached steady state, the sample is slowly moved (0.72 mm/s) between χ_{min} and χ_{max}, while the infrared camera is continuously recording. The distance between χ_{min} and χ_{max} is thereby resolved by approximately $15{\times}10^3$ frames in one recording sequence and direction of movement. The sample is repeatedly moved back and forth between χ_{min} and χ_{max} until approximately $120{\times}10^3$ frames have been accumulated. This procedure is repeated for five different temperatures $T_{ref,n}$ ($n = 1$ to 5) ranging from 23 °C to 35 °C for FC-72 and 23 °C to 38 °C for ethanol.

2. Creation of the position reference images U
   An arbitrary sequence from step 1 including the continuous movement between χ_{min} and χ_{max} is chosen and discretized as described earlier to create the position reference images U. P_{corr} is iteratively adjusted to result in a resolution of $N = 1000 \pm 2$.

3. Creation of the temperature reference images V
   All frames recorded in step 1 are cross-correlated to U to determine their χ_i, which is found by locating U_i in U with the highest correlation. All images sharing the same χ_i and $T_{ref,n}$ are merged by calculating their mean, which results in one *temperature reference image* $V_{i,n}$ for each $T_{ref,n}$ and χ_i. Thus, as a total of five reference temperatures were chosen in step 1, five temperature reference images now exist for each of the $N = 1000$ positions χ_i. It is ensured that at least 40 frames are used for the calculation of each V_i, while the median is approximately 100 throughout each calibration.

4. Determination of the calibration coefficients c
   Using V, a pixel-wise calibration is performed for each position χ_i by fitting the intensity values of $V_{i,n}$ and their corresponding temperature values $T_{ref,n}$ to Equation 3.1 using a least squares approach. As this is done for every pixel and every position, the coefficients c_1, c_2 and c_3 are discrete functions of x, y, and i.

5. Creation of the calibration reference images W
   All images within V sharing the same position χ_i, but different $T_{ref,n}$, are merged into one image by calculating their mean. While the resulting *calibration reference images* W are very similar to the position reference images U, the overall measurement uncertainty is reduced when using W instead of U for position detection in the following step 6 of the calibration procedure. This is explained by slight errors and non-uniformities in χ that can occur during the creation of V and which are directly passed on to the calibration coefficients. Since these errors are not present in U, χ_i calculated using U and W can differ. Therefore, using W for the determination of χ ensures maximal geometrical agreement with the calibration coefficients and in turn lower measurement uncertainty.

6. Calibration
   A frame is calibrated by first cross-correlating it to W in order to determine χ_i. Once χ_i is known for each frame, the measured intensity value of each pixel within each frame is related to a temperature value by using Equation 3.1 and the coefficients determined in step 4. The temperature values obtained with this method are referred to as T_{IR} in the following.

3.3 Heat flux calculation

The heat flux q through the solid-liquid/solid-gas interface, i.e. the coated surface of the sample where the microlayer is formed, is computed using numerical simulations. The temperature data measured by the infrared camera is used as a boundary condition to calculate the temperature distribution within the solid sample, from which the boundary heat flux is deduced. Computations are carried out in Comsol Multiphysics 5.6 (Build 280). The numerical method presented in this section has previously been published by the author (Schweikert et al. [131]).

A calibrated measurement of the local temperature distribution T_{IR} measured by the infrared camera is shown in Figure 3.12. The temperature field is sufficiently homogeneous in x-direction across the FOV and analysis is, therefore, only carried out within a narrow area located in the center of the FOV. Hence, the problem is reduced to two dimensions. A time dependent temperature vector is thereby gained by averaging the data in x-direction within $\Delta x = 1\,\mathrm{mm}$ (40 pixels). The size of Δx was chosen to sufficiently reduce temporal noise through the averaging process, while remaining small enough to ensure small measurement uncertainty in u. The computational domain including the grid and boundaries is shown in Figure 3.13. The coating of the sample is not resolved but neglected in the calculations due to its marginal thickness. Thus, the sample is modeled as a pure CaF_2 substrate at 25 °C. Detailed information about the computational grid and the boundary conditions (BC) is given in Table 3.3. The time dependent temperature data obtained by averaging within Δx is placed as a boundary condition on the boundary B1. The temperature distribution cannot be calculated for the whole sample at once because measured temperature data is only available within a small portion, which is currently being observed within the FOV. Therefore, only this portion of the sample is discretized. The vertical movement of the solid sample is accounted for by assuming a homogeneous convective flow in y-direction within the computational domain. The energy equation, Equation 3.2, is solved for each cell and time step t:

Table 3.3: Cell size and boundary conditions of the computational area

boundary	cell size in µm	thermal BC	convective BC
B1	12.5	$T_{IR}(y,t)$	$u_y = u; u_x = 0$
B2, B3	≤ 400	$\nabla T = 0$	$u_y = u; u_x = 0$
B4	1280	$\nabla T = 0$	$u_y = u; u_x = 0$

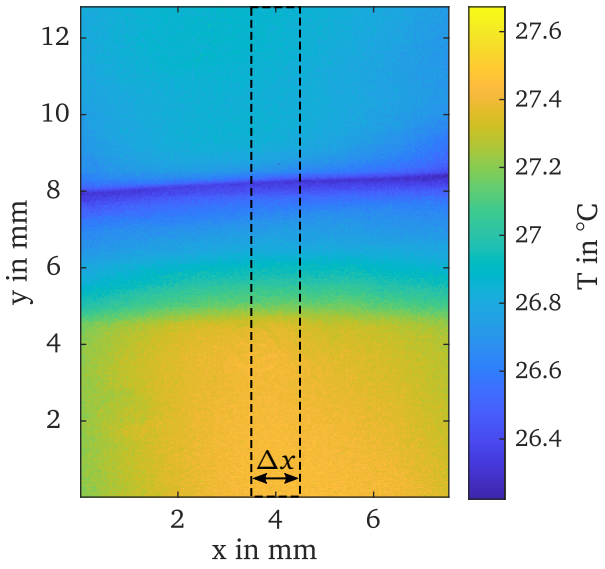

Figure 3.12: Example of a measured temperature field T_{IR} on a flat sample. Data within Δx is averaged in x-direction and then used as a boundary condition within the heat flux calculation.

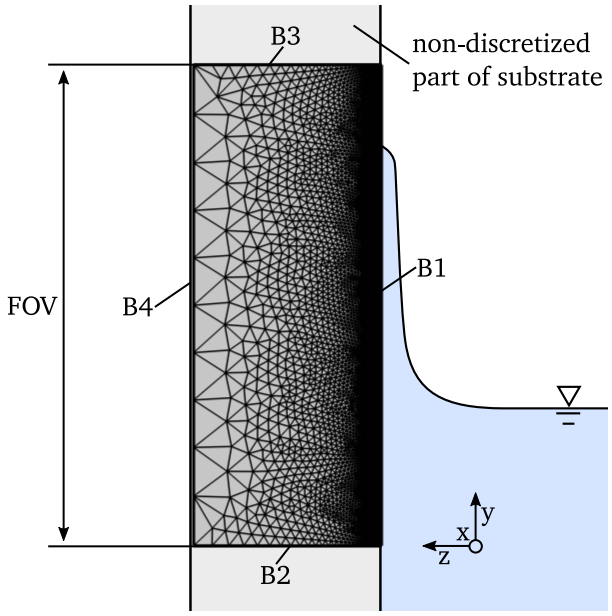

Figure 3.13: Computational domain showing the grid and boundaries B1 to B4. Only the portion of the sample currently within the FOV is discretized.

$$\rho_s c_{p,s} \frac{\partial T}{\partial t} + \rho_s c_{p,s} \vec{u} \nabla T + \lambda_s \nabla^2 T = 0. \tag{3.2}$$

Therein ρ_s, $c_{p,s}$ and λ_s describe the density, specific heat capacity and thermal conductivity, respectively, of the solid substrate. The values are set to those of calcium fluoride at 25 °C and assumed constant. The vector $\vec{u}$ is equal to zero in x-direction, $\vec{u}_x = 0$, and a step function in y-direction:

$$\vec{u}_y = \begin{cases} 0 & t < t_{start} \\ u & t_{start} \leq t \leq t_{end} \\ 0 & t_{end} < t \end{cases}, \tag{3.3}$$

where t_{start} and t_{end} describe the point in time, where the sample begins and stops moving, respectively. The step function is necessary because the sample is at rest during the beginning and end of the infrared recordings. The values of t_{start} and t_{end} are thereby easily obtained from the change in χ_i over time. Hence, a convective inflow and outflow proportional to the dewetting velocity is assumed across the boundaries B2 and B3, respectively. The initial temperature within the solid is set to the temperature distribution measured at B1 at $t = 0$, $T(y, z, t = 0) = T_{IR}(y, t = 0)$. The temperature of the inflow at B2 is set to the temperature measured at $y = 0$. Heat loss to the low pressure atmosphere across boundary B4 is neglected and the boundary condition is, therefore, assumed as adiabatic.

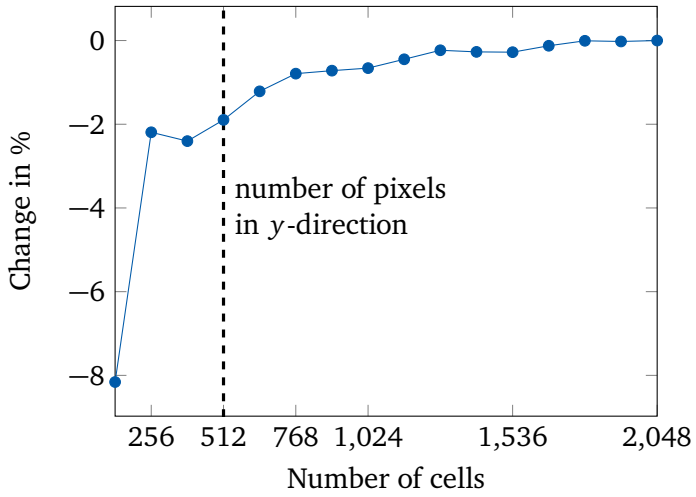

Figure 3.14: Influence of the number of cells at boundary B1 on the total heat flux across B1. The change is relative to the case with 2048 cells and the vertical dashed line marks the pixel resolution of the infrared camera in y-direction.

A triangular grid is used for meshing with the cell size gradually decreasing towards boundary B1. The necessary cell size at boundary B3 is found by evaluating the simulation results for an increasing number of elements at this boundary. If the number of cells is unequal to the amount of pixels of the infrared camera in y-direction (512), the cell temperature is calculated by linear interpolation. The total heat flux in time and space across boundary B3 is chosen as the indicating parameter, whose change relative to the solution with 2048 cells is shown in Figure 3.14. For an increasing number of elements, the change in the total heat flux approaches zero and is marginal above 1024 elements, which is chosen for all further calculations. A similar analysis for the mesh size on boundary B4 yielded no influence on the obtained results.

3.4 Data reduction and analysis

In order to analyze and present the time dependent and highly resolved measurement data efficiently, it is necessary to reduce the amount of data and derive representative quantities. This process is outlined below using a typical dewetting experiment with ethanol as an example. The course of this measurement is displayed in Figure 3.15, where the measured temperature field is shown for different points in time. In Figure 3.15a, the sample is heated but still at rest, and the location of the contact line (1) can be identified within the FOV by the local drop in temperature, which is a result of the strong evaporation in this region. The region underneath and above the static contact line are referred to as the bulk liquid region (2) and the dry wall region (3), respectively. In Figure 3.15b, the sample is in motion and the contact line is dragged upwards. Consequently, a microlayer (4) is formed. A dewetting ridge (5) of increased liquid thickness can be observed during this process. The slightly curved bright line (6) above the microlayer marks the upper edge of the sample. The sample is slightly warmer in this region due to the contact resistance between the Cr-coating and the copper spring contacts. Eventually, the microlayer length does not increase any further,

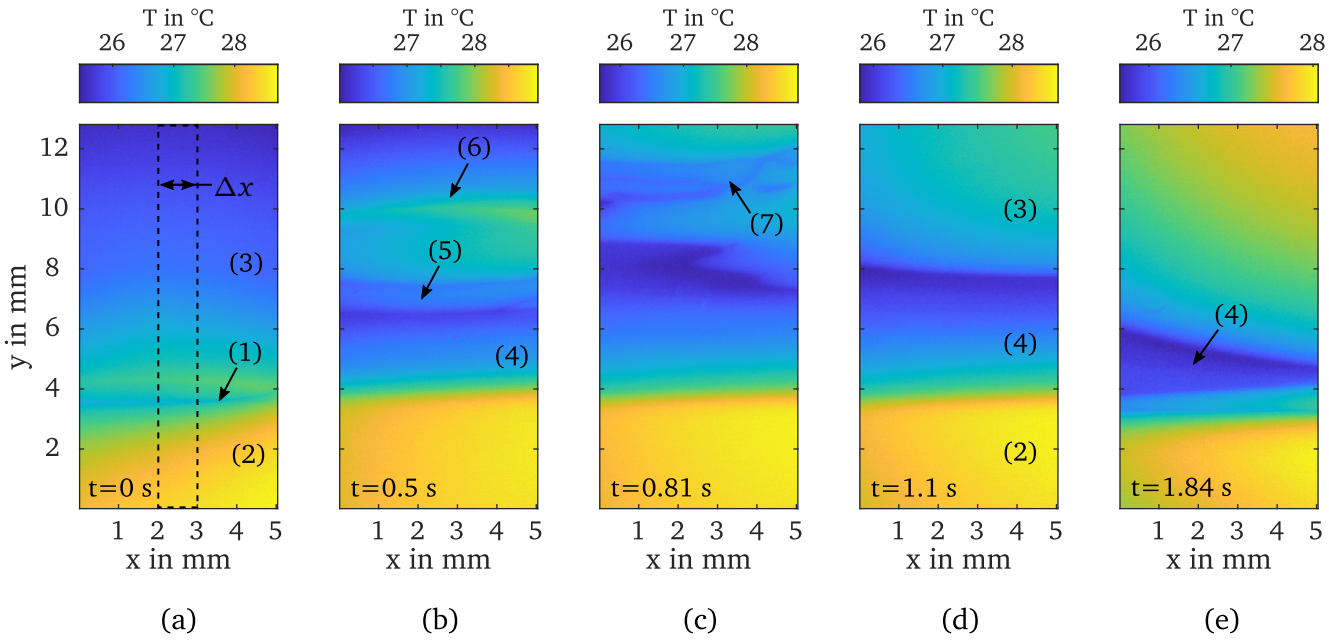

Figure 3.15: T_{IR} during the course of a typical measurement: (a) $u = 0$, start of the measurement. (b) Microlayer formation. (c) Instabilities at the end of the microlayer. (d) Microlayer in steady state. (e) $u = 0$, breakup of microlayer at the end of the measurement. (1) Contact line, (2) bulk liquid region, (3) dry wall region, (4) microlayer, (5) dewetting ridge, (6) sample edge, (7) detached liquid.

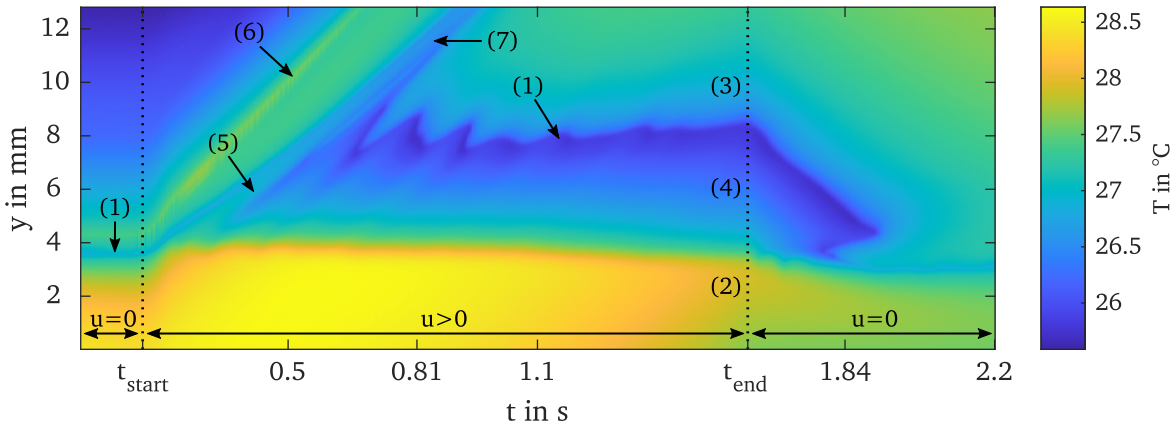

Figure 3.16: Kymograph of the whole measurement shown in Figure 3.15 with (1) contact line, (2) bulk liquid region, (3) dry wall region, (4) microlayer, (5) dewetting ridge, (6) sample edge, (7) detached liquid. The markings on the abscissa correspond to Figure 3.15a-e.

which is illustrated in Figure 3.15c. However, instabilities leading to local film breakup near the end of the microlayer can be observed, causing the microlayer to fluctuate in length. In addition, the dewetting ridge detaches (7) from the rest of the microlayer and it is carried out of the FOV by the motion of the sample. In Figure 3.15d, the initial instabilities caused during the formation process and the fluctuation of the microlayer length have reduced in magnitude. A slight curving of the contact line can be observed, which is caused by a slight temperature gradient across the sample in x-direction. In Figure 3.15e, the movement of the sample has stopped and the microlayer starts to break up and eventually disappears completely due to evaporation.

In analogy to the heat flux calculation in section 3.3, each measurement is reduced to two dimensions for further analysis by averaging T_{IR} in x-direction within the area $\Delta x = 1\,\mathrm{mm}$ located in the center of the sample. Δx is indicated in Figure 3.15a and identical to Δx used for the heat flux calculation. The averaging process allows the whole measurement to be conveniently viewed as a single image, which is also referred to as a *kymograph*. The kymograph for the measurement shown in Figure 3.15 is displayed in Figure 3.16. The time stamps of Figure 3.15a-e are marked on the abscissa for direct comparison. Beginning and end of the sample motion are indicated by t_{start} and t_{end}, respectively. While the information in the x-direction is lost, a much better impression of the measurement as a whole is gained. For instance, comparing the gradient of the edge of the sample (6) with the gradient of the dewetting ridge (5) immediately reveals that a velocity difference exists between the two. Other than serving as a tool for visualization, the kymograph of each measurement is used for data analysis, which is described in the following.

3.4.1 Microlayer length

The analysis of the contact line position is shown in Figure 3.17. The momentary position of the contact line $y_{cl}(t)$ is determined by finding the local minimum in T_{IR} in the kymograph for each time step. After the initial growth and transient oscillations, y_{cl} does not change much between t_1 and t_2, which is referred to as the steady state of the microlayer. t_1 and t_2 are determined by hand for each experiment.

At the beginning and end of the measurement, where $u = 0$, y_{cl} is constant and corresponds to the location of the contact line at the end of the static meniscus y_{sta}. Unfortunately, y_{sta} is not the same before and after the dewetting process. This can best be observed by comparing $y_{cl}(t < t_{start})$ to $y_{sta}(t > t_{end})$. The latter is specifically indicated as a horizontal line in Figure 3.17 for this purpose. In the displayed experiment, the absolute decrease in the static contact line position $\Delta y_{sta} = y_{sta}(t < t_{start}) - y_{sta}(t_{end} < t)$ is 0.475 mm. This decrease is likely caused by an overall decrease of the liquid pool height due to a combination of effects, such as the sample leaving the liquid pool and film formation on the rotating disc. It was observed that the magnitude of Δy_{sta} is the same for experiments using the same sample, liquid, and movement distance. Furthermore, the decrease in the height of the liquid pool over the cause of a single measurement is linear, which can be best observed in measurements where no microlayer is formed. The constant decrease is likely a result of the almost constant dewetting velocity. Therefore, the hypothetical static contact line position $y_{sta}(t)$ is obtained by linear interpolation between the static position of the contact line before and

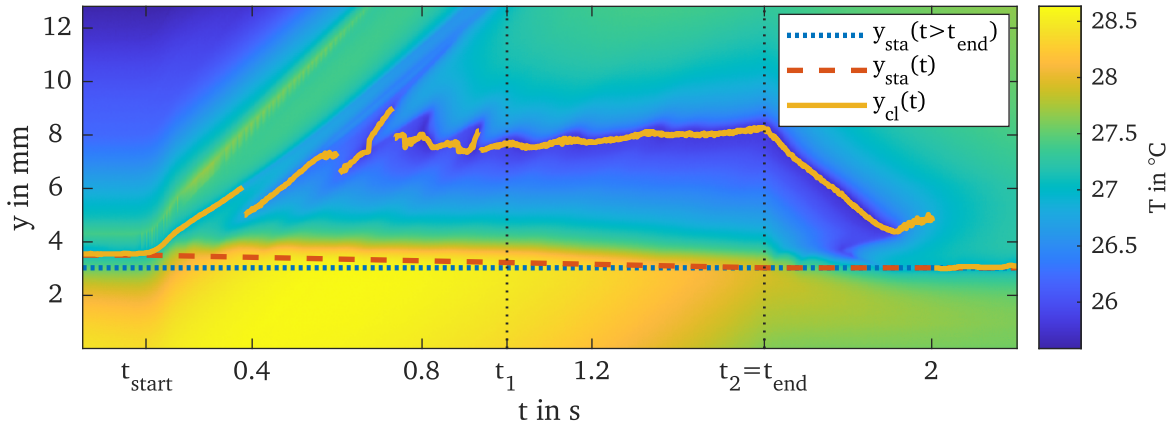

Figure 3.17: Determination of the dynamic position of the contact line $y_{cl}(t)$ and the static position of the contact line $y_{sta}(t)$. The latter is gained by linear interpolation between the $y_{cl}(t_{start})$ and $y_{cl}(t_{end})$. t_1 and t_2 indicate the steady state.

after the dewetting process, i.e. between $y_{cl}(t < t_{start})$ and $y_{cl}(t_{end} < t)$. $y_{sta}(t)$ is indicated in Figure 3.17 as the dashed line.

In order to calculate the microlayer length, the beginning of the microlayer has to be located. To outline this procedure, the instantaneous heat flux profile at $t = 1.24\,\mathrm{s}$, $q_{1.24\mathrm{s}} = q(y, t = 1.24\,\mathrm{s})$, for the same measurement displayed in Figure 3.16 is shown in Figure 3.18a. Heat flux sharply begins to increase before a plateau is reached at y_0. The beginning of this sharp increase is interpreted as the end of the bulk liquid region (1) and the start of the dynamic meniscus region (2), and is denoted with y_b. Hence, y_0 marks the beginning of the microlayer region (3). Heat flux peaks at the contact line, which coincides with y_{cl} in Figure 3.17, and marks the end of the microlayer, beyond which the dry wall region (4) remains. y_b and y_0 are obtained directly from the heat flux profile, which is illustrated by the linear model in Figure 3.18a. The heat flux profile for $y < y_{cl}$ is fitted to a model consisting of three linear functions. y_b and y_0 then coincide with y, where the mean gradient of the heat flux profile changes.

In contrast to y_b, y_0 cannot be determined with sufficient accuracy from the heat flux data in all experiments because the change in gradient between dynamic meniscus and microlayer region can be very insignificant. This is especially true for very short microlayers in FC-72 at high ΔT, where the heat flux does not reach a plateau in the microlayer region but rises towards the contact line. In these cases, y_0 is estimated on the basis of y_b and the mean size of the meniscus region found in other experiments with the same liquid.

y_b generally coincides with y_{sta} for both FC-72 and ethanol. In some experiments the position of the contact line can only be determined for either $y_{cl}(t < t_{start})$ or $y_{cl}(t_{end} < t)$, for example due to delayed triggering of the infrared recording. In these cases y_{sta} is estimated from y_b.

Having determined the beginning and end of the microlayer for each time step, $y_0(t)$ and $y_{cl}(t)$, respectively, the microlayer length is obtained from their difference $y_{cl}(t) - y_0(t)$. The steady state microlayer length h

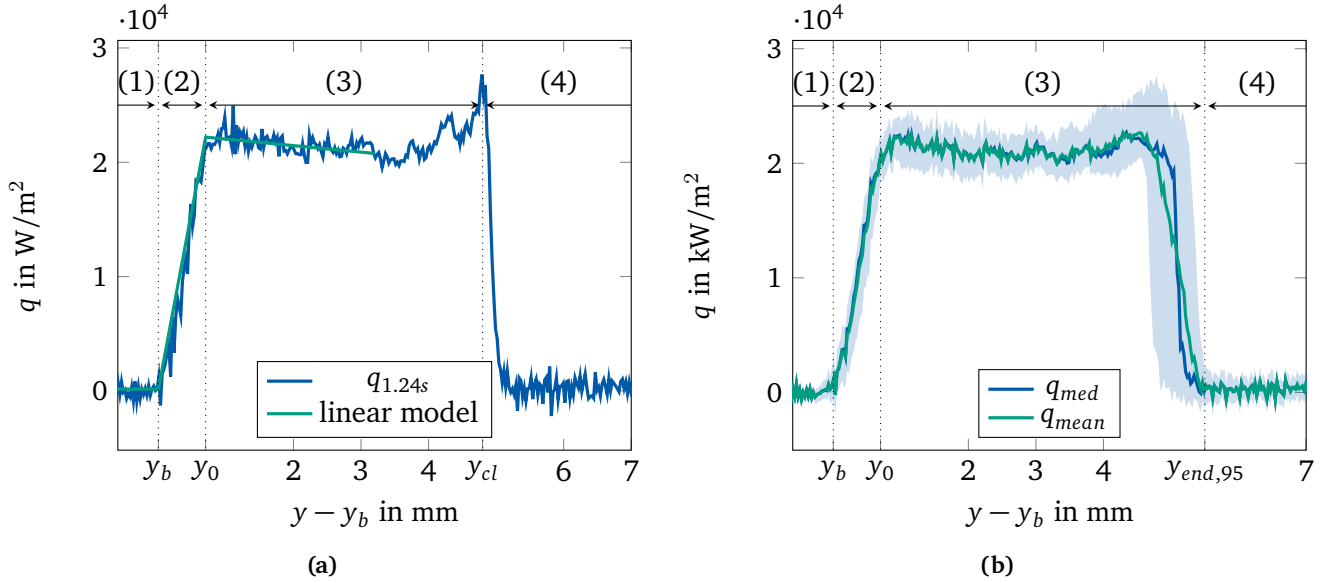

Figure 3.18: Local heat flux over y for the measurement displayed in Figure 3.17 with (1) bulk liquid region, (2) dynamic meniscus region, (3) microlayer region, (4) dry wall region. (a) Instantaneous heat flux profile at $t = 1.24\,\mathrm{s}$ and estimation of y_b and y_0. (b) Comparison of different methods for the evaluation of the heat flux profile in steady state. The upper and lower boundaries of the shaded area mark the 95$^{\text{th}}$ and 5$^{\text{th}}$ percentile of q, respectively.

is calculated from the mean of $y_{cl}(t_1 < t < t_2) - y_0(t_1 < t < t_2)$ in time and the standard deviation is used to describe the measurement uncertainty of h.

3.4.2 Heat flux

To easily compare the shape of the local heat flux of different measurements, a suitable method for representing the heat flux profile during the steady state (between t_1 and t_2) has to be found. This process is outlined in Figure 3.18b, where two approaches are compared. q_{mean} and q_{med} are obtained from the temporal mean and median, respectively, from $q(t_1 < t < t_2)$. The shaded area is displayed as a measure of the fluctuations in the steady state. The top and bottom of the shaded area mark the 95$^{\text{th}}$ and 5$^{\text{th}}$ percentile of q, respectively. While the heat flux within most of the microlayer is generally equally well described by both q_{mean} and q_{med}, neither can capture the shape of the heat flux close to the contact line seen for the instantaneous profile in Figure 3.18a. The best description is achieved by q_{med} because the sharp drop in heat flux at the end of the film is preserved. The peak in heat flux, however, is lost in both q_{med} and q_{mean}. The peak indeed exists during the whole steady state for this measurement and evidence for this can be found in the shape of the 95$^{\text{th}}$ percentile. Therefore, using q_{mean} or q_{med} to describe the shape of the heat flux profile leads to considerable loss of information. On the other hand, the usage of an instantaneous profile can be ambiguous because of the possible inclusion of momentary fluctuations. Comparing the drawbacks of all three methods, q_{med} is seen as most suitable for the evaluation of the heat flux profiles. The heat flux at the contact line is analyzed using the separate quantity q_{cl}, which describes the magnitude

of the contact line peak during the steady state. q_{cl} is obtained by locating the maximum of the contact line peak for each time step during the steady state, from which the temporal mean is then calculated.

To directly compare the overall heat flux during the steady state of each experiment, the heat flux profile is integrated. Q_{tot} describes the total heat flux caused by the dewetting process and is obtained by integration of q from y_b to $y_{end,95}$. Hence, Q_{tot} includes the heat flux of both the meniscus region Q_{men} and microlayer region Q_{ml}:

$$Q_{tot} = Q_{men} + Q_{ml}. \tag{3.4}$$

$y_{end,95}$ is chosen as an upper integration limit to also capture the fluctuations in microlayer length and possible instabilities, which would be lost if y_{cl} was used as the upper limit for integration instead. Care is taken to not include evaporation caused by any liquid that detached from the microlayer before t_1 and that might still be within the FOV during the steady state. Similarly, the evaporation caused by the microlayer Q_{ml} is obtained by integration of q from y_0 to $y_{end,95}$. Q_{men} is then calculated by rearranging Equation 3.4. Please note that the definition of Q_{tot} above also includes the total heat flux in the vicinity of the contact line: In the presence of a microlayer, the effects of the contact line are included in Q_{ml}. In the absence of a microlayer, Q_{ml} is zero and the effects of the contact line, thus, included in $Q_{men} = Q_{tot}$.

3.4.3 Wall superheat

In boiling research, the wall superheat ΔT describes the difference between the wall temperature T_w and the saturation temperature T_{sat}. A pure vapor atmosphere is assumed within the test chamber and justified in section 3.5 below. Furthermore, it is ensured that the pressure p and the temperature of vapor and

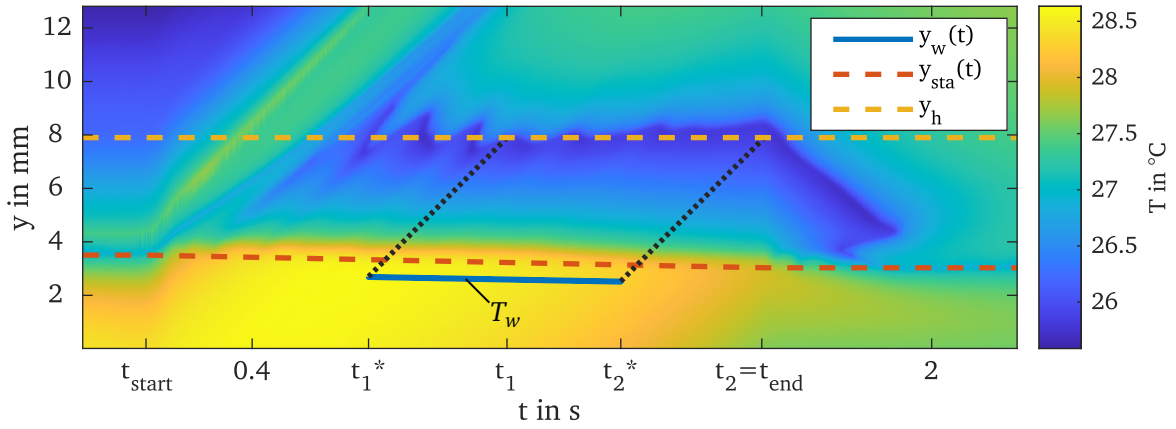

Figure 3.19: The wall temperature T_w is found by tracing the trajectories of the points of the wall located on y_h during the steady state underneath $y_{sta}(t)$. The mean of the temperatures located on $y_w(t_1^* < t < t_2^*)$ equals T_w.

liquid, T_g and T_l, respectively, are stationary before conducting any experiments. Therefore, it is assumed that $T_{sat} = T_g$ and the wall superheat calculated as $\Delta T = T_w - T_g$.

The determination of the wall temperature T_w is illustrated in Figure 3.19. It can be seen that the temperature in the bulk liquid region slightly varies throughout the measurement. However, the temperature within the bulk liquid region is not equally relevant for the microlayer at every point underneath $y_{sta}(t)$ because wall movement has to be taken into account. For instance, the point of the wall located at $y = 2\,\text{mm}$ at $t = t_{start}$ has long since passed the contact line before the microlayer length reaches the steady state. On the other hand, any point located underneath $y_{sta}(t_{end})$ never leaves the bulk liquid region. These parts of the wall are irrelevant and should not be included in T_w. The point $y_{sta}(t_1)$, however, passes through the whole steady state microlayer. Hence, the temperature of this part of the wall contributes to the rate of evaporation in the microlayer and is, therefore, relevant. The whole part of the wall passing through the microlayer during the steady state is found by following the trajectories of the parts of the wall located at the end of the microlayer between t_1 and t_2. For this purpose, the end of the microlayer is calculated from the mean contact line position during the steady state, y_h. The trajectories of the parts of the wall located at the end of the microlayer at t_1 and t_2 are indicated by the black dotted lines. These trajectories are followed 0.625 mm (25 pixels) below $y_{sta}(t)$, i.e back to the time step t_1^* and t_2^*. In other words, all points on the line $y_w(t_1^* < t < t_2^*)$ reach or cross the end of the microlayer between t_1 and t_2. Note that in two dimensions y_w corresponds to an area on the sample. T_w is then obtained from the mean temperature measured on $y_w(t_1^* < t < t_2^*)$ and the variance of the temperature on this line accounts to the overall measurement uncertainty in ΔT.

3.4.4 Microlayer thickness

The microlayer thickness δ is expected to be a function of y and decrease from an initial thickness δ_0 at the end of the dynamic meniscus region y_0 towards zero at the contact line. The microlayer thickness measured directly by the interferometric probe is denoted with δ_{IP} and is measured approximately $1-2\,\text{mm}$ above the hypothetical location of the static contact line y_{sta}. The measurement location is further discussed below. Unfortunately, δ_{IP} could only be obtained for FC-72 and not for ethanol. With the latter, the frontal cell window would always be covered with liquid droplets after the initial heating process due to condensation and splashing caused by the evaporation near the contact line. It is not entirely clear why this was not observed in the case of FC-72. Therefore, only the reference case at $\Delta T = 0$ was measured with the interferometric probe for ethanol.

A measurement of δ_{IP} during microlayer formation with FC-72 is plotted in Figure 3.20a. A maximum can be observed at the beginning of the measurement, which is followed by oscillations, whose amplitude decreases in time. This corresponds to the formation process, fluctuation, and steady state observed for the microlayer length. At the end of the measurement, δ_{IP} starts to decrease quickly and disappear, which marks t_{end}. This point in time is used to match the time evolution of δ_{IP} with the temperature and heat flux data through the known temporal resolution in both measurements. The matching indicates that the

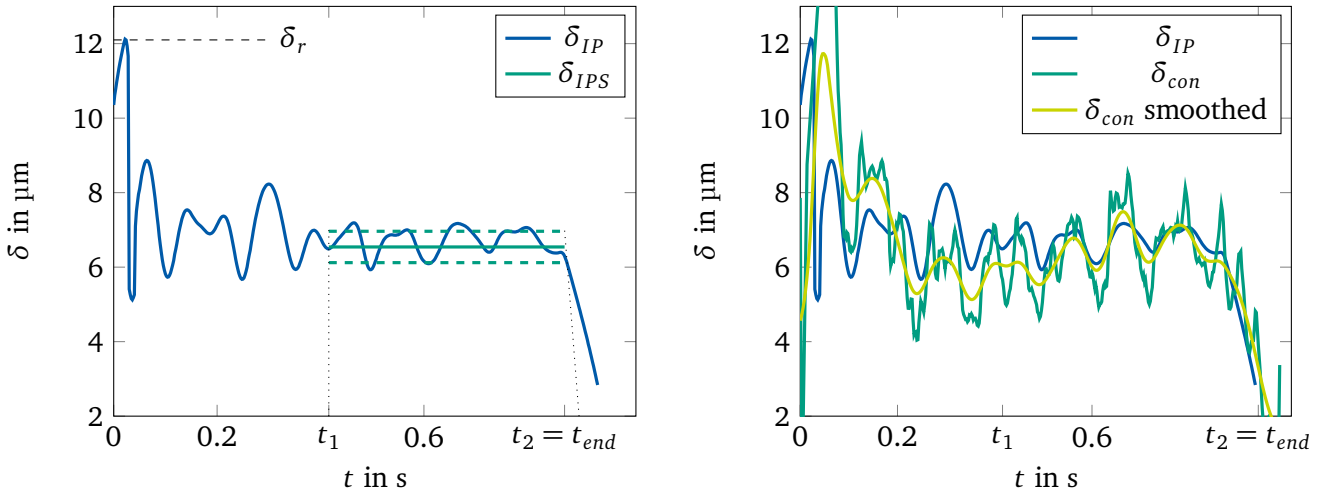

Figure 3.20: δ_{IP} during an experiment with FC-72. (a) Deduction of δ_r and δ_{IPS} with the horizontal dashed lines describing the standard deviation of δ_{IP} in the steady state. (b) Comparison of δ_{IP} and δ_{con} over time at measurement location inferred from Figure 3.21.

maximum corresponds to the thickness of the dewetting ridge δ_r at the front of the microlayer, which later gives rise to the detached liquid marked in Figure 3.16.

Following the procedure for h, the steady state microlayer thickness δ_{IPS} is calculated from the mean of $\delta(t_1 < t < t_2)$ and the variance accounts to the measurement uncertainty. In some measurements the length of the microlayer is too long to be determined because the contact line leaves the upper edge of the FOV. Hence, no steady state can be determined from the kymograph. The thickness of these microlayers, however, is still measured reliably. To also obtain a steady state microlayer thickness in these cases, the steady state is instead determined directly from the thickness data. The found t_1 and t_2 are then used to calculate T_w as described above. h is thereby assumed to equal the upper edge of the FOV. A major drawback of δ_{IP} is, however, that the exact measurement location with respect to y_b is unknown. The location is estimated by determining the minimum microlayer length, for which thickness data is recorded. Based on this, the measurement position is approximated to be located between 1 mm to 2 mm above y_b. This is in agreement with the manual positioning of the sensor described in section 3.1.4, when taking the decrease of the liquid pool height Δy_{sta} into account. Therefore, it is expected that the measured value of δ_{IP} is lower than the initial microlayer thickness δ_0 at y_0 because of the evaporative thinning towards the contact line.

The local microlayer thickness is calculated from the local heat flux $q(y,t)$ by assuming linear one dimensional heat conduction through the microlayer [19, 81]. As shown by Giustini et al. [49], however, a correction in form of an evaporation heat transfer resistance R_{ev} might be necessary for this method to give satisfactory results. Following this approach, the liquid thickness calculated by linear heat conduction δ_{con} is given by

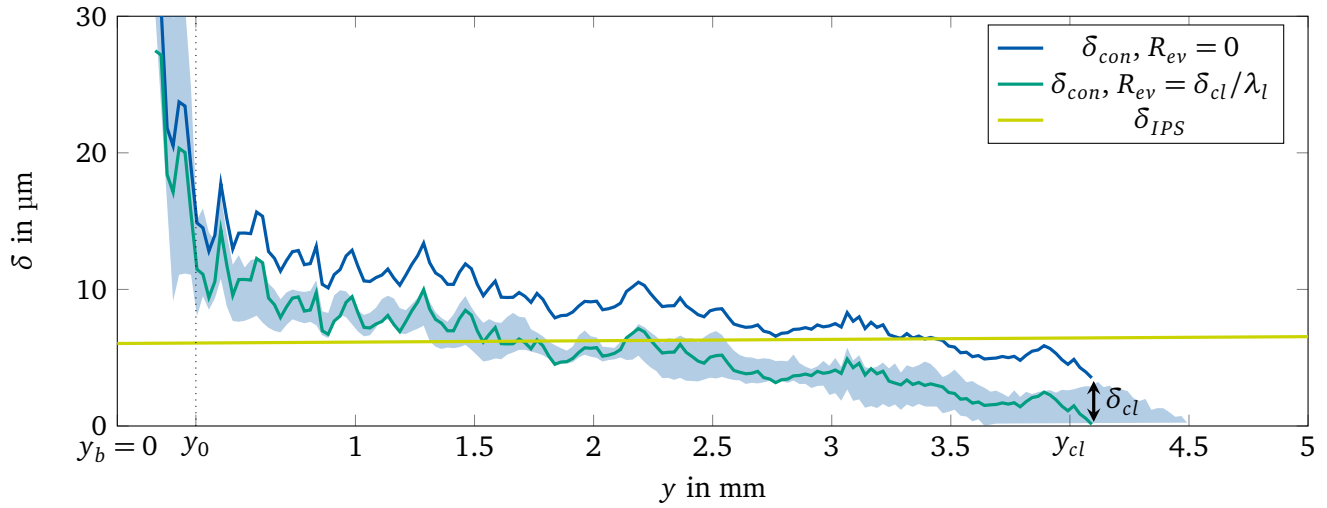

Figure 3.21: Instantaneous microlayer thickness profiles δ_{con} obtained with Equation 3.5 for FC-72 in comparison to δ_0 and δ_{IP}. The shown time step corresponds to $t = 0.78\,\mathrm{s}$ in Figure 3.20a. The shaded area indicates 5^{th} and 95^{th} percentiles of δ within the whole steady state.

$$\delta_{con}(y,t) = \lambda_l \left(\frac{T_{IR}(y,t) - T_{sat}}{q(y,t)} - R_{ev} \right). \tag{3.5}$$

The determination procedure of the unknown value of R_{ev} is illustrated in Figure 3.21, where two instantaneous thickness profiles obtained with Equation 3.5 are shown. The measurement depicted in Figure 3.21 and Figure 3.20a is the same and both instantaneous profiles were calculated from the same arbitrary time step $t = 0.78\,\mathrm{s}$. y_b, y_0 and y_{cl} are each indicated on the abscissa. As heat flux at y_b is close to zero, δ_{con} tends to infinity as y_b is approached from the meniscus region. However, the gradient of both profiles sharply changes near the beginning of the microlayer, which coincides with y_0 obtained from the heat flux profile. This supports the assumption made above that y_0 indeed describes the boundary between the meniscus region and the microlayer region.

The difference between both thickness profiles becomes most apparent at the contact line; for $R_{ev} = 0$, δ_{con} does not reach zero at y_{cl} but only a minimum thickness of $\delta_{cl} = 3.34\,\mu\mathrm{m}$. The nonexistence of such a thick film beyond the contact line is easily proven by carrying out the same analysis for a measurement, where the microlayer is too short to be detected by the interferometric probe. Here, δ_{cl} is of similar magnitude but nothing is detected by the interferometric probe. Hence, it must be an error. In addition, the measurement location of the interferometric probe does not match the previous estimation, when inferred from the intersection of δ_{IPS} and the thickness profile calculated with $R_{ev} = 0$. Therefore, the thickness profile is corrected by finding a suitable value for R_{ev}. For this purpose, the existence of an adsorbed film is neglected and δ is assumed zero at the contact line. In a preliminary calculation, the thickness profile is obtained with $R_{ev} = 0$, from which the mean thickness at the contact line δ_{cl} during the steady state is evaluated. The thickness profile is then recalculated with

$$R_{ev} = \frac{\delta_{cl}}{\lambda_l}. \tag{3.6}$$

With Equation 3.6, $\delta_{con}(y_{cl}) = 0$ is now obtained by Equation 3.5. The resulting profile is also shown in Figure 3.21 and is compared to the interferometric measurement for validation. Inferring the measurement location of the interferometric probe from the intersection with δ_{IPS} now yields approximately 1.7 mm, which is in good agreement with the approximation made earlier.

Agreement can be further tested by comparing the time evolution of $\delta_{con}(t)$ at the inferred measurement location to δ_{IP} measured with the interferometric probe. This comparison is shown in Figure 3.20b. The data of δ_{IP} and δ_{con} was aligned using an estimated value for t_{end}, as explained previously. Large fluctuations are seen in δ_{con}, which are not measured in δ_{IP} and are likely a result of the noise in the temperature data and the heat flux calculation. Therefore, δ_{con} is smoothed by a Gaussian filter. It should be noted, though, that the necessary level of smoothing decreases with increasing wall superheat in the experiment because noise effects become comparably less important. However, it becomes apparent from the smoothed data that the fluctuations seen in δ_{con} follow those seen in δ_{IP}. Overall agreement is good, especially in the steady state. Naturally, the agreement is not perfect. However, considering the long chain of experimental and computational methods needed to obtain δ_{con}, each carrying multiple sources of uncertainty, both measurement methods agree remarkably well. The same observations are made for all measurements with FC-72. With ethanol, on the other hand, δ_{IP} could not be measured and the values obtained for δ_{con} can, thus, not be validated. However, the thermal conductivity of ethanol is almost three times as high as that of FC-72 and the assumption of a linear temperature profile across the thickness of the microlayer is, therefore, likely justified as well. Hence, it is assumed that the method of obtaining δ_{con} described above is valid for both liquids.

3.5 Measurement uncertainties

The measurement uncertainty for all measured or derived quantities is discussed below. For most quantities, measurement uncertainty varies between experiments and an absolute value can, thus, not be given. Hence, in this chapter the calculation method for the uncertainty of each quantity is presented. The absolute values are then displayed alongside the measurement data in chapter 4.

Temperature of gas and liquid

The temperature of the bulk liquid and gas are determined using Pt-1000 temperature sensors, which are relocated approximately 5 mm distanced from the sample's coated surface on side (A) of the test cell. The temperature sensors were calibrated by comparing against a Pt-100 reference sensor within a calibration

bath. A measurement uncertainty of $e_{\mathrm{Pt1000}} = \pm 200\,\mathrm{mK}$ and an accuracy of $\pm 10\,\mathrm{mK}$ was determined for the calibrated Pt-1000 temperature sensors.

Vapor pressure

The pressure on side (A) of the central disc is measured by a pressure transducer with a measurement uncertainty of ±0.1% of the measurement range, resulting in a measurement uncertainty of $e_p = \pm 1\,\mathrm{mbar}$. A leakage test of the test facility was performed over the duration of 4 weeks, from which a leakage rate of $0.048\,\mathrm{mbar\,h^{-1}}$ ($\approx 5{\times}10^{-5}\,\mathrm{mbar\,L\,s^{-1}}$) was determined. The influence of leakage on the experimental results is, therefore, assumed negligible.

Microlayer thickness

The thickness of the microlayer is determined with a commercially available interferometric white light point sensor (Precitec CHRocodile 2SE)[1] with a measurement range between 2 µm to 180 µm, a resolution of 10 nm and a measurement uncertainty of $e_{\delta_{IP}} = \pm 100\,\mathrm{nm}$. The measuring spot is approximately 40 µm in diameter and data is recorded with a temporal resolution of 1000 Hz. The measurement uncertainty for δ_{IPS} is calculated by

$$e_{\delta_{IPS}} = \sqrt{e_{\delta_{IP}}^2 + var(\delta_{IP})}, \tag{3.7}$$

where $var(\delta_{IP})$ is the variance of δ_{IP} during the steady state only. $e_{\delta_{con}}$ is assumed equal to $e_{\delta_{IPS}}$.

Sample surface temperature

The surface temperature of the sample T_{IR} is determined by infrared thermography, for which a Flir X6901sc infrared camera (sensor pixel size 25 µm, resolution 640 × 512 pixels, maximal full resolution frame rate 1004 Hz, spectral band $2-5\,\mu\mathrm{m}$) in combination with a microscope lens (magnification ×1, effective focal length 19.8868 mm) is used. Images are recorded at 500 Hz, an integration time of 1.7 ms, and full resolution. Temperature gradients between the front and back of the sample coating are assumed zero due to the marginal thickness of the coating. To estimate the uncertainty of T_{IR}, three main effects are considered: The standard error of estimate introduced by the infrared calibration procedure e_{est}, the uncertainty of the reference temperature throughout the calibration process e_{ref}, and the effect of the heated gas phase between sample and infrared camera on side (B) of the experimental facility. The latter will be assumed negligible for now and then addressed below.

[1] This model is capable of both chromatic and interferometric measurements.

The fitting process of a single pixel m and position i is characterized by the standard error of estimate e_{est}. This quantity can be interpreted as the mean deviation between the temperature calculated with Equation 3.1 (T_{IR}) and the reference temperatures used for the calculation of the coefficients (T_{ref}) across the whole temperature range of the calibration. For one pixel m and position i, e_{est} is given by

$$e_{est,m,i} = \sqrt{(\sum_{n=1}^{n_{max}}((T_{IR,n,m,i} - T_{ref,n})^2/(n_{max} - 3))}, \tag{3.8}$$

where n is the index of the constant reference temperature and $(n_{max} - 3)$ is the number of reference temperatures used during fitting, minus the number of coefficients in Equation 3.1. As $T_{ref,n}$ itself is a mean quantity calculated from multiple measurements, e_{ref} is gained from e_{Pt1000} and the variance of all measurements used to calculate $T_{ref,n}$. The standard uncertainty for one pixel and position is then obtained by

$$e_{T_{IR},m,i} = \sqrt{(e_{ref}^2 + e_{est,m,i}^2)} = \sqrt{e_{\mathrm{Pt1000}}^2 + \sum_{n=1}^{n_{max}} var(T_{ref,n}) + e_{est,m,i}^2}. \tag{3.9}$$

To deduce a single uncertainty for the whole infrared sensor and all sample positions, it is assumed that measurements carried out by each individual pixel m and position i are independent. $e_{T_{IR}}$ is then given by

$$e_{T_{IR}} = \sqrt{\frac{1}{m_{max}\,N} \sum_{m=1}^{m_{max}} \sum_{i=1}^{N} e_{T_{IR},m,i}^2}. \tag{3.10}$$

While each sample is calibrated individually and $e_{T_{IR}}$, thus, differs between experiments, it is approximately $e_{T_{IR}}^{eth} \approx \pm 0.35\,\mathrm{K}$ and $e_{T_{IR}}^{FC} \approx \pm 0.4\,\mathrm{K}$ for the experiments with ethanol and FC-72, respectively. The higher measurement uncertainty in the experiments with FC-72 is not due to the liquid, but rather the variations during the calibration procedure, such as worse temperature stability of T_{ref} during step 1 of the calibration procedure.

It needs to be stressed that $e_{T_{IR}}$ is the measurement uncertainty in regards to the true value and has the characteristic of an offset rather than statistical scatter. For a given temperature, this offset is of comparable magnitude for neighboring pixels and positions. Therefore, while $e_{T_{IR}}$ limits the determination of the true value of T_{IR}, it does not limit the temperature differences observable across the FOV. Rather, the latter is limited by the temporal noise in I, which is estimated by the standard deviation of I in time from a measurement of constant temperature to $e_I = \pm 4\,\mathrm{counts}$. Note, that this uncertainty is implicitly included in $e_{T_{IR}}$ because mean data is used for the fitting process during the calibration procedure. The average gradient of the calibration function is approximately 5 mK/count within the observed temperature range.

Thus, the uncertainty in T_{IR} due to noise effects can be estimated to $e_{noise} = \pm 0.02\,\mathrm{K}$. Therefore, local temperature gradients larger than $2e_{noise} = 0.04\,\mathrm{K}$ can be assumed significant.

Lastly, the influence of the gas on side (B) of the experimental facility shall be discussed. During the step 1 of the calibration procedure, this gas is heated with the rest of the experimental facility to ensure a homogeneous temperature distribution. Therefore, the infrared emission of the gas I_g are superimposed with the emission of the sample and included in the reference images. During the experiments, however, side (B) is kept at saturation temperature, while only the sample surface is heated. This introduces an error, whose magnitude is dependent on the emission spectrum of the gas on side (B) within the observed wavelength of $3-5\,\mu\mathrm{m}$. The infrared spectra of the fluids used within this thesis can be found in the appendix Figure A.1. As the transmittance of FC-72 is near unity across the whole spectral range, its influence on measurement uncertainty is assumed negligible. Ethanol, however, shows substantial absorption bands in this spectral range. Therefore, I_g^{eth} was evaluated by recording the same sample position at the same cell temperature of 25 °C, once with FC-72 vapor and once with ethanol vapor on side (B) of the test cell. As emission caused by the FC-72 vapor I_g^{FC} is assumed zero, the emission caused by the ethanol vapor I_g^{eth} was gained by subtracting the infrared recordings made with FC-72 from those made with ethanol. The difference was found to locally vary up to 100 counts, which equates to approximately 0.5 K following the estimation for e_{noise} above. The local variation of I_g is thereby caused by vignetting. To avoid such a large additional source of uncertainty, step 1 of the calibration procedure is carried out with FC-72 exclusively. To account for the change of the gas in later measurements, I_g is subtracted before converting the measurements made with ethanol from intensity to temperature. As I_g stems from the gas behind the rotating disc, it is a constant and is not affected by the sample position, sample temperature or measurement duration.

Wall superheat

The uncertainty of the wall superheat ΔT is calculated by Equation 3.11:

$$e_{\Delta T} = \sqrt{e_{T_{IR}}^2 + var(T_{IR}(y_w)) + var(T_g)}, \tag{3.11}$$

where $var(T_{IR}(y_w))$ is the variance of the sample surface temperature on y_w, from which T_w is calculated, and $var(T_g)$ is the variance of the gas temperature during the whole measurement. e_{T_g} is not explicitly included in Equation 3.11 because it is already implicitly included in $e_{T_{IR}}$.

Throughout this work, measured quantities are frequently presented in such a way that the wall superheat appears to stay constant between single experiments. Obviously, ΔT can not be perfectly reproduced and the individual measurement uncertainty in each experiment also differs. To clearly distinguish between ΔT referring to a single experiment and the wall superheat supposedly being constant throughout multiple experiments, a bar above the quantity ($\overline{\Delta T}$) indicates the latter. $\overline{\Delta T}$ is thereby obtained from the mean

value of ΔT in a set of experiments of similar ΔT. $e_{\overline{\Delta T}}$ thereby takes into account the variance of $\overline{\Delta T}$ in between single experiments and is given by

$$e_{\overline{\Delta T}} = \sqrt{var(\Delta T) + \sum_{k=1}^{k_{max}} e_{\Delta T,k}^2}. \tag{3.12}$$

Therein $e_{\Delta T,k}$ is the measurement uncertainty of ΔT within the single experiment k described by Equation 3.11. In the data presented below, $e_{\Delta T}$ varies between ±0.39 K and ±0.77 K.

Sample velocity

The vertical velocity u of any point on the sample is obtained from an analysis of the infrared recordings and given by Equation 3.13:

$$u = \frac{r_M + \Delta r}{r_M} u_M = \frac{r_M + \Delta r}{r_M} \frac{\Delta y}{\Delta F} f, \tag{3.13}$$

where u_M is the velocity of the markers on the edge of the FOV (located on the side closer towards the center of the disc), r_M the distance between the center of the rotating disc and the markings, and Δr the horizontal distance between the markings and the point on the sample, where u is to be determined. The velocity of the markers u_M is obtained by counting the number of frames ΔF recorded with the frame rate f while the markings moved by the distance Δy. Approximated for small angles of rotation, Δy is determined by observing the vertical motion of the markings within the FOV. The absolute values of Δy, Δr, and r_M are determined through the pixel-resolution of the camera. The marker velocity is evaluated multiple times between χ_{min} and χ_{max}. The mean is used to describe u_M and the standard deviation $\sqrt{var(u_M)}$ to describe the uncertainty in u_M. e_u is then estimated through the partial derivatives of Equation 3.13:

$$e_u = \frac{r_M + \Delta r}{r_M} \sqrt{var(u_M)} + \frac{u_M}{r_M} \Delta x + \frac{\Delta r u_M}{r_M^2} e_{r_M}, \tag{3.14}$$

where Δx is the horizontal width of the area, which is averaged for data analysis. e_{r_M} describes the accuracy, with which the markers can be located. It is estimated to ±10 pixels, resulting in $e_{r_M} = 0.25$ mm. In the experiments presented in this thesis, e_u is largely dependent on u and remains below 10%. Typical values are, for example, 5.24 ± 0.13 mm/s or 20.53 ± 0.54 mm/s. The increased uncertainty at higher velocities is mainly due to the increase in friction between the central disc and the shaft seal, as well as the overall shorter measurement duration, which both present a challenge for the motor controller. Thus, the velocity of the sample slightly varies during the measurement at higher velocities.

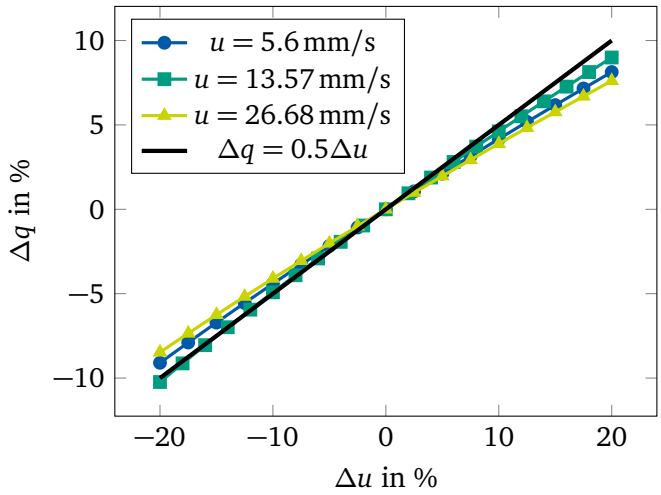

Figure 3.22: Relative change in the simulated heat flux Δq over the relative change in dewetting velocity Δu for three experiments at different levels of u.

Heat flux

The nature of the applied numerical method makes it difficult to directly relate the uncertainty in the measurement data to the numerical solution obtained for the local heat flux. To assess this complex interaction, a sensitivity analysis is performed for the dependency of the numerical solution on the dewetting velocity and substrate temperature. No dependency was observed for the latter because $e_{T_{IR}}$ is assumed constant across the sensor and, therefore, has no impact on the analysis of heat flux, which is evaluated from gradients in temperature.

The influence of a possible mismatch in u between experiments and numerical simulations is evaluated by carrying out the same simulation for varying u, i.e. purposefully altering u from what was measured in the experiment. This analysis is shown in Figure 3.22, where the change in total heat flux Δq in the microlayer region is plotted over Δu, which describes the relative change in u. Both values are given in percent and relate u actually measured in the experiment, which is assumed the true value for this purpose. The analysis was carried out for three different experiments at different magnitudes of u. The dependency in all three cases is very similar and the change in simulated heat flux across the solid-liquid interface follows the sign of the change in u. A dependency on the absolute magnitude of u can not be observed. Based on the data in Figure 3.22, the relationship between Δu and Δq is conservatively estimated as $\Delta q = 0.5\Delta u$, which is indicated by the black line in Figure 3.22. Hence, e_{sim}, which is the error in q due to e_u in the simulation, is described by

$$e_{sim} = 0.5\frac{q}{u}e_u. \tag{3.15}$$

The measurement uncertainty for q and Q is then obtained by Equation 3.15, where $var(q)$ describes the variance of the individual quantity during the steady state:

$$e_q = \sqrt{e_{sim}^2 + var(q)}. \tag{3.16}$$

In the experiments presented below, e_q tends to be greater in experiments with FC-72 and towards higher wall superheat, both due to the increased fluctuations of the microlayer. In the majority of experiments, e_q is below ±10% of the measured value.

CHAPTER 4

Results and discussion

The results obtained by the experiments and the numerical heat flux calculations are presented in this chapter. The measurement data is largely displayed in their measured dimensions to preserve the sense of scale for the reader. Comparison of data between both fluids, deduction of correlations, or comparison to existing expressions, however, is done using dimensionless quantities. The Jakob number Ja

$$\mathrm{Ja} = \frac{\Delta T c_p}{\Delta h_v} \tag{4.1}$$

is thereby used to describe the wall superheat ΔT. Some of the derivations, discussions, and results given in this chapter have been published by the author (Schweikert et al. [129, 131]).

4.1 Shape of the microlayer

This section is focused on the shape of the microlayer during its various stages of existence. The shape during the steady state is presented first, followed by the formation and depletion process.

4.1.1 Microlayer profile in steady state

Figure 4.1 shows the shape of the microlayer during steady state for ethanol for five different dewetting velocities u and levels of wall superheat ΔT. As the absolute length of the microlayer differs in each of the profiles displayed, y is normalized by y_{cl} to allow convenient comparison. Despite the variation of the dewetting velocity u, the wall superheat ΔT, and the microlayer length h in the displayed data, the shape of all profiles is very similar. Towards low y/y_{cl}, all profiles initially overlap and show a rapid decrease of the film thickness δ with increasing y/y_{cl}. As outlined in section 3.4, this region is assumed to be part of the dynamic meniscus and not the microlayer. Above $y/y_{cl} \approx 0.2$, the gradient of the thickness profiles decreases and becomes almost constant. Hence, δ approaches a value of zero at the contact line nearly

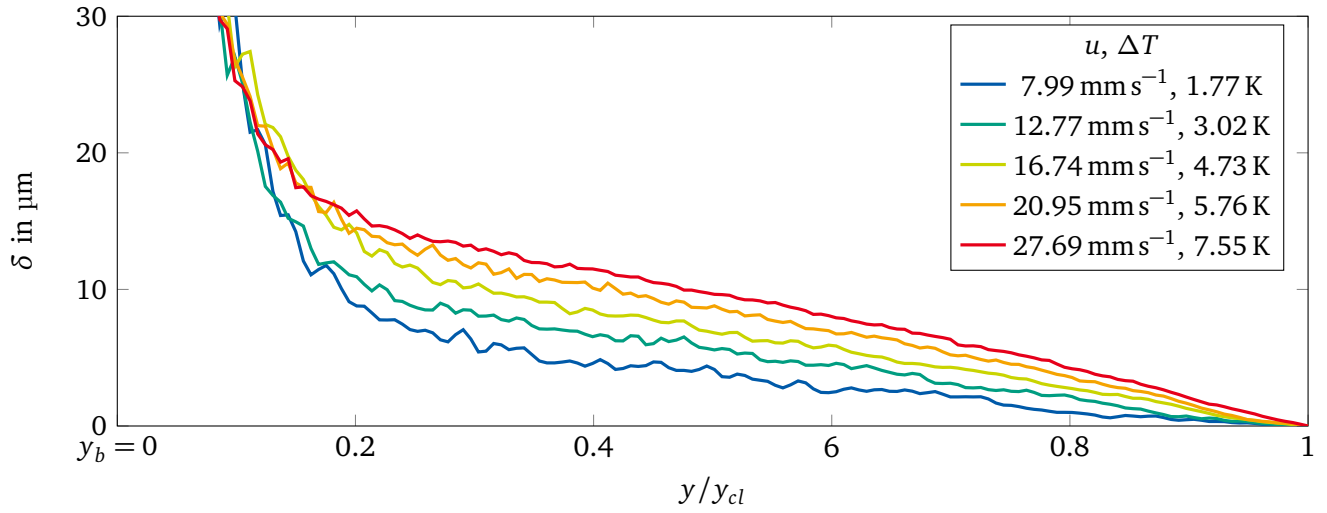

Figure 4.1: Median microlayer thickness profiles in ethanol for varying u and ΔT.

monotonically. The observed shape of the microlayer is in good agreement with the wedge-like shape of microlayers generally observed in boiling processes presented in chapter 2 (Figure 2.4a). In the majority of the data presented in this work, the wedge-shaped microlayer region (between y_0 and y_{cl}) is indeed described best by a linear function. For high ΔT for ethanol, however, the thickness profile becomes slightly concave, which can be seen for $\Delta T = 7.55\,\mathrm{K}$ in Figure 4.1. Here, a quadratic function is better suited to describe the thickness profile. A similar convex shape can also be observed for microlayers in nucleate boiling, for example in the measurements of Utaka et al. [152].

As mentioned previously, it is rather difficult to determine y_0, the location where the dynamic meniscus ends and the microlayer begins, due to the rather gradual change in curvature. Nevertheless, it can be observed that the transition from the curved dynamic meniscus region into the wedge-shaped microlayer occurs at higher δ for lager u and larger ΔT. Thus, the overall thickness of the profile increases towards higher u and ΔT. The dependency of the initial microlayer thickness δ_0, i.e. the liquid film thickness at y_0, is discussed in more detail below.

Initial microlayer thickness δ_0

The initial microlayer thickness δ_0 could theoretically be obtained from $\delta_{con}(y_0)$. However, y_0 is only estimated and, therefore, rather uncertain. Due to the proximity to the dynamic meniscus region, large gradients in δ are found near y_0, which lead to very large uncertainty in δ_0 even for small uncertainty in y_0. Therefore, δ_0 is estimated from the interferometric measurements. As shown in section 3.4, the measurement location of the interferometric probe is located approximately $1-2\,\mathrm{mm}$ above y_0. Thus, the steady state microlayer thickness δ_{IPS} measured with interferometry does not directly correspond to δ_0.

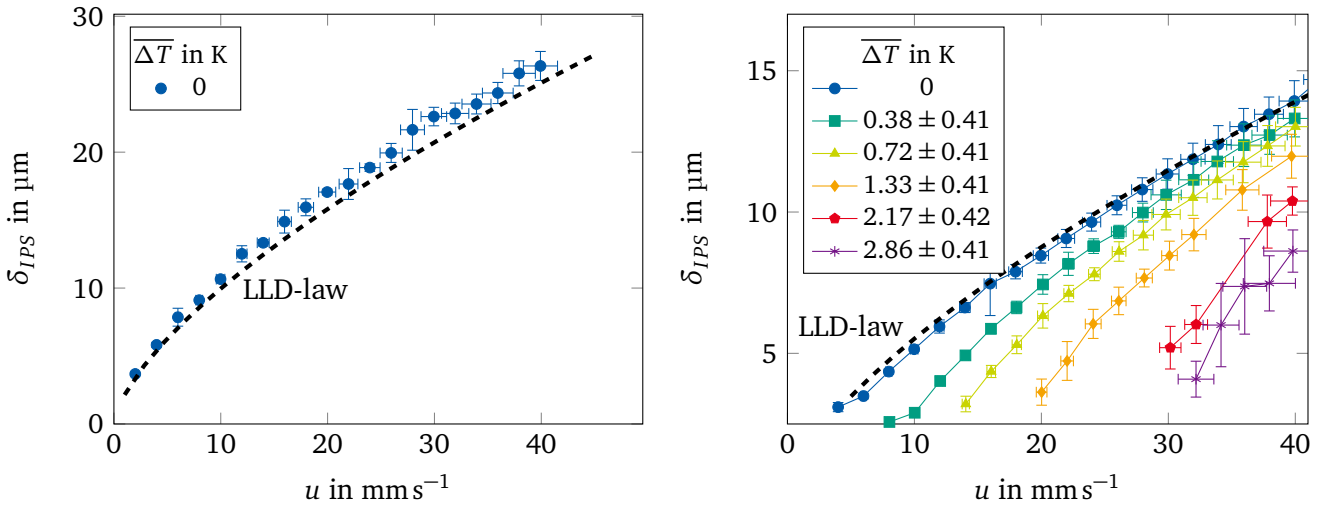

(a) ethanol **(b)** FC-72

Figure 4.2: Steady state film thickness δ_{IPS} measured by interferometry at different dewetting velocities u and wall superheats $\overline{\Delta T}$ for (a) ethanol and (b) FC-72.

δ_{IPS} for ethanol is shown in Figure 4.2a. As explained in section 3.4, δ_{IPS} for ethanol could only be obtained for the isothermal reference case without wall superheat, $\overline{\Delta T} = 0$. Here, the measurement data closely follows the LLD-law, Equation 2.17. Therefore, as no thinning due to evaporation can occur in the isothermal reference case, it can be assumed that $\delta_0^{eth} = \delta_{IPS} = \delta_{LLD}$ for $\overline{\Delta T} = 0$.

δ_{IPS} for FC-72 is shown in Figure 4.2b over the dewetting velocity u for varying degrees of wall superheat $\overline{\Delta T}$. Similarly to ethanol, the film thickness for $\overline{\Delta T} = 0$ closely follows the LLD-law. For constant $\overline{\Delta T} > 0$, the trend of the data stays similar to the LLD-law, but δ_{IPS} decreases with increasing $\overline{\Delta T}$. When extrapolating each curve at $\overline{\Delta T} = const.$ towards smaller values of δ_{IPS}, $\delta_{IPS} = 0$ can be expected at a finite value $u > 0$. This does not permit the conclusion, however, that no microlayer is formed below this velocity. Rather, this corresponds to the velocity, below which the microlayer is too short to reach the measurement location. Furthermore, extrapolating each curve of $\overline{\Delta T} = const.$ towards high u, one can expect all data to converge with the LLD-law. However, the measurement uncertainty of δ_{IPS} and u slowly increases towards higher values of ΔT and u, which makes a comparison of the data increasingly difficult. The increasing measurement uncertainty in δ_{IPS} indicates that the film becomes increasingly unstable towards high ΔT.

Considering the measurement location of δ_{IPS}, the thickness of the microlayer will have decreased by some amount $\Delta\delta = \delta_0 - \delta_{IPS}$ when reaching the measurement location. At $u = const.$, $\Delta\delta$ is thereby expected to increase with ΔT because the fluid evaporates more rapidly. At $\Delta T = const.$ and varying u, on the other hand, $\Delta\delta$ is expected to decreases with increasing u because the measurement location is reached more quickly. Consequently, $\Delta\delta$ should ultimately converge to zero towards high u, because the evaporation between y_0 and the measurement location becomes increasingly negligible. Therefore, δ_{IPS} is expected to converge towards δ_0 at high u. Hence, the data presented in Figure 4.2b suggests that $\delta_0^{FC} = \delta_{LLD}$ for all

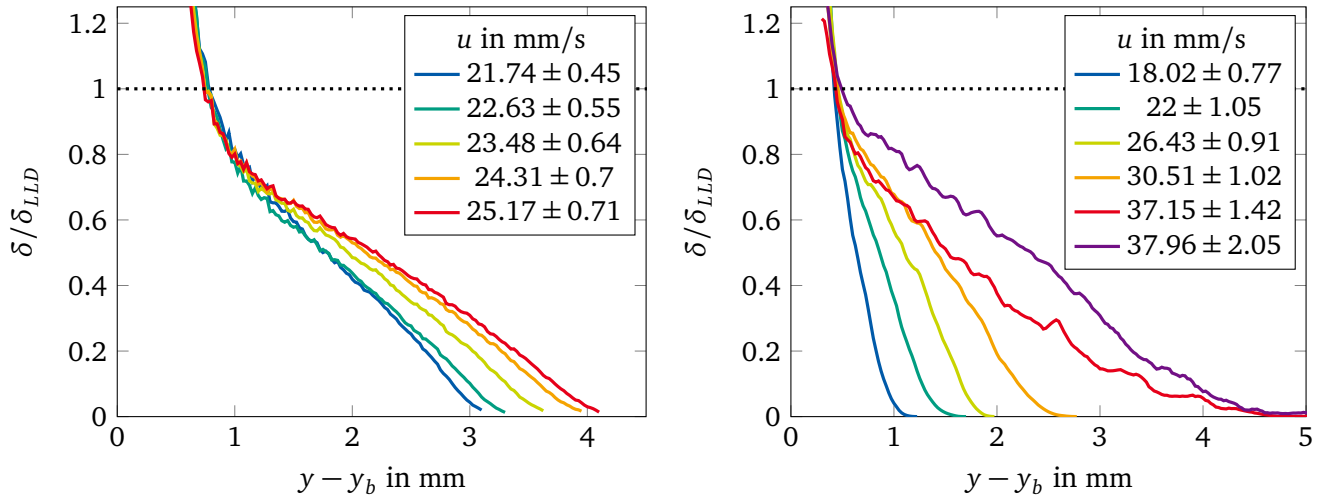

(a) ethanol

(b) FC-72

Figure 4.3: Comparison of the microlayer profiles to δ_{LLD} for varying dewetting velocity u. (a) ethanol at $\overline{\Delta T} = 6.56 \pm 0.71\,\mathrm{K}$ and (b) FC-72 at $\overline{\Delta T} = 2.66 \pm 0.49\,\mathrm{K}$.

ΔT. Thus, the seen dependency of δ_{IPS} on ΔT is entirely caused by the evaporation between y_0 and the location of the thickness sensor.

While no data for $\overline{\Delta T} > 0$ is available for ethanol, it seems reasonable to assume that the conclusions drawn for FC-72, $\delta_0 = \delta_{LLD}$, also holds for both liquids. This conjecture is further tested by comparing δ_{LLD} to the thickness profiles obtained with δ_{con}, which is displayed in Figure 4.3 for a constant $\overline{\Delta T}$ and varying u. As above, Figure 4.3a and Figure 4.3b correspond to ethanol and FC-72, respectively . The thickness profiles are normalized by δ_{LLD} and plotted over the distance from y_b. As the microlayer length of the shown profiles differs, the profiles overlap in the dynamic meniscus region and start diverging at y_0. For FC-72, the thickness at the point of divergence agrees well with $\delta/\delta_{LLD} = 1$, which is indicated by the dotted line. Therefore, the above assumption $\delta_0 = \delta_{LLD}$ agrees well with the microlayer thickness profiles.

For ethanol, on the other hand, the situation is not as clear. The profiles also overlap for low $y - y_b$, but the point of divergence cannot be located very accurately. In contrast to FC-72, the curvature of the thickness profiles near the dynamic meniscus region is much larger due to the increased capillary length l_c for ethanol. In Figure 4.3a, y_0 could, therefore, also be located at $y - y_b = 1\,\mathrm{mm}$, which coincides with $\delta/\delta_{LLD} \approx 0.75$. However, this strongly disagrees with the analysis of δ_{IPS} presented earlier. In addition, the negative deviations from the LLD-law would need to be explained. This is known to occur due to gravitational drainage, which can be described by Equation 2.19 proposed by White and Tallmadge [162]. For the experimental parameters in Figure 4.3a, however, the difference between the LLD-law and Equation 2.19 is only about 6%, which is too small to be the lone cause for the seen deviation. In microchannels, inertia has also been identified as a cause of thinning, as expressed by Equation 2.15. The given correlation, however, cannot directly be applied to the used dip-coating set-up, but the effect can be expected to be present, as it is linked to the flow field in the dynamic meniscus region [56]. In microchannels the inertial thinning

has been observed for low Re, which is in agreement with the experiments presented in this work. In contrast, thinning showed to be significant for Ca > 0.02 in microchannels, which is one order of magnitude larger than Ca in the experiments presented here. A third mechanism leading to a negative deviation from the LLD-law is acceleration as described by Han and Shikazono [57]. This effect, however, is also likely negligible because the measurement data is only evaluated in the steady state, where the sample velocity is practically constant.

Overall, none of the three mechanisms considered above are likely to explain the disagreement of $\delta_0 = \delta_{LLD}$ and the thickness profiles for ethanol. Therefore, it has to be considered that δ_{con} itself is slightly erroneous for ethanol. This is unlikely, however, because the used evaluation method does not differ from that used for FC-72, where good agreement between δ_{IPS} and δ_{con} was found. In conclusion, it cannot be said for certain how δ_0 is best described for ethanol. As the LLD-law was shown to agree with the $\Delta T = 0$ reference case and with both δ_{IPS} and δ_{con} for FC-72, δ_{LLD} is used to describe δ_0 for both fluids.

4.1.2 Formation process of the microlayer

The microlayer thickness profile during the formation of the microlayer is illustrated in Figure 4.4 for the example of ethanol at a wall superheat $\Delta T = 5.9\,\mathrm{K}$ and a dewetting velocity $u = 20.11\,\mathrm{mm/s}$. Each profile corresponds to a different time step at $t - t_{start}$, where negative values indicate $u = 0$. The profile at $t - t_{start} = -40\,\mathrm{ms}$, therefore, corresponds to the static meniscus and the contact line is located at $y - y_{sta} = 0$. The graph on left hand side shows the local film thickness for the times $-40\,\mathrm{ms} \leq t - t_{start} \leq 160\,\mathrm{ms}$, while the times $160\,\mathrm{ms} \leq t - t_{start} \leq 480\,\mathrm{ms}$ are shown in the graph on the right. The profile at $t = 160\,\mathrm{ms}$ is displayed in both graphs. The horizontal dashed line indicates δ_{LLD} for comparison with the above discussion. Please note that many of the profiles shown do not reach zero thickness at the contact line but end at some finite δ. This is caused by the gradient with which the liquid approaches the contact line, which is much greater for a finite apparent contact angle than in the presence of a microlayer. As a result, the contact line cannot be resolved sufficiently due to thermal blurring and no data is available close to the contact line for contact angles much greater than zero.

At $t - t_{start} = 0$ the dewetting process starts, a dynamic meniscus forms, and the contact line moves with the sample in positive y-direction. At 60 ms the dynamic meniscus has reached a maximum height and its shape appears smooth. As the wall keeps moving, the contact line is dragged along with it, but the dynamic meniscus does not follow. Instead, the dynamic meniscus recedes, as seen in the profile at 80 ms. A bulge thereby appears and connects the dynamic meniscus, moving in negative y-direction, to the contact line, moving in positive y-direction. At 120 ms, the meniscus height does not decrease any further. As the contact line continues to be dragged upwards by the moving wall, the thickness of the bulge increases, but the thickness of its connection to the dynamic meniscus decreases. This gives rise to a thickened ridge. It is important to note that during this formation process, the contact line velocity is smaller than the wall velocity. Consequently, liquid is dragged into the ridge by the wall, where it

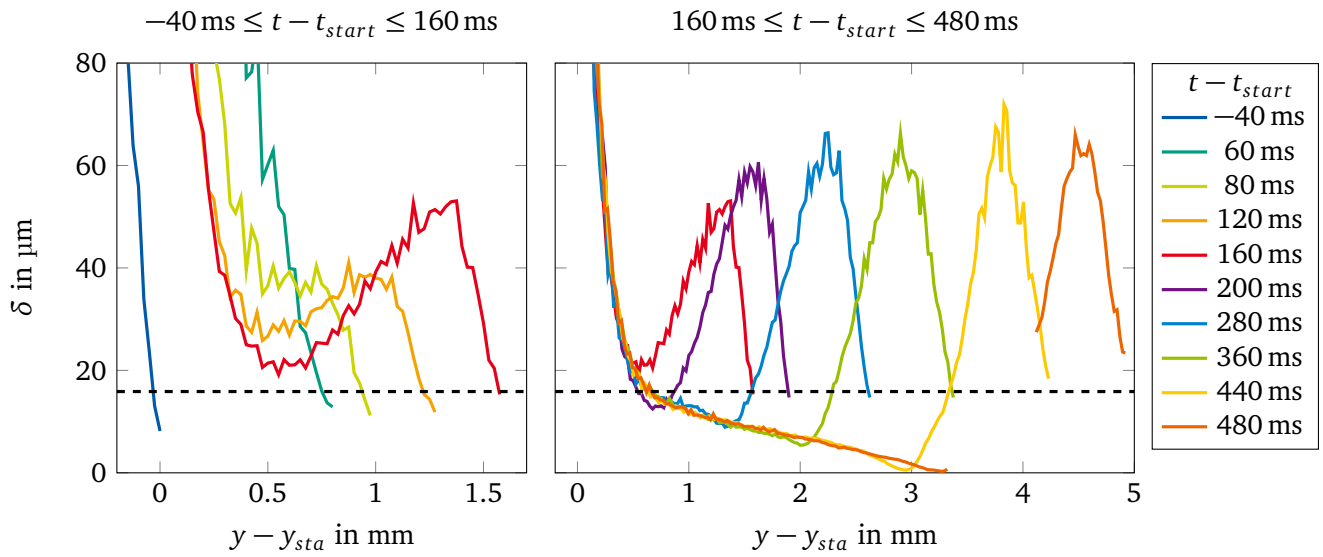

Figure 4.4: Formation process of the microlayer and dewetting ridge for ethanol at $\Delta T = 5.9\,\mathrm{K}$ and $u = 20.11\,\mathrm{mm/s}$. The dashed line marks δ_{LLD}.

accumulates, which explains the seen increase in thickness of the ridge with time [138]. As the distance between ridge and dynamic meniscus increases, the microlayer emerges as a connection between both, which can be seen clearly by comparing the profiles at 200 ms and 280 ms. Due to evaporation within this connecting microlayer region, the thickness of the connection between the end of the (soon to be) microlayer and ridge continues to decrease in time. Hence, the mass flux entering the ridge decreases. At 440 ms, the thickness at the connection to the ridge has decreased to zero, which marks the end of the formation process of the microlayer. The detached ridge continues to move upward with the wall while it evaporates.

Ridge thickness δ_r

The dewetting ridge described above and sketched in Figure 4.4 is observed for both ethanol and FC-72. The thickness of this ridge δ_r is evaluated in Figure 4.5 over the dewetting velocity u for different levels of wall superheat $\overline{\Delta T}$. The data for ethanol was inferred from the thickness profiles δ_{con} and calculated by finding the maximum thickness of the ridge for every time step during the formation process of the microlayer. A mean value was then obtained in between those time steps, where the thickness of the ridge had stopped growing significantly but was still attached to the microlayer. In Figure 4.4, this equals the time between 200 ms and 440 ms. The standard deviation of the maximum over time is used as a measure of measurement uncertainty. For FC-72, the ridge thickness δ_r is directly obtained from the interferometric measurements δ_{IP} and corresponds to the maximum in film thickness at the beginning of the measurement. The reader is referred back to Figure 3.20a in section 3.4.4 for a visual impression. It should be noted that

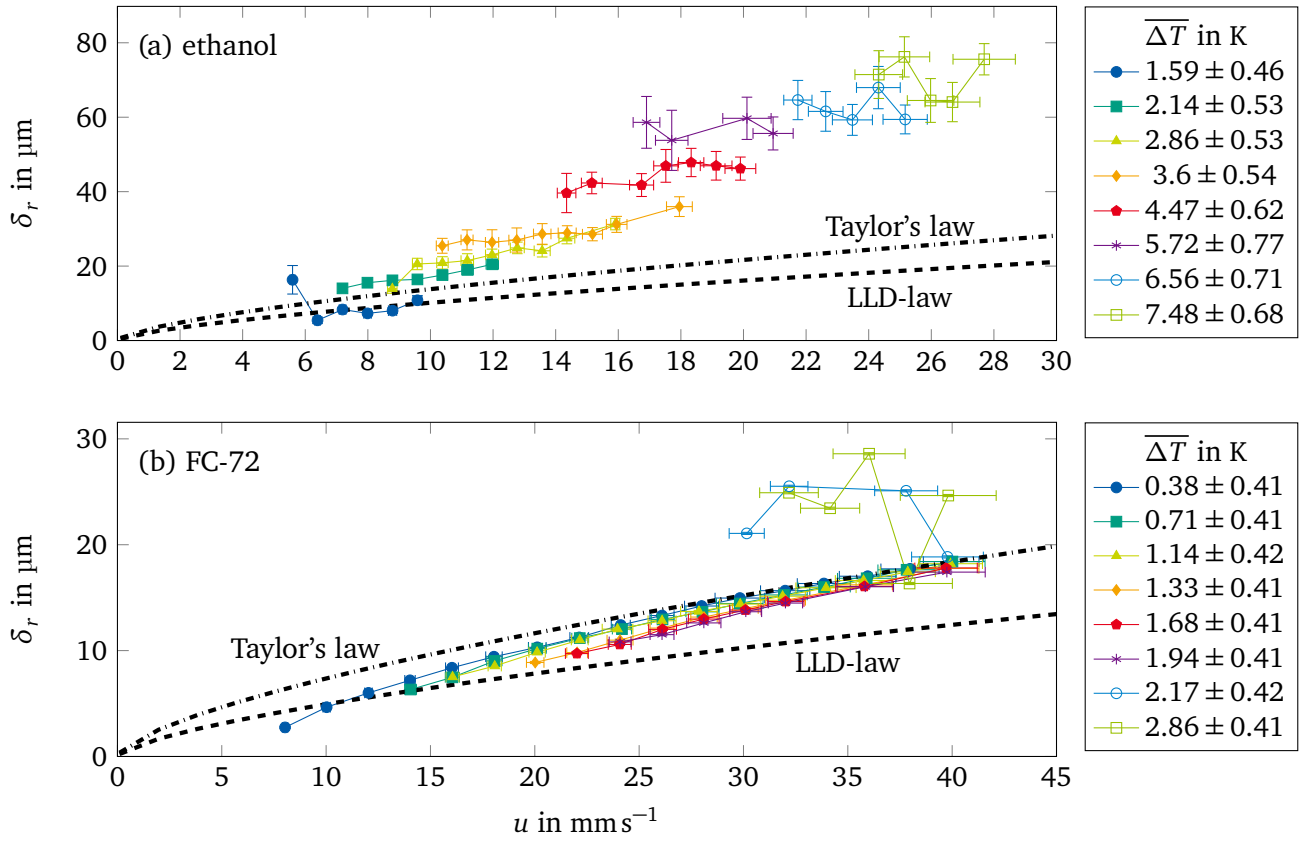

Figure 4.5: Thickness of the dewetting ridge δ_r at the front of the microlayer over the dewetting velocity u for different $\overline{\Delta T}$. (a) ethanol, δ_r obtained from δ_{con}. (b) FC-72, δ_r obtained from δ_{IP}. The dashed and dotted-dashed lines correspond to Equation 2.17 and Equation 2.13, respectively.

the same trend is found, when evaluating δ_r based on the thickness profile δ_{con} for FC-72. Measurement uncertainty and scatter, however, is much larger for δ_{con}, which is why δ_{IP} is used for evaluation.

The obtained data for ethanol and FC-72 are shown in Figure 4.5a and Figure 4.5b, respectively. For both liquids, the LLD-law is plotted alongside the data for comparison. For ethanol, the ridge thickness δ_r shows a clear increase with $\overline{\Delta T}$, but a dependency of δ_r on the dewetting velocity u can only be observed for low ΔT. At higher ΔT, the data becomes increasingly scattered and the dependency on ΔT appears to weaken.

For FC-72, the dependency of the ridge thickness δ_r on ΔT is far less pronounced and most data strongly converges into a single curve with increasing u. Following the argumentation for the thickness measured by interferometry δ_{IPS} in section 4.1.1, the evaporative thinning before the dewetting ridge reaches the measurement location of the interferometric probe can also be assumed negligible at large dewetting velocity u. Taylor's law (Equation 2.13) for a hypothetical channel size $d = l_c$ is indicated by the dotted-dashed line, which converges with the measurement data towards high u. Consequently, it is concluded that the ridge thickness δ_r initially follows Taylor's law for low ΔT for FC-72. This finding is surprising because

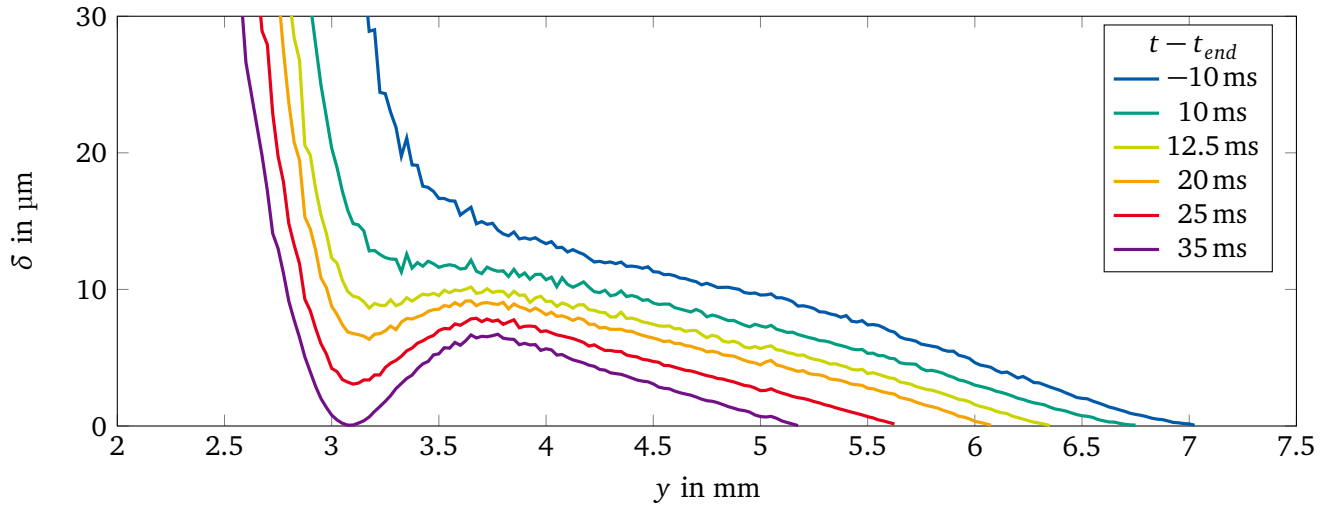

Figure 4.6: Depletion process of the microlayer (ethanol, $u = 27.69\,\mathrm{mm\,s^{-1}}$, $\Delta T = 7.55\,\mathrm{K}$).

Taylor's law is a correlation for δ at high Ca, which does not apply here. In addition, Taylor's law is defined in the context of microchannels and the agreement is found by assuming a channel width of $d = l_c$. The agreement with the measurement data could, therefore, well be a coincidence. Pronounced deviations from Taylor's law then emerge for $\overline{\Delta T} > 1.95\,\mathrm{K}$. As this data is rather scattered, however, a dependency on either ΔT or u cannot be observed. This sudden change in δ_r above a threshold value in ΔT is further addressed below in section 4.2.

4.1.3 Depletion process of the microlayer

At $t = t_{end}$ the dewetting velocity is reduced to $u = 0$ and the microlayer left on the solid substrate depletes rapidly through evaporation. This transient depletion process can be seen as similar to the depletion of the microlayer in nucleate boiling, when the bubble reaches its departure diameter. Hence, it is also analyzed here. In Figure 4.6, the depletion process is displayed for an exemplary measurement for ethanol and each of the shown curves corresponds to an instantaneous thickness profile at $t - t_{end}$. Negative values thereby indicate steady state, i.e. before reduction of the dewetting velocity from $u = const.$ to $u = 0$ is initiated. Once u is reduced, the microlayer rapidly decreases in thickness near the meniscus region and a crest like shape is formed. As the dynamic meniscus recedes and returns to the static meniscus height, dry-out is reached first close to the meniscus region, while the rest of the microlayer remains on the substrate and evaporates.

The described process is very similar to the observations of Chen et al. [15] and Utaka et al. [152] in nucleate boiling, illustrated in Figure 2.4b, where the crest-like shape emerges near the end of bubble expansion. While the authors supply little explanation for the cause of the effect, it is argued that increasing

buoyancy forces near the end of bubble expansion are likely of importance. This, however, is not the case in the experiments presented here and another explanation shall thus be attempted. As concluded in section 4.1.1, the initial microlayer thickness δ_0 is highly dependent on u, which decreases during the deceleration of the solid substrate. Since the duration needed to decrease u to zero is finite, δ_0 deposited during the stopping procedure is not uniform. Hence, a crest-like shape is expected to be deposited, even without evaporation, if the deceleration of the substrate is not infinite. With evaporation, the local minimum in the thickness profile close to the meniscus region is likely subject to temperature driven Marangoni instability, which accelerates the emergence of the crest structure. Furthermore, the meniscus rise also reduces with u and returns to that of a static meniscus, which further contributes to the emergence of the local minimum. With the exception of the meniscus rise, the given analysis can be transferred to nucleate boiling and the experiments of Chen et al. [15] and Utaka et al. [152], because bubble growth slows near the point of maximum bubble expansion. In addition, the observation of this effect in the presented experiments further supports the assumption that microlayers underneath vapor bubbles and those investigated in this work are indeed comparable.

4.2 Transition between the contact line and microlayer evaporation regime

Formation of a microlayer is not always observed. This is illustrated in Figure 4.7, where the dewetting velocity u is mapped over the wall superheat ΔT for all experiments. Their corresponding dimensionless quantities, the capillary number Ca and the Jakob number Ja, are shown on a second pair of axis on the right and top of the graph, respectively. If no microlayer formation was observed during the experiment, i.e. the microlayer length h was zero, a circle is used to mark the experiment. In contrast, a square indicates that a microlayer of any length formed during the experiment. For both ethanol and FC-72, shown in Figure 4.7a and Figure 4.7b, respectively, the same trend is clearly visible. At constant wall superheat ΔT, a threshold velocity needs to be surpassed in order for a microlayer to form. As ΔT is increased, so does this critical velocity u_{cr}. In the following, u_{cr} is therefore also referred to as the regime boundary between the *contact line evaporation regime* (CER) and the *microlayer evaporation regime* (MER).

In the case of ethanol, the data suggests that a finite critical velocity $u_{cr,0} > 0$ exists at $\Delta T = 0$, which corresponds to ethanol being partially wetting in equilibrium. As mentioned in section 3.1.3, the equilibrium contact angle for ethanol could not be measured in a sessile drop experiment, as it is too small to be resolved. Therefore, the existence of a finite critical velocity in equilibrium, $u_{cr,0}$, for ethanol could be a consequence of a small, but finite, equilibrium contact angle between $0 < \theta_e < 10°$. However, if this was the only cause, $u_{cr,0}$ inferred from Figure 4.7 should coincide with $u_{cr,0}$ obtained from an isothermal experiment, where $\Delta T = 0$. Unfortunately, this is not the case. $u_{cr,0}$ inferred from Figure 4.7a is approximately $u_{cr,0}^{eth} = 1.83\,\mathrm{mm/s}$, while a film of finite thickness is still measured with the interferometric probe at $u = 1\,\mathrm{mm/s}$ for $\Delta T = 0$. Unfortunately, the stick-slip effect prevents accurate experiments below this dewetting velocity, and the true value of $u_{cr,0}^{eth}$ can thus not be determined.

As $u_{cr,0}^{eth}$ cannot entirely be explained by a finite equilibrium contact angle, other explanations have to be considered. A systematic measurement error in the dewetting velocity is highly unlikely because low values of u can be very accurately obtained and, in addition, agree well with the appointed motor velocity. Another possibility would be a systematic underestimation of the wall superheat ΔT. In order to produce a shift in ΔT large enough for the observed trend to agree with $u_{cr,0} = 0$, however, an offset of at least 0.75 K in ΔT is needed. This is also unlikely, because it is much larger than the estimated measurement uncertainty and,

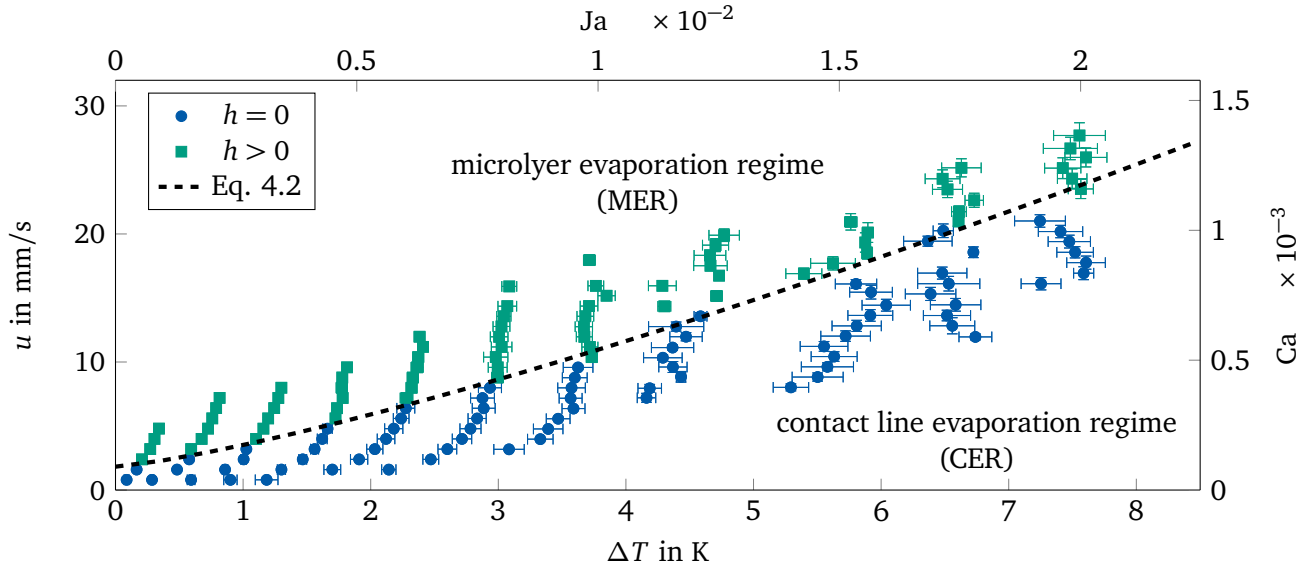

(a) ethanol

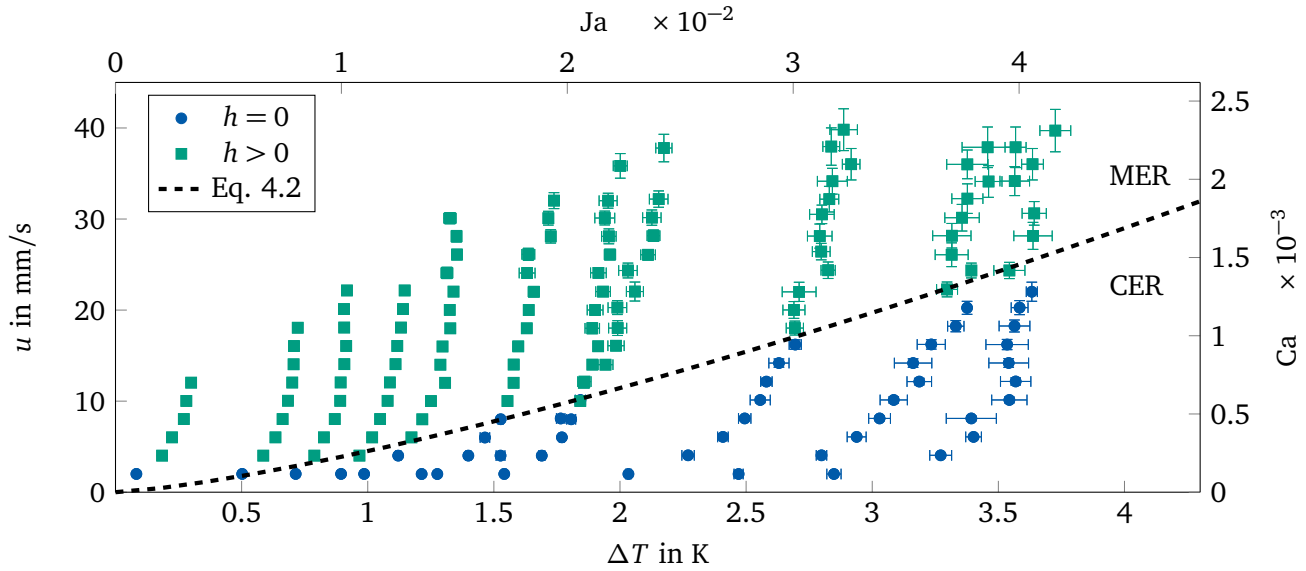

(b) FC-72

Figure 4.7: Regime map of (a) ethanol and (b) FC-72. The dashed line marks the regime boundary estimated based on Equation 4.2.

in addition, no such deviation is seen between the temperature measured by with the Pt-1000 and the temperature of the unheated edge of the sample measured by the infrared camera. Overall, it is likely that $u_{cr,0}^{eth} = 1.83\,\mathrm{mm/s}$ in Figure 4.7a is caused by a combination of the measurement uncertainty in ΔT and a very small finite equilibrium contact angle θ_e.

As the exact cause and magnitude for $u_{cr,0}$ cannot be identified, $u_{cr,0}$ is only inferred from Figure 4.7. To compare the regime maps of both liquids and deduce a description of the regime boundary, dimensionless quantities are used in the following. This leads to $\mathrm{Ca}_{cr,0}^{eth} = 9\times10^{-5}$ and $\mathrm{Ca}_{cr,0}^{FC} = 0$ for ethanol and FC-72, respectively. For each constant $\overline{\Delta T}$, a correlation for the regime boundary Ca_{cr} is obtained by linear interpolation between the lowest velocity, for which a microlayer was observed, and the highest velocity, for which no microlayer was observed. The data for both liquids is each fitted to a power law:

$$\mathrm{Ca}_{cr} - \mathrm{Ca}_{cr,0} = a_{cr}\mathrm{Ja}^{b_{cr}}, \tag{4.2}$$

which yields $a_{cr}^{eth} = 0.154 \pm 0.09$ and $b_{cr}^{eth} = 1.27 \pm 0.15$ for ethanol, and $a_{cr}^{FC} = 0.109 \pm 0.08$ and $b_{cr}^{FC} = 1.34 \pm 0.22$ for FC-72. The fits are indicated in Figure 4.7 by the dashed lines and are referred to as the regime boundary in the following. It should be noted that the uncertainty in the obtained coefficients allows for both liquids to share the same value for the exponent b_{cr}. Indeed, the data for both liquids is also described well by a mean value of $b_{cr} = 1.3$.

4.2.1 Mechanism determining microlayer formation

While the dependency of the critical capillary number Ca_{cr} on the Jakob number Ja is well described by Equation 4.2, the mechanism responsible for the seen effect is still unclear. One might suggest that the formation of a microlayer is simply driven by the mass flux evaporated at the contact line [35]: If this mass flux was equal to the mass entrained into a hypothetical microlayer, no microlayer would be formed. Ca_{cr} would then correspond to the velocity, at which more mass is entrained into the contact line region than could be evaporated there. Hence, a microlayer is formed. This conjecture can be easily tested by analysis of the heat flux during the regime transition. To support the conjecture, the total heat flux should be continuous and directly proportional to the dewetting velocity u in both evaporation regimes. As will be shown in section 4.3, however, this is not the case. Thus, further effects in addition to evaporation must be considered.

The regime transition observed in the presented experiment is strikingly similar to the forced dynamic wetting transition known from partially wetting liquids discussed in section 2.2.3. Not only does Ca_{cr} exist, but a dewetting ridge similar to the one described by Snoeijer et al. [138] is also observed. In partially wetting liquids, both these effects are linked to θ_e and analytical expressions exist to describe them. As presented in section 2.1, the evaporative contact angle θ_{ev} increases with the evaporation near the contact line. Therefore, it can be argued that ethanol and FC-72 become strongly partially wetting under superheated conditions. In this case, the regime transition is not determined by the equilibrium

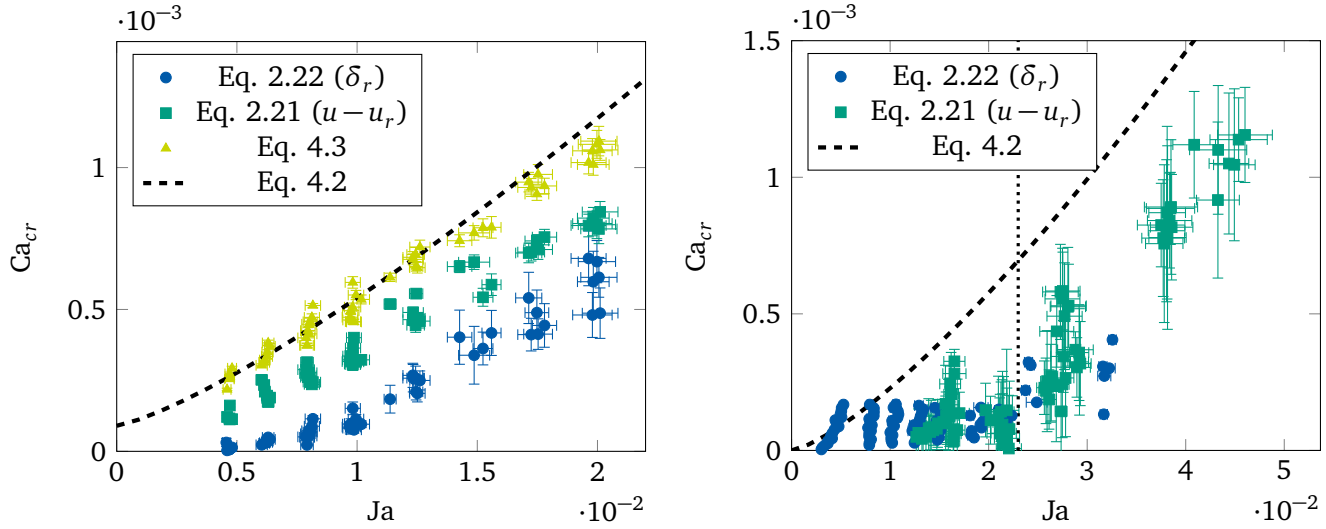

(a) ethanol **(b)** FC-72

Figure 4.8: Comparison of Equation 4.2 to the analytical expressions Equation 2.21 and Equation 2.22 for (a) ethanol and (b) FC-72.

contact angle θ_e, but rather the evaporative contact angle θ_{ev} [38]. Quantitatively, this conjecture agrees well with the measurement data because θ_{ev} increases with ΔT, which would hence lead to an increase in Ca_{cr}. This leaves the highly debated question whether Ca_{cr} is determined by a vanishing macroscopic contact angle and maximum meniscus rise, or rather the mobility of the contact line and the dewetting ridge. Both mechanisms are discussed in the following.

Transition due to ridge formation

If the regime boundary is determined by the formation of the dewetting ridge, the critical capillary number Ca_{cr} obtained above, Equation 4.2, should coincide with Ca_{cr} described by Equation 2.21 and Equation 2.22. The former is thereby dependent on the relative velocity between ridge and wall, $u - u_r$, while the latter is dependent on the ridge thickness δ_r. A comparison of these two equations with the regime boundary obtained above (Equation 4.2) is displayed in Figure 4.8, where Ca_{cr} obtained with all three methods is plotted over Ja. u_r for Equation 2.21 was obtained by tracking the location of the contact line at the upper end of the ridge in the kymograph.

While the trend of the data and Equation 4.2 agree rather well for ethanol displayed in Figure 4.8a, the regime boundary is underestimated by both Equation 2.21 and Equation 2.22. In addition, Equation 2.21 and Equation 2.22 do not coincide themselves, even though they describe the same mechanism. The disagreement with the regime boundary, Equation 4.2, is thereby greater for Equation 2.22, which is calculated with the ridge thickness δ_r. This suggests, that δ_r in the presented experiments is somehow too low for Equation 2.22 to be applicable. Considering that the decrease of the microlayer thickness between y_0 and y_{cl} is in the order of 10 µm, the seen offset is much too large to be caused by evaporation alone. A

possible explanation can be found in the calculation method for the thickness profiles δ_{con}, where a linear temperature profile between solid and liquid-vapor interface is assumed. While this assumption likely holds across the thin microlayer, it can be questioned if it does across the much thicker ridge. However, in this case the offset should become smaller towards low δ_r, i.e. low Ca_{cr} according to Equation 2.21, which is not observed. Another explanation can be found by considering the difference in the formation process of the ridge with and without the effects of evaporation. In both cases, the growth of the ridge is fueled by the liquid dragged into the ridge through its connection with the rest of the film. In contrast to a non-evaporating liquid film, the thickness of this connection is not constant during the formation of a microlayer and eventually vanishes. In combination with the mass lost by evaporation, it seems plausible that the ridge is, therefore, simply not able to reach its maximum height described by Equation 2.22. Thus, evaluating Ca_{cr} on the basis of δ_r leads to an underestimation of Ca_{cr}.

This leaves the disagreement between Equation 2.21 and Equation 4.2 to be explained. The underestimation suggests that the velocity of the ridge in the experiments is larger than in the case without evaporation described by Equation 2.21. A correction factor a_r is, therefore, introduced to Equation 2.21 to describe this phenomenon:

$$\mathrm{Ca}_{cr} = (u - a_r u_r)\frac{\eta}{\sigma}. \tag{4.3}$$

Indeed, agreement with Equation 4.2 is restored for $a_r \approx 0.5$ for ethanol, as shown in Figure 4.8a, where Equation 4.3 is also displayed. The comparison for FC-72 is omitted due to the large scatter in the data. An explanation for the existence of the found value for a_r, however, cannot be given here. Some systematic measurement error in the velocity difference or ΔT of the magnitude needed to restore agreement, however, can quite certainly be ruled out. A possible cause might be the liquid properties limiting the applicability of Equation 4.2. Snoeijer et al. [138] used silicone oil with a viscosity $\mu = 4.95\,\mathrm{Pa\,s}$, which is more than three magnitudes larger than the viscosity of FC-72 and ethanol.

The comparison for FC-72 is shown in Figure 4.8b. As one can expect from the trend seen for the ridge thickness δ_r earlier in section 4.1, the regime boundary Ca_{cr} calculated from the ridge thickness δ_r with Equation 2.22 does not agree with the regime boundary inferred from the observation of a microlayer, i.e. with the regime map. The trend of Ca_{cr} calculated from the ridge thickness (Equation 2.22) abruptly changes above $\mathrm{Ja} \approx 2.3\times10^{-2}$ ($\Delta T = 2.06\,\mathrm{K}$), which is marked by the vertical dotted line. As shown earlier in section 4.1, the ridge thickness δ_r for all data points below $\Delta T = 2.06\,\mathrm{K}$ agree with Taylor's law, while the data above $\Delta T = 2.06\,\mathrm{K}$ suddenly do not (Figure 4.5b). A similar change in trend can also be observed for the regime boundary Ca_{cr} calculated with the ridge velocity u_r (Equation 2.21), even though the data is rather scattered. Below $\mathrm{Ja} \approx 2.3\times10^{-2}$ ($\Delta T = 2.06\,\mathrm{K}$), Ca_{cr} is very low and shows little change with Ja, while a clear dependency can be seen above $\mathrm{Ja} \approx 2.3\times10^{-2}$. Hence, the contact line is rather immobile for low Ja, while increasing above $\mathrm{Ja} \approx 2.3\times10^{-2}$.

The similarity of the trends of Ca_{cr} calculated with $u - u_r$ (Equation 2.21) and with the ridge thickness δ_r

(Equation 2.22) suggests that the sudden increase in the ridge thickness δ_r at higher wall superheat $\overline{\Delta T}$ might be explained by the mobility of the contact line. Below Ja $\approx 2.3\times10^{-2}$, the evaporative contact angle θ_{ev} is low and the contact line thus immobile. Here, the ridge thickness δ_r follows Taylor's law. Towards higher Ja, θ_{ev} increases and the contact line becomes increasingly mobile. This leads to a change in the mechanism determining δ_r from Taylor's law to Equation 2.21. Following the arguments for ethanol, the deviations from Equation 4.2 above Ja $\approx 2.3\times10^{-2}$ are then explained by assuming that for FC-72 the ridge is also unable to reach its maximum theoretical height. Why the described change in mechanism is observed at Ja $\approx 2.3\times10^{-2}$, however, cannot be answered here. It should be noted that such a threshold is not observed for ethanol, which indicates that Ja alone is not sufficient to describe it. Rather, a detailed description of the fluid dynamics close to the contact line including the effects of evaporation on θ_{ev} is likely needed for further study.

Transition due to vanishing apparent contact angle

The possibility exists that the regime transition is determined by the meniscus rise reaching a maximum of $l_c\sqrt{2}$, where the apparent contact angle θ_{app} vanishes. In this case, the critical capillary number Ca_{cr} is described by Equation 2.20, which can be compared to the correlation for Ca_{cr} obtained through the experiments (Equation 4.2). Equation 2.20 is dependent on the slip length l_{slip} and the equilibrium contact angle θ_e, where the latter is to be replaced by the evaporative contact angle θ_{ev} as argued above. Therefore, if Ca_{cr} is indeed determined by a vanishing apparent contact angle, the comparison of Equation 2.20 with experiments presented in this work offers a way of obtaining l_{slip} and θ_{ev}. A statement about the applicability of Equation 2.20 can, however, only be made if either θ_{ev} can be validated or the meniscus rise was measured. Unfortunately, it is not possible with the presented experimental set-up to obtain either. θ_{ev} cannot be measured with the needed accuracy and the location of the free surface of the bulk liquid pool, which is needed to calculate the meniscus rise, is unknown. Therefore, literature data for θ_{ev} is compared to θ_{ev} obtained with Equation 2.20 for evaluation.

θ_{ev} at the regime boundary (Equation 4.2) calculated with Equation 2.20 is displayed in Figure 4.9. As l_{slip} is unknown, solutions for $l_{slip} = 1$ to 100 nm are shown, which is indicated by the shaded area. The solid line marks $l_{slip} = 10$ nm as suggested by [74]. However, from the size of the shaded area for both ethanol shown in Figure 4.9a and FC-72 shown in Figure 4.9b, it can be concluded that θ_{ev} obtained with Equation 2.20 does not strongly depend on l_{slip}. For both ethanol and FC-72, θ_{ev} increases with Ja and the trend, therefore, agrees with the conjecture made earlier. For ethanol, Equation 2.20 thereby agrees rather well with the measurements by Fourgeaud et al. [38], which were carried out on a film of ethanol spontaneously dewetting a vertical plate due to evaporation and gravity. For FC-72, however, such agreement cannot be found. The measurements by Raj et al. [122] were carried out on static evaporating droplets and do not agree with θ_{ev} calculated with Equation 4.2, which over predicts the experiment. Naturally, in contrast to the experiments by Raj et al., the contact line is in motion in the experiments presented in this thesis and θ_{ev} is, thus, expected to differ. However, as the effects of contact line motion

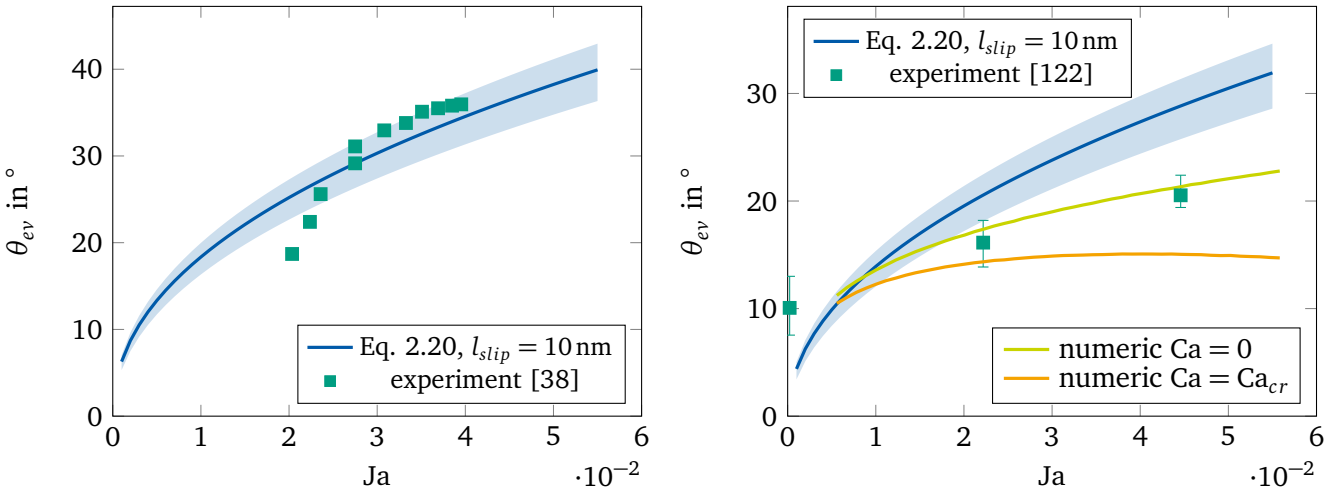

(a) ethanol

(b) FC-72

Figure 4.9: Comparison of θ_{ev} (from Equation 2.20) at Ca_{cr} (from Equation 4.2) with literature data for (a) ethanol and (b) FC-72. The shaded area indicates the variation of l_{slip} between 1 nm (upper limit) and 100 nm (lower limit) and the numeric solutions were obtained with the micro region model of Schlawitschek [128].

rather lead to a decrease in θ_{ev}, the values obtained with Equation 4.2 should be smaller than those presented by Raj et al. Unfortunately, suitable experimental measurements of θ_{ev}, where the contact line is in motion, are not known to the author.

The micro region model presented in section 2.1 offers a convenient way to numerically obtain θ_{ev} as a function of Ca and Ja. The micro region model described by Schlawitschek [128] is used for this purpose and the solutions are also displayed in Figure 4.9b. It is important to note that while Ja refers to the superheat in the bulk liquid region (ΔT), the solutions of the micro region model displayed in Figure 4.9b were obtained using the corresponding local superheat at the contact line ΔT_{cl} for $\text{Ca} < \text{Ca}_{cr}$. The relation between both quantities is approximated from the conducted experiments to $\Delta T_{cl} = 0.93\Delta T$ within the contact line evaporation regime for FC-72, which is shown and further discussed in section 4.3.3. As expected, the solution of the micro region model for $\text{Ca} = 0$ agree well with the measurements by Raj et al. [122]. Furthermore, θ_{ev} obtained for $\text{Ca} = \text{Ca}_{cr}$ is smaller, which is expected and agrees with the conjectures above. However, the trend of θ_{ev} for $\text{Ca} = \text{Ca}_{cr}$ calculated with the micro region model is noteworthy. After an initial increase with Ja, θ_{ev} reaches a maximum and then starts to decrease with Ja. As argued earlier, the regime boundary observed in this work can only be explained by the dependency of θ_{ev} on ΔT. Therefore, the experimentally observed regime boundary Equation 4.2 suggests that θ_{ev} only increases with Ja within the investigated range. Thus, the trend for θ_{ev} obtained with the micro region model at $\text{Ca} = \text{Ca}_{cr}$ does not agree with the experiments presented here.

Two possibilities are proposed to explain this disagreement. Firstly, the effect of velocity on θ_{ev} might simply be too dominant in the micro region model. This seems unlikely, however, because the obtained dynamic

contact angle has been thoroughly validated using dynamic impinging drop experiments [128]. Therefore, it seems more likely that the disagreement is due to the length scale on which θ_{ev} is defined within the context of the micro region model. In the derivation of Equation 2.20, which utilizes the micro angle approach, the microscopic contact line region is asymptotically matched with the macroscopic meniscus region. The length scales of the former and the latter are in the order of 10^{-9}m and 10^{-3}m, respectively [13, 30]. At the regime boundary Ca_{cr}, the slope of the interface on a microscopic length scale equals the imposed microscopic contact angle, and gradually decreases to $\theta_{app} = 0$ at the end of the dynamic meniscus on a macroscopic length scale. The micro region, on the other hand, measures approximately 0.5 µm [128] and θ_{ev} is thus defined much closer to the dynamic meniscus than θ_e, namely right within the intermediate region, where the matching of interface curvature occurs in the context of the micro angle approach. Therefore, the contact angle obtained by the micro region model can be expected to lie somewhere between θ_e assumed by Equation 4.2 and $\theta_{app} = 0$, and show a stronger velocity dependency. As seen in Figure 4.9, this is indeed the case. Consequentially, the contact angle obtained by the micro region model close to Ca_{cr} is neither *microscopic* nor *apparent*, yet not incorrect. θ_{ev} is simply defined on a different length scale and thus not directly comparable with the contact angle imposed by the micro angle approach. It should be stressed that this discrepancy likely only occurs close to Ca_{cr}, where θ_{app} approaches zero. In any other case, the contact angle obtained by the micro region model coincides with θ_{app}, which is finite, and hence agrees with experiments and other models, where the contact angle is imposed directly at the wall.

Concluding remarks concerning the transition mechanism

The measurement data and analysis presented above clearly indicate that the transition between contact line evaporation and microlayer evaporation is very similar to the forced dynamic wetting transition in partially wetting liquids. The regime boundary is, therefore, largely determined by fluid dynamics and the contact angle. The seen dependency on Ja is thus a consequence of the dependency of the contact angle on the wall superheat ΔT. Unfortunately, it cannot be said if the regime boundary in the presented experiments is determined by a vanishing macroscopic contact angle or the mobility of the dewetting ridge. For ethanol, evidence in favor of both was presented. While Equation 2.21 and Equation 2.22 do not directly hold for the experiments, the trends agree rather well and agreement can be restored by correcting u_r. However, θ_{ev} obtained with Equation 2.20 was also plausible and agreed with literature data. For FC-72, the data is inconclusive. While a dewetting ridge was observed, agreement with Equation 2.21 and Equation 2.22 was not very good. In addition, θ_{ev} obtained with Equation 2.20 showed no agreement with literature data or the micro region model. As observed by Gao et al. [43], however, a vanishing contact angle and the appearance of a dewetting ridge might not be mutually exclusive. In section 4.1, it was shown that the dynamic meniscus first reaches a maximum height during the formation process of the microlayer, before it recedes and the dewetting ridge appears. Therefore, it should be investigated if this short-lived maximum meniscus rise is maybe equal to $\sqrt{2}l_c$, which corresponds to a vanishing apparent contact angle.

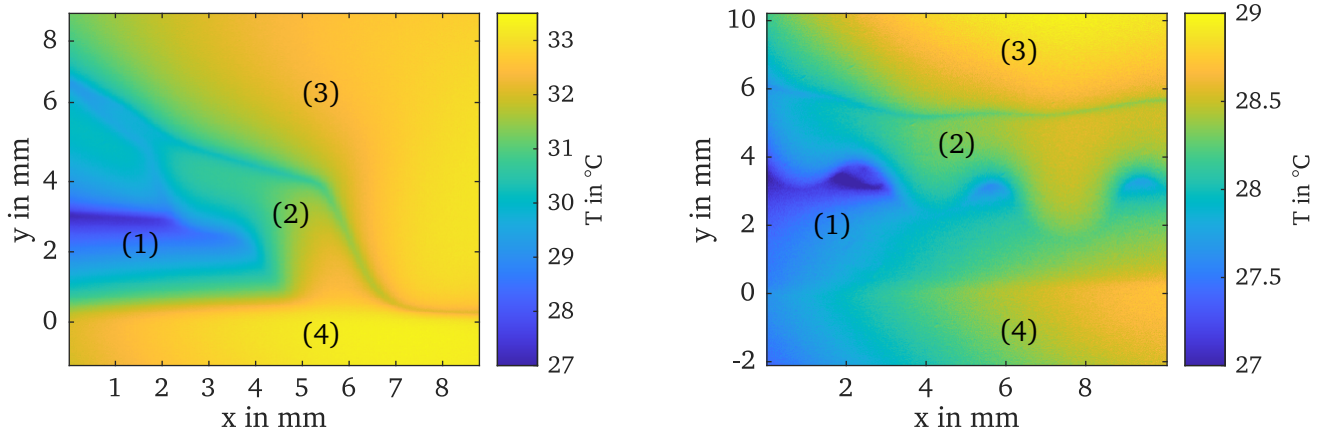

(a) Ethanol at Ja = 2×10^{-2} and Ca = 1.1×10^{-3} ($\approx$ Ca$_{cr}$). **(b)** FC-72 at Ja = 3.4×10^{-2} and Ca = 2.7×10^{-3} ($>$ Ca$_{cr}$).

Figure 4.10: (a) Transitional evaporation regime and (b) unstable dewetting ridge leading to droplet rundown. (1) microlayer, (2) dewetting ridge / thick film, (3) dry wall region, (4) bulk liquid region.

4.2.2 Additional evaporation regimes

Snoeijer et al. [136] pointed out that if the sample velocity remained close to Ca$_{cr}$, the dewetting ridge could be stretched to deposit a film of large thickness. This effect is also rarely observed in the presented experiments and is illustrated in Figure 4.10a. Due to a slight temperature gradient in x-direction across the sample and Ca $\approx$ Ca$_{cr}$, a microlayer (1) is formed in the left area of the FOV, while only contact line evaporation is observed on the far right. Above the microlayer a dewetting ridge (2) exists, whose appearance differs across the sample. On the far left, the dewetting ridge has already detached from the microlayer and has thinned due to evaporation. At $x = 3\,\text{mm}$ the dewetting ridge is still attached to the microlayer and thus still considerably thicker. At $x = 5\,\text{mm}$ the dewetting ridge transitions into a thick film, which is directly attached to the dynamic meniscus without a microlayer in between. Film growth for these films is rather slow and steady state is not reached within the duration of the measurement. Furthermore, the increased thickness of the film leads to reduced evaporation and hence decreased heat flux in comparison to a microlayer of the same length. In Figure 4.10, this is reflected by the low temperatures reached within the microlayer, while the wall remains considerably warmer towards the right of the FOV. These thick films were omitted in the analysis of the regime boundary in section 4.2, but the regime map shown in Figure 4.7 could be extended to include a third evaporation regime that corresponds to the formation of these thick dewetting films. In this case, the contact line evaporation regime and the microlayer evaporation regime are not separated by a boundary as described above but a *transitional* evaporation regime. It should be noted that the thick dewetting films were observed towards the highest ΔT investigated for each fluid in this work. Therefore, the proposed transitional evaporation regime might get broader towards high ΔT.

A different mechanism leading to the local formation of thick films is illustrated in Figure 4.10b. Here, the dewetting ridge (2) above the microlayer (1) is unstable and liquid locally accumulates into droplets.

The mass of these droplets can become very large, so that they are eventually unable to be dragged upwards any further by the movement of the wall and reverse their direction of movement due to gravity. Consequentially, the droplets reattach to the microlayer, even though the dewetting ridge had initially been completely detached. Once reattached, the mass of the droplet is then further increased through its newfound connection. The droplets can reach the dynamic meniscus, which leads to a situation similar to the transitional films discussed above. However, in contrast to Figure 4.10a, Ca in Figure 4.10b is much larger than Ca_{cr} and the described mechanism, therefore, not of transitional nature. While the data is not sufficient to clearly locate this phenomenon in the regime map, it appears to occur for large Ca and Ja and could hence mark an upper limit to the microlayer evaporation regime, where a stable microlayer exists. It should be noted, however, that both mechanisms described above are driven by gravity and, therefore, only occur in vertical dewetting.

4.3 Effects on heat flux

The following section deals with the evaporative heat flux during the dewetting process. The analysis is divided into three parts, in which the shape of the heat flux profile, the integrated heat flux, and the heat flux at the contact line are analyzed separately.

4.3.1 Heat flux profiles

Figure 4.11 shows the median heat flux q_{med} over the vertical coordinate y for different u at a high Ja. Figure 4.11a and Figure 4.11b correspond to ethanol and FC-72, respectively. The y-axis was adjusted to relate to $y_b = 0$ and thus equals the distance above the bulk liquid region. Heat flux profiles in the contact line evaporation regime at $u < u_{cr}$ are indicated by the use of dashed lines, which is true for the lowest u shown for each fluid. Here, only a sharp peak in heat flux is observed at the contact line. The magnitude of this peak is discussed in further detail in section 4.3.3. The shape of the heat flux profile changes as u is increased above u_{cr} and a microlayer is formed. The heat flux quickly rises above the bulk region and reaches a maximum at the contact line. As demonstrated in section 3.4, however, the true value of the contact line peak is not visible in q_{med}, as it is lost in the median data due to the motion of the contact line at the end of the film. Above the contact line, in the dry wall region, heat flux drops to negligible magnitude. The described profile shape is preserved for increasing u in both liquids.

A different shape of the heat flux profile is observed at lower Ja, which is shown in Figure 4.12. Again, Figure 4.12a and Figure 4.12b correspond to ethanol and FC-72, respectively. As expected, a solemn peak at the contact line is also observed for both liquids at $u < u_{cr}$. For $u > u_{cr}$, however, the heat flux profile differs from the shape observed at high Ja. q_{med} still quickly increases above the bulk liquid region, but does not strictly increase towards the contact line. In ethanol, a local maximum is reached at y_0, i.e just at the end of the dynamic meniscus region. q_{med} then decreases until the contact line region is reached, where

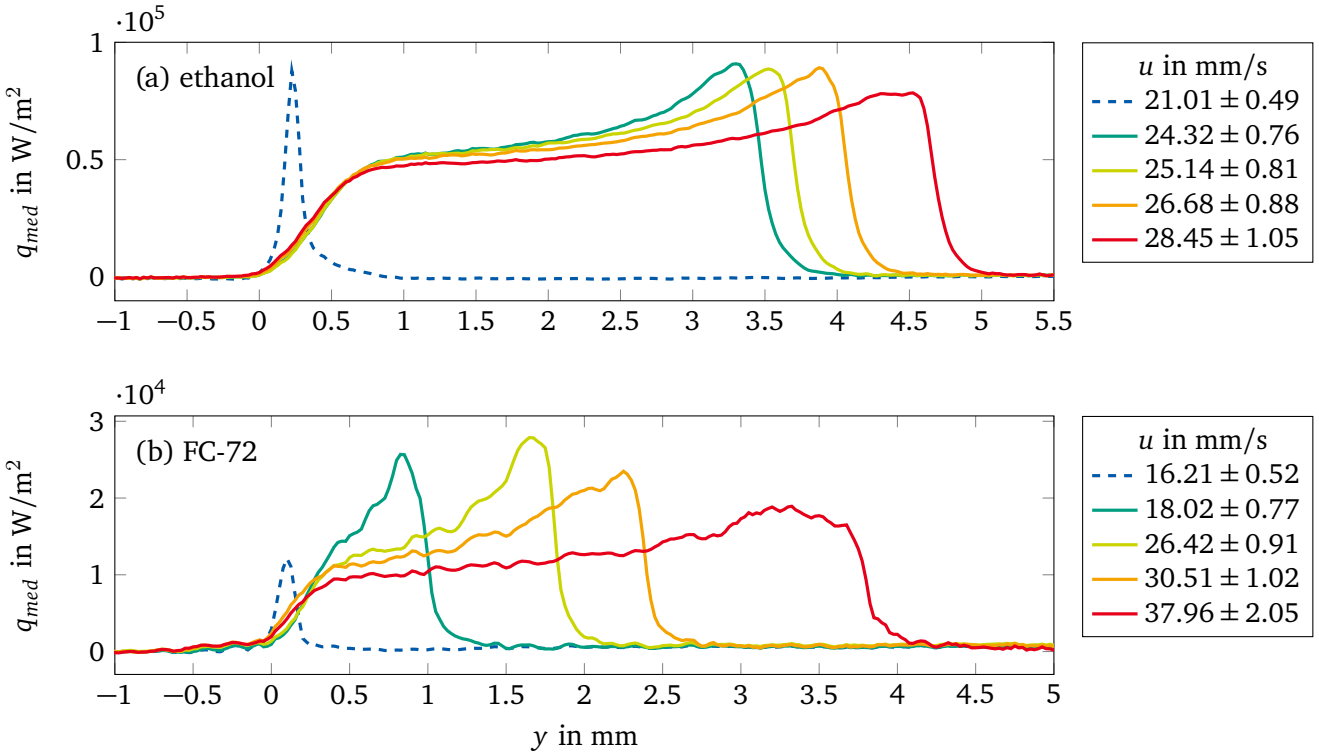

Figure 4.11: Median heat flux q_{med} during the steady state over the vertical coordinate y at high Ja. (a) Ethanol at $\overline{Ja} = (20 \pm 1.7) \times 10^{-3}$, (b) FC-72 at $\overline{Ja} = (30.1 \pm 3.1) \times 10^{-3}$. Dashed lines indicate $u < u_{cr}$ (CER).

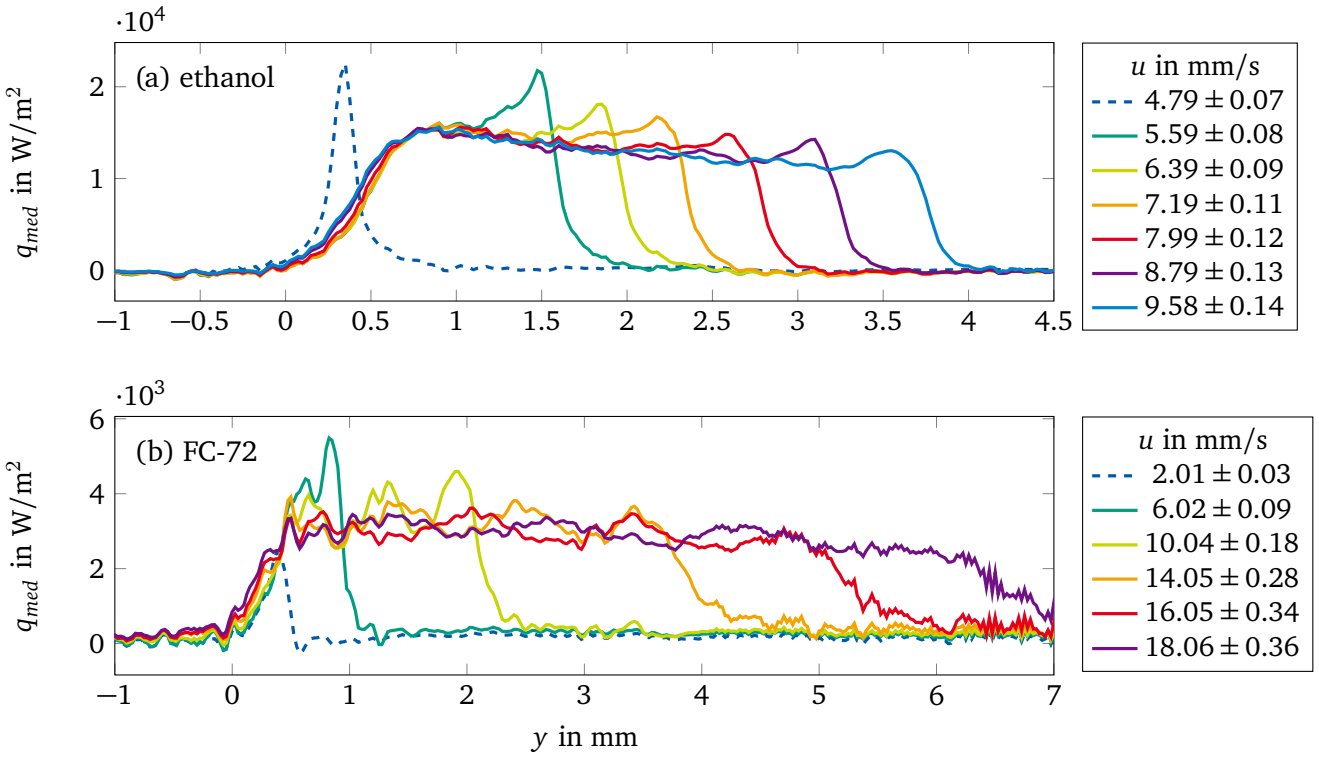

Figure 4.12: Median heat flux q_{med} during the steady state over the vertical coordinate y at low Ja. (a) Ethanol at $\overline{Ja} = (6.7 \pm 0.2) \times 10^{-3}$, (b) FC-72 at $\overline{Ja} = (7.6 \pm 0.9) \times 10^{-3}$. Dashed lines indicate $u < u_{cr}$ (CER).

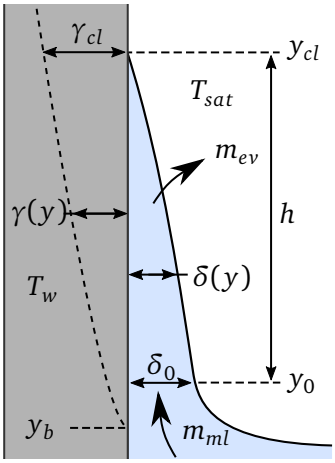

Figure 4.13: Illustration of the microlayer and thermal boundary layer in the steady state.

q_{med} increases again. The magnitude of the peak at the contact line thereby decreases with u and only describes a global maximum for low u. For high u, maximum q_{med} is located at y_0. A similar observation is made for FC-72, which is displayed in Figure 4.12b. An increasing profile can only be observed for $u = 6.02\,\mathrm{mm\,s^{-1}}$, which is very close to u_{cr}. In all other cases, q_{med} does not rise towards the contact line.

Analytical description of the local heat flux

In order to explain the seen difference in the heat flux profile shape, a description for the local heat flux $q(y)$ is derived in the following. The microlayer in steady state is illustrated in Figure 4.13, in which any quantities mentioned or introduced in the following analysis can be found. Since the microlayer is thin, a linear temperature gradient normal the wall is assumed across the microlayer to describe the evaporative heat flux:

$$q(y) = \frac{\Delta T(y)}{R(y)}, \tag{4.4}$$

in which R is the resistance to heat transfer in between the points, where ΔT is defined. As seen in the measurements, the wall temperature beneath the microlayer is not constant and decreases towards the contact line. Hence, the local heat flux through the microlayer is ultimately coupled with the local heat flux within the wall. A description of the change in local ΔT with y is, therefore, needed to solve Equation 4.4 if only heat transfer in the liquid is considered. In addition, this approach requires a treatment of the heat flux singularity at the contact line, where the δ goes to zero. The work of Guo and El-Genk [55] suggests that the heat transfer in the wall might be a limiting factor to the overall heat transfer in the microlayer and should, therefore, be included in the description. Considering the instationary nature of the problem, it is likely that the heat transfer within the wall has boundary layer character. In this case, the temperature deeper within the solid substrate can be assumed constant and equal to the wall temperature measured in

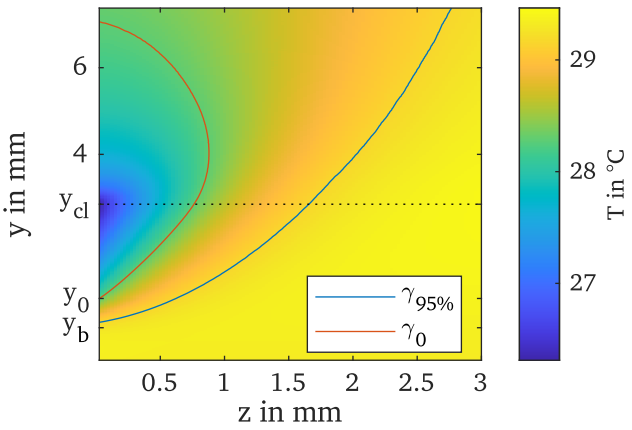

Figure 4.14: Temperature field inside the solid for ethanol at $u = 14.38 \pm 0.29\,\mathrm{mm\,s^{-1}}$ and $\Delta T = 3.85\,\mathrm{K}$.

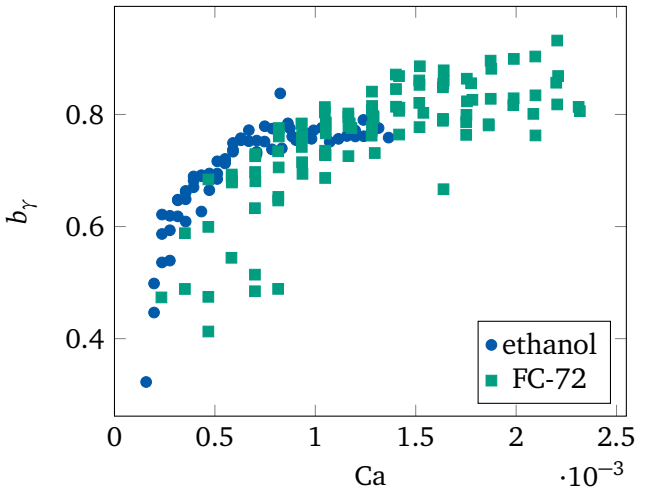

Figure 4.15: Exponent b_γ over Ca for ethanol and FC-72.

the bulk liquid region. Therefore, ΔT in Equation 4.4 is a constant if R describes the combined resistance of microlayer and thermal boundary layer in the solid, i.e. within liquid R_l and solid R_s:

$$R(y) = R_l + R_s = \frac{\delta(y)}{\lambda_l} + \frac{\gamma(y)}{\lambda_s}. \tag{4.5}$$

Therein, γ describes the thickness of the thermal boundary layer inside the solid and λ_l and λ_s are the thermal conductivity of the liquid and the solid, respectively. Additional resistances, such as R_{ev}, are neglected for the purpose of this analysis. For a full description of the problem, functions for both the liquid film thickness $\delta(y)$ and the thickness of the thermal boundary layer in the solid $\gamma(y)$ need to be found. As shown in section 4.1, δ can be assumed to decrease linearly with y in the microlayer region:

$$\delta(y) = \delta_0 \left(1 - \frac{y}{y_{cl}}\right) \qquad \text{for} \quad y_0 = 0. \tag{4.6}$$

To obtain an expression for γ, the temperature field within the solid is analyzed, which is gained directly from the numerical heat flux calculations. The mean temperature field inside the solid during the steady state for an exemplary measurement with ethanol is displayed in Figure 4.14. The minimum distance perpendicular to the solid-liquid interface at $z = 0$, where the wall superheat is at least equal to 95% of the wall superheat in the bulk liquid region, is denoted with $\gamma_{95\%}$. As seen in Figure 4.14, $\gamma_{95\%}$ is not linear, but increases with y non-monotonically and reaches a value $\gamma_{cl,95\%} = \gamma_{95\%}(y_{cl})$ at the contact line. Fitting a power law to $\gamma_{95\%}$ for both ethanol and FC-72 yields good agreement:

$$\gamma(y) = \gamma_{cl} \left(\frac{y}{y_{cl}}\right)^{b_\gamma}. \tag{4.7}$$

The intersection of $\gamma_{95\%}$ with the solid-liquid interface, however, is very close to y_b, the end of the bulk liquid region and beginning of the dynamic meniscus region. As can be expected from the shape of q discussed earlier, significant reduction in ΔT already occurs within the dynamic meniscus region within $y_b \leq y \leq y_0$. Equation 4.6, however, is only valid for $y \geq y_0$. To unify the origin of both δ and γ, either Equation 4.6 has to be extended by a description of the meniscus region, or an alternative measure for γ has to be found. In Figure 4.14, γ_0 describes the minimum distance perpendicular to the solid-liquid interface, where the wall superheat is equal to the wall superheat at y_0. Naturally, $\gamma_{cl,0}$ is much smaller than $\gamma_{cl,95\%}$. In addition, γ_0 appears to be more linear between y_0 and y_{cl}. The exponent b_γ is obtained by fitting γ_0 for each experiment to Equation 4.7 and is shown in Figure 4.15 for both liquids. A strong dependency on ΔT, and thus on the Jakob number Ja, was not observed for either liquid. Therefore, b_γ is only plotted over the capillary number Ca, the non-dimensionless measure for the dewetting velocity u. While the data for FC-72 shows more scatter, b_γ for both liquids follows a similar trend. Towards higher Ca, b_γ approaches unity, while quickly reducing towards lower Ca. The limit of $b_\gamma = 1$ is expected because larger values would result in a nonphysical shape of the thermal boundary layer. However, using γ_0 instead of $\gamma_{95\%}$ for the description of γ requires ΔT in Equation 4.4 to be exchanged with ΔT_0, which is the local superheat at y_0. Combining Equation 4.4, Equation 4.5, Equation 4.6, and Equation 4.7 then leads to an expression for the local heat flux q in the microlayer region:

$$q(y) = \Delta T_0 \frac{\lambda_l}{\delta_0} \left(1 - \frac{y}{y_{cl}} + \alpha \left(\frac{y}{y_{cl}} \right)^{b_\gamma} \right)^{-1} \qquad \text{for} \quad y_0 = 0 \tag{4.8}$$

with

$$\alpha = \frac{\gamma_{cl}}{\delta_0} \frac{\lambda_l}{\lambda_s}. \tag{4.9}$$

α is the ratio of the thermal resistances of wall at the contact line to the initial thermal resistance of the microlayer. If this ratio is very low, the influence of the thermal wall boundary layer is expected to be negligible. As α increases, however, local heat flux reduces and becomes increasingly inhibited by the heat transfer in the wall. A value of $\alpha = 1$ thereby indicates equal importance of the heat transfer in solid and liquid.

α defined here is very similar to the Biot number Bi, which compares the thermal resistance inside the solid to the thermal resistance at the solid surface. However, as Bi is associated with convective heat transfer, the thermal resistance in the fluid at the solid surface is usually described by a (convective) heat transfer coefficient. Naturally, one could interpret the ratio δ_0/λ_l as such. However, this approach might convey the impression that convective heat transfer is related to the problem at hand, but the analysis above is based on linear heat conduction only. As will be shown in section 4.3.2, gravitational drainage within the film does likely exist, however, and it can thus be argued if convective heat transfer can indeed be neglected. In contrast, it can easily be shown that δ_0 is about three magnitudes smaller than the thickness of a velocity

boundary layer in the same fluid on a flat plate. Additionally, in convective heat transfer, the boundary layers in liquid and solid both increase in the direction of the flow. In the presented problem, this is only true for γ, while δ decreases towards the contact line. To emphasize these differences, Bi is not used for the description of heat transfer in the microlayer presented here.

Analysis of the thermal boundary layer

Unknown quantities in Equation 4.8 are the thickness of the thermal boundary layer at the contact line, $\gamma_{cl,0}$, and the superheat ΔT_0 at y_0, which are both expected to be linked to δ_0, ΔT, and the material properties of both fluid and wall. As explained above, $\gamma_{cl,0}$ can be obtained from the experiments and is displayed for ethanol in Figure 4.16 and for FC-72 in Figure 4.17, each in the top graph of the corresponding figures. Naturally, only data points at $\mathrm{Ca} > \mathrm{Ca}_{cr}$ are considered. For low ΔT, $\gamma_{cl,0}$ strongly depends on both ΔT and Ca. For $\overline{\Delta T} = const.$, $\gamma_{cl,0}$ increases seemingly linearly with Ca. For $\mathrm{Ca} = const.$, on the other hand, $\gamma_{cl,0}$ increases with decreasing ΔT.

The two observed trends can be explained by considering the energy required for the evaporation of the microlayer, which is supplied by the wall. At low ΔT, the wall contains less energy per unit depth than at high ΔT. Hence, to evaporate the same microlayer, the energy has to be supplied from further within the wall, which corresponds to a larger γ_{cl}. The same explanation holds for the dependency on Ca due to the increase in δ_0. However, in contrast to the linear relationship observed in the data, one would expect the scaling $\gamma_{cl} \sim \mathrm{Ca}^{5/3}$ because the latent energy needed to evaporate the film is directly proportional to the mass flow entrained into the microlayer m_{ml}. The data, however, is not sufficient for further investigation of this trend. Towards higher ΔT, the above discussed dependencies on Ca and ΔT weaken for both fluids and $\gamma_{cl,0}$ seems to approach a constant value. This value can be estimated to approximately 0.7 mm for ethanol and 0.25 mm for FC-72, which are indicated by the horizontal dotted line. The difference between both fluids is likely explained by the difference in Δh_v, which is about ten times higher for ethanol.

In a next step, the data for $\gamma_{cl,0}$ is used in Equation 4.9 to evaluate α. For this purpose, the initial microlayer thickness δ_0 is calculated with Equation 2.17 for ethanol and FC-72. α is displayed for ethanol in Figure 4.16 and for FC-72 in Figure 4.17, each in the bottom graph of the figures. The trends for both fluids are again very similar: The dependency of α on ΔT and Ca mirrors the dependency seen for $\gamma_{cl,0}$, which is expected because δ_0 is independent of ΔT. Similarly to $\gamma_{cl,0}$, the dependency of α on Ca and ΔT is again lost at high ΔT and the data seems to collapse onto a single curve. This is especially visible in the data for ethanol. Since $\gamma_{cl,0}$ tends towards a constant value and δ_0 further increases with u, it can be expected that α slowly approaches zero with $\alpha \sim 1/\delta_0$, i.e. $\alpha \sim \mathrm{Ca}^{-2/3}$ for FC-72 within the LLD-regime.

While the described trends are the same for both ethanol and FC-72, the absolute values for α differ and larger values are observed in ethanol. This is only a consequence of the larger $\gamma_{cl,0}$ for ethanol because δ_0 is assumed to follow the LLD-law in both fluids. In ethanol, α reaches as low as 0.61 at the highest Ca, indicating that heat transfer within the wall is relevant. Largest α are observed towards low ΔT and high

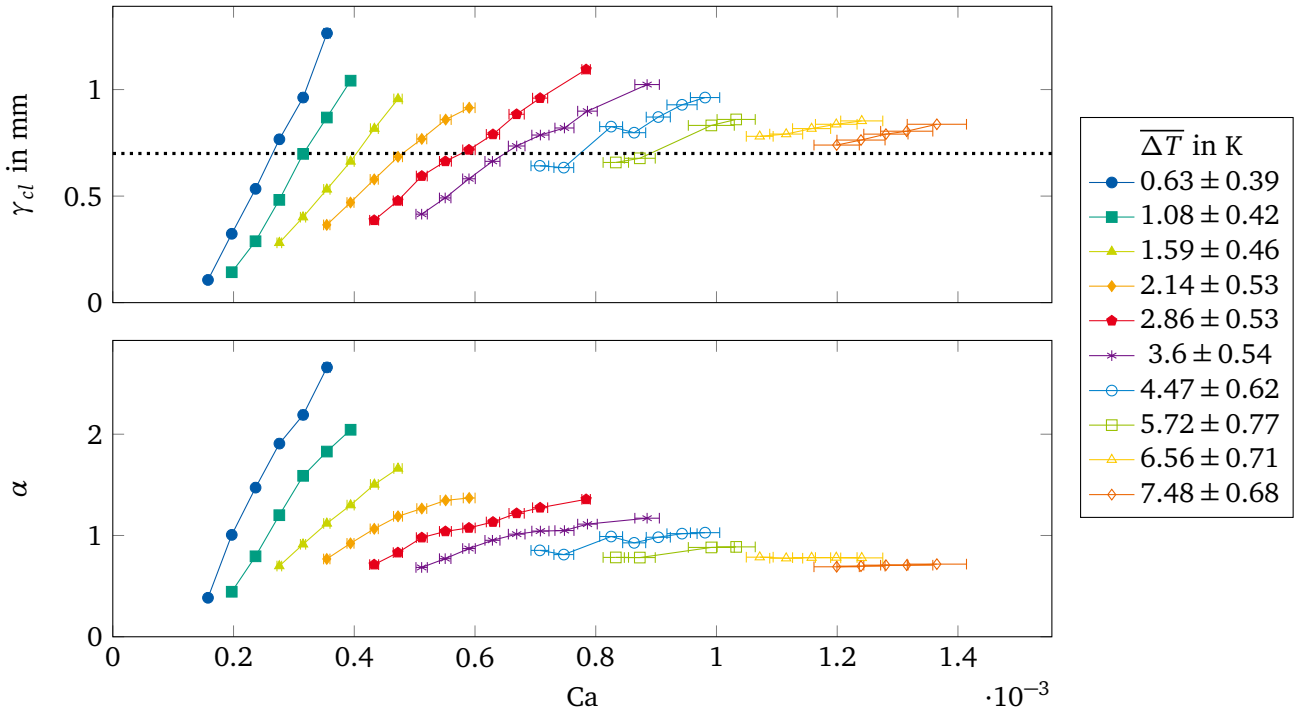

Figure 4.16: Interaction between solid and liquid in ethanol: γ_{cl} (top) and α_h (bottom) over Ca for different wall superheats $\overline{\Delta T}$. The legend applies to both top and bottom.

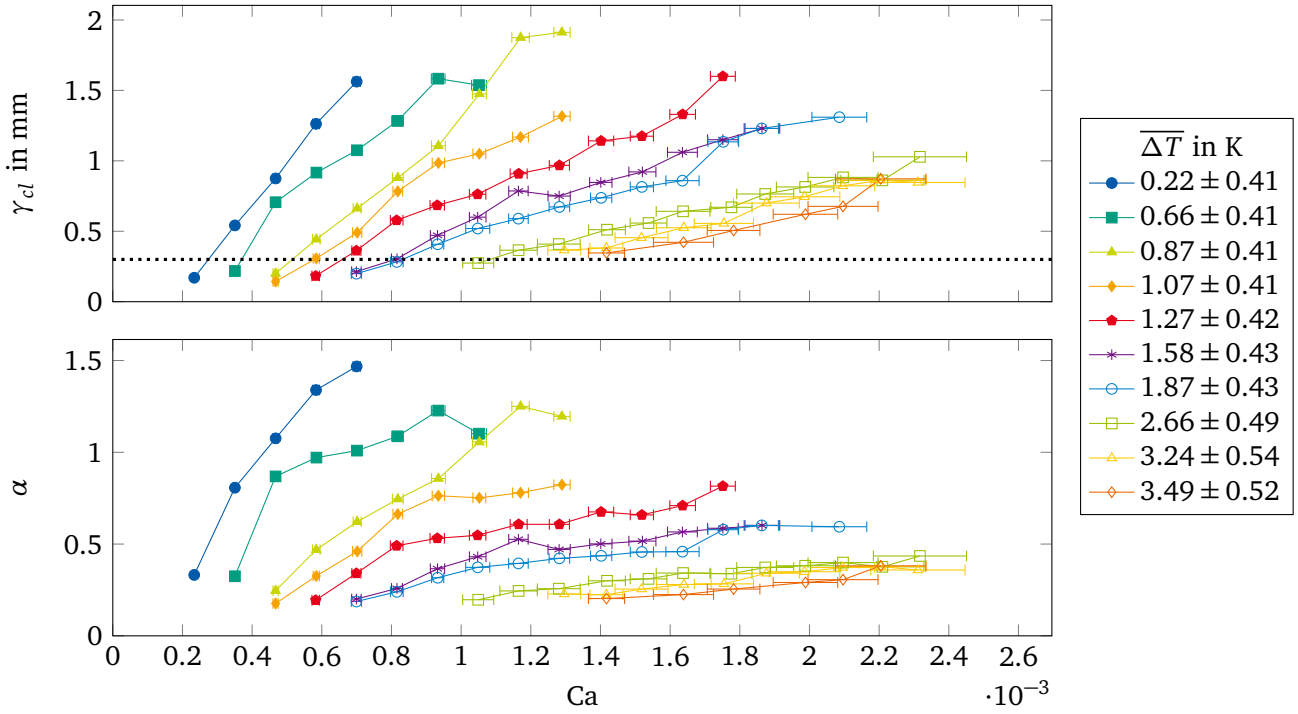

Figure 4.17: Interaction between solid and liquid in FC-72: γ_{cl} (top) and α_h (bottom) over Ca for different wall superheats $\overline{\Delta T}$. The legend applies to both top and bottom.

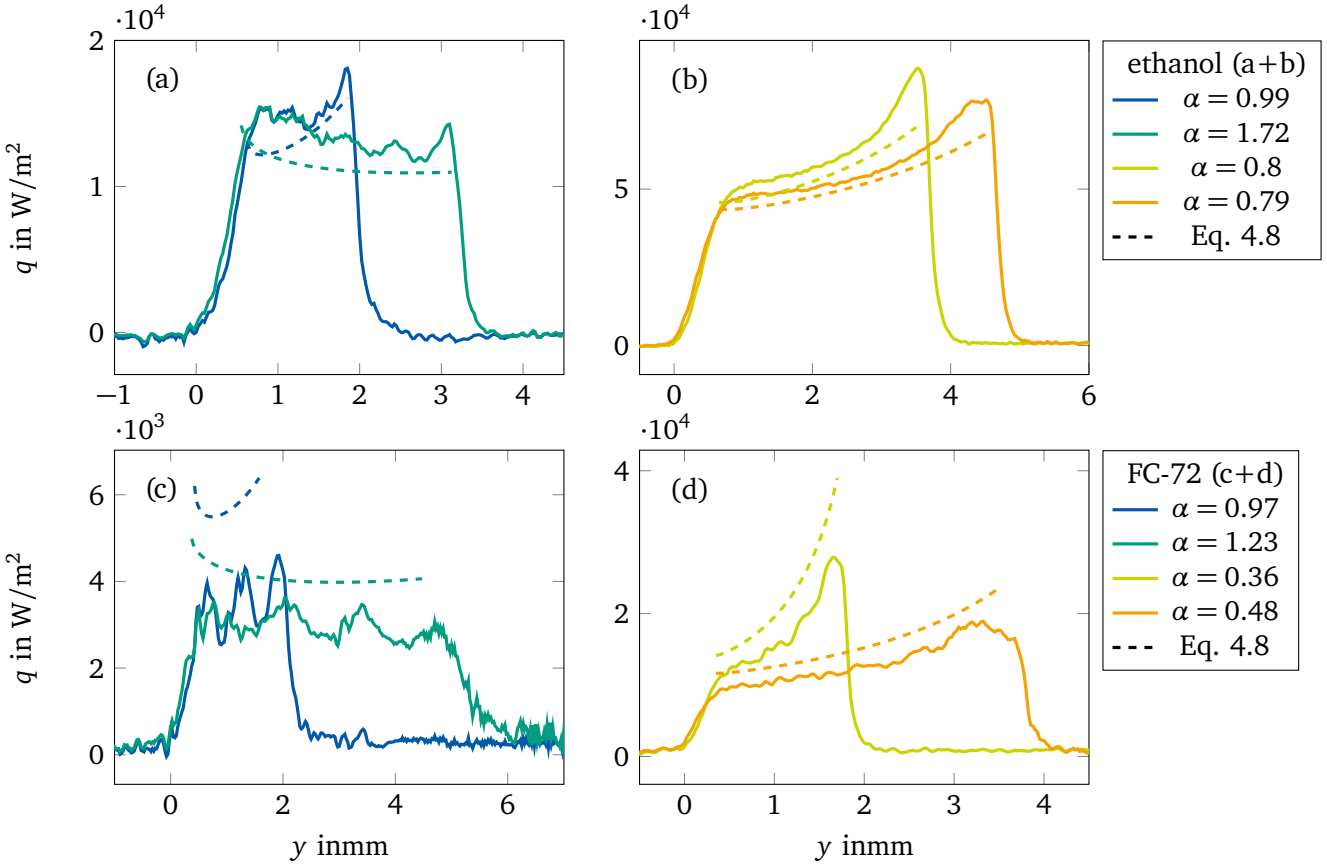

Figure 4.18: Comparison of the measured heat flux profiles (full lines) to Equation 4.8 (dashed lines). Top: ethanol at (a) $\overline{Ja} = (6.7 \pm 0.2) \times 10^{-3}$ and (b) $\overline{Ja} = (20.02 \pm 1.72) \times 10^{-3}$). Bottom: FC-72 at (c) $\overline{Ja} = (7.59 \pm 0.89) \times 10^{-3}$ and (d) $\overline{Ja} = (30.14 \pm 3.13) \times 10^{-3}$.

Ca, where neglecting heat transfer through the fluid is unlikely to cause large errors. In FC-72, on the other hand, α is below unity for most of the data. Hence, heat transfer in the liquid is the dominating mechanism determining heat flux in the microlayer region. However, for the highest Ca in FC-72, α remains above 0.25, which is still too large for heat transfer in the wall to be considered negligible.

Comparison of experiment and analytic expression

In Figure 4.18 the derived expression for $q(y)$, Equation 4.8, is compared with the median heat flux profiles obtained from the experiments. The experimental data q_{med} is shown with full lines, while Equation 4.8 is plotted with dashed lines. The data for ethanol is displayed in the top two graphs (a and b) and the data for FC-72 is displayed in the lower two graphs (c and d). The graphs on the left (a and c) correspond to low Ja, while the graphs on the right (b and d) correspond to high Ja. The coefficient α is displayed in the legend entry. It can be observed that Equation 4.8 does not perfectly agree with the numerical heat flux profiles. However, the overall shape of the numerical heat flux profiles is reproduced well by Equation 4.8. In ethanol, the analytical expression slightly underestimates q_{med}, while the opposite is observed in FC-72.

The source for the disagreement can be manifold but is likely due to measurement uncertainty in q, ΔT_0, and δ_0. As the shape is reproduced well, it can be concluded that Equation 4.8 is suitable to describe the heat flux in the microlayer region.

In Figure 4.18 it can be observed that the shape of the heat flux profile correlates with α. Profiles where q increases towards the contact line correspond to low values of α, while high values of α correlate with q decreasing towards the contact line. The gradient of the heat flux profile can be gained through differentiation of Equation 4.8:

$$\frac{\partial q}{\partial y} = -\frac{\Delta T}{(R_l + R_s)^2}\left(\frac{\partial R_l}{\partial y} + \frac{\partial R_s}{\partial y}\right). \tag{4.10}$$

It is eminent from Equation 4.10 that a decreasing heat flux profile can be expected when the combined gradient of both microlayer and thermal boundary layer increases towards the contact line. In order to deduce a more detailed condition, Equation 4.6 and Equation 4.7 are used to describe δ and γ, respectively. Differentiation with respect to y then yields

$$\frac{\partial}{\partial y}(R_l + R_s) = \frac{1}{y_{cl}}\left(b_\gamma \alpha \left(\frac{y}{y_{cl}}\right)^{b_\gamma - 1} - 1\right). \tag{4.11}$$

Hence, the gradient of the heat flux profile is negative, i.e decreases towards the contact line, if α exceeds a threshold value α_t:

$$\alpha_t = \frac{1}{b_\gamma}\left(\frac{y}{y_{cl}}\right)^{1-b_\gamma}. \tag{4.12}$$

Equation 4.12 shows a dependency on y: For constant $b_\gamma < 1$ and α, Equation 4.12 is much more likely fulfilled at small y, i.e. close to y_0, than close to the contact line, where the ratio y/y_{cl} approaches unity. This agrees well with the trend observed in Figure 4.12a, where the gradient of the heat flux profile changes from initially negative to positive closer to the contact line. The dependency on y, however, makes it difficult to quantify a single threshold value α_t, above which a single heat flux profile rather decreases towards the contact line. While the average gradient across the whole profile could be gained by integration of Equation 4.12, this quantity is not easily evaluated in the measurement data. In addition, the average gradient is distorted by the movement of the contact line peak. Therefore, Equation 4.12 is evaluated at a fixed location for comparison with the experiment. In the following, the middle of the profile $y/y_{cl} = 0.5$ is chosen for this purpose because it is easily located and unaffected by fluctuations near the contact line, unless the microlayer is very short.

For both ethanol and FC-72, a threshold value of $\alpha_t \approx 1.2 - 1.3$ can be observed in the experiments. In Equation 4.12, this corresponds to $b = 0.57 - 0.65$. In the experiments, however, a value of $b \approx 0.7$ is observed at α_t, which does not fully agree with Equation 4.12. Nevertheless, the values are quite

close. While Equation 4.12 might, therefore, not be suitable to obtain an exact value for α_t, it can be concluded that the overall magnitude of α is a good indicator for the expected shape of the heat flux profile. Furthermore, it should be noted, that extrapolating Equation 4.12 towards high Ca, where b_γ approaches unity, yields $\alpha_t = 1$.

4.3.2 Total heat flux between wall and fluid

The total heat flux in the steady state $Q_{tot} = Q_{ml} + Q_{men}$ is displayed in Figure 4.19 over the dewetting velocity u for different wall superheats $\overline{\Delta T}$. The results for ethanol are displayed in Figure 4.19a and the results for FC-72 in Figure 4.19b. For both fluids, the data follows the same trend and collapses onto two curves. For $\overline{\Delta T} = const.$, Q_{tot} remains low for low u, until a threshold in u is exceeded and Q_{tot} sharply increases. Thereafter, Q_{tot} continues to increase with u. The threshold value thereby corresponds to u_{cr}, at which a microlayer is formed. Therefore, all data below the dotted line correspond to the contact line evaporation regime, while all data above the dotted line correspond to the microlayer evaporation regime.

Total heat flux in the microlayer evaporation regime

The collapse of Q_{tot} onto a single curve in the microlayer evaporation regime is expected because evaporation is largely driven by the heat flux in the microlayer region Q_{ml}. In the steady state, the liquid mass $m_{ev} = Q_{ml}/\Delta h_v$ leaving the microlayer by evaporation must be equal to the mass flow m_{ml} entrained into the microlayer through the dynamic meniscus:

$$m_{ml} = u_l \delta_0 \rho_l, \tag{4.13}$$

where u_l is the mean velocity of the liquid in y-direction at y_0. Hence, Q_{ml} can be directly calculated if δ_0 and u_l are known. As above, it is assumed that $\delta_0 = \delta_{LLD}$ within the experiments presented in this work. The velocity profile within the film, however, is unknown. It is likely that u_l is equal to u close to the wall, but reduces as the liquid-vapor interface is approached due to gravitation. Consequently, the mean velocity of the liquid u_l is expected to be smaller than the dewetting velocity u of the wall. To describe the dependency between u_l and u in a simple manner, the coefficient $a_u = u_l/u$ is introduced. The integrated heat flux in the microlayer region Q_{ml} is then given by

$$Q_{ml} = a_u u \delta_0 \rho_l \Delta h_v \qquad \text{for} \quad u > u_{cr}. \tag{4.14}$$

Adding the integrated heat flux in the meniscus region Q_{men} to Equation 4.14 then results in an expression for the total heat flux Q_{tot} in the microlayer evaporation regime:

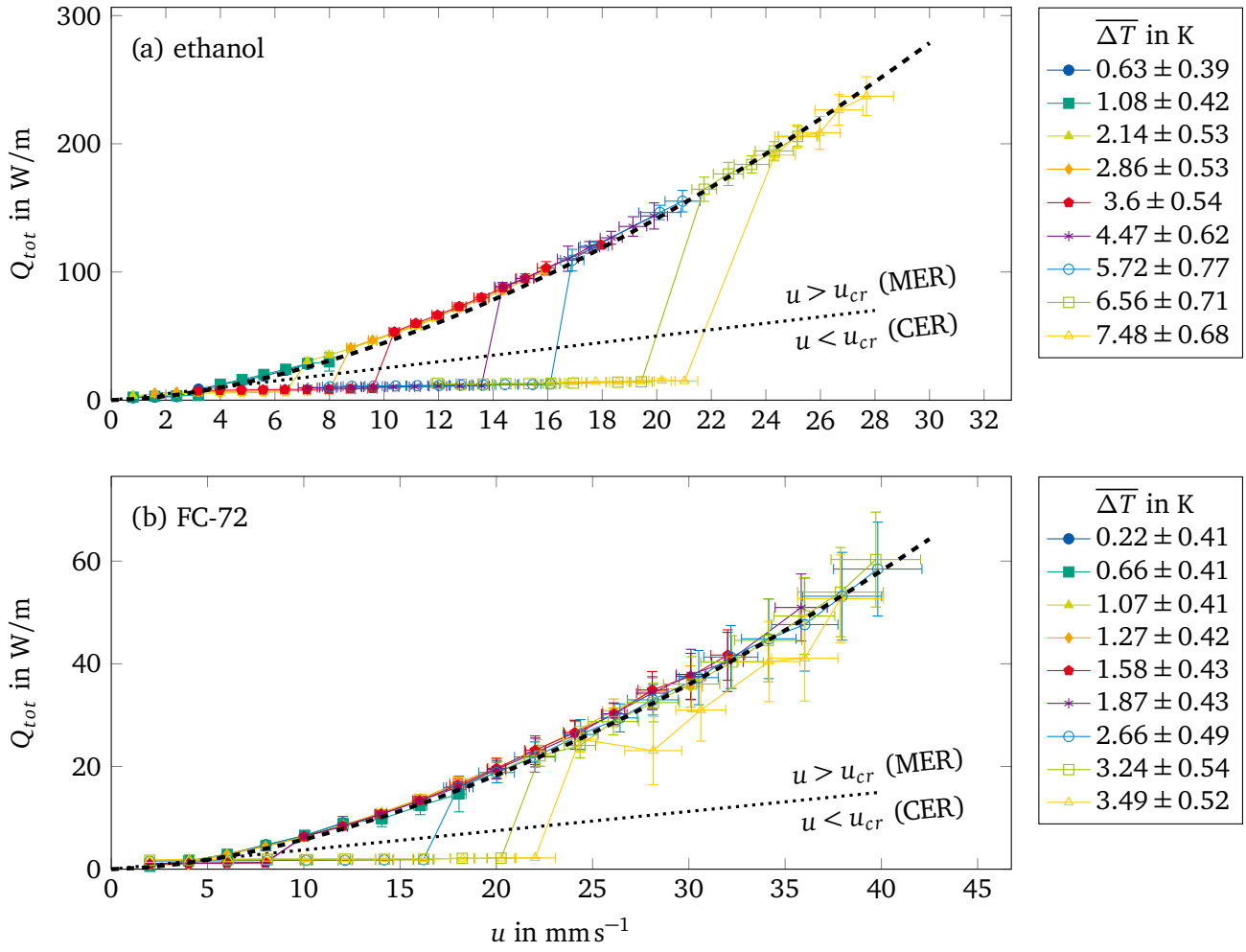

Figure 4.19: Total heat flux Q_{tot} over u for different ΔT for (a) ethanol and (b) FC-72. Experiments below the dotted straight line showed no microlayer formation. The dashed curve corresponds to Equation 4.15.

$$Q_{tot} = a_u u \delta_0 \rho_l \Delta h_v + Q_{men} \qquad \text{for} \quad u > u_{cr}. \tag{4.15}$$

A value for the coefficient a_u is obtained by fitting Equation 4.15 to the measurement data for Q_{tot} displayed in Figure 4.19. The fitting procedure yields $a_u^{eth} = 0.58$ and $a_u^{FC} = 0.65$ for ethanol and FC-72, respectively. The fitted function is indicated by the dashed line in Figure 4.19, showing excellent agreement with the measurement data in the microlayer evaporation regime. The obtained values for a_u indicate that a velocity profile within the microlayer at y_0 indeed exists, and that the velocity gradient towards the liquid-vapor interface is larger for ethanol. The values of the coefficients are very similar, however, and the difference might also be caused by the combined uncertainty in u and Q_{tot}. Nevertheless, assuming a linear velocity profile within the film, the obtained values for the coefficient a_u correspond to the velocity at the liquid-vapor interface being reduced to 16% and 30% of the dewetting velocity u for ethanol and

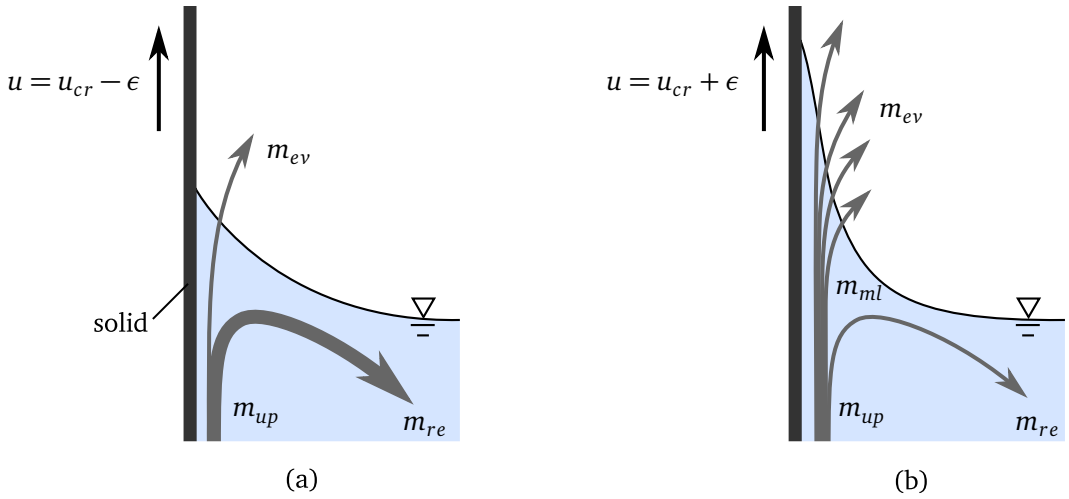

Figure 4.20: Illustration of the presumed flow field in the dynamic meniscus close to the regime boundary: (a) contact line evaporation regime ($u < u_{cr}$), (b) microlayer evaporation regime ($u > u_{cr}$).

FC-72, respectively.

While the above analysis shows that Q_{tot} is independent of ΔT in the microlayer evaporation regime, the change between both regimes, i.e. u_{cr}, is not. The shift in u_{cr} towards higher values with increasing ΔT, as discussed in section 4.2, is clearly visible in Figure 4.19. In addition, the gain in Q_{tot}, when changing from the contact line evaporation regime to the microlayer evaporation regime, i.e. surpassing u_{cr}, increases towards higher ΔT. Thus, a change in ΔT near u_{cr} can have dramatic effects on Q_{tot}. If the system is in the contact line evaporation regime, Q_{tot} can be significantly increased if ΔT is lowered sufficiently to cause a regime change into the microlayer evaporation regime. For example, decreasing ΔT from 7.48 K to 5.72 K for ethanol at a fixed dewetting velocity of 18 mm/s causes an increase in Q_{tot} of roughly 120 W/m. In the microlayer evaporation regime, on the other hand, the situation is reversed. Here, decreasing ΔT can cause a change into the contact line evaporation regime and hence a considerable decrease in Q_{tot}. Naturally, the same applies for a change in the dewetting velocity u in both evaporation regimes.

The increase in Q_{tot} at the regime boundary u_{cr} in the contact line evaporation regime suggests that the flow field within the dynamic meniscus changes at the regime boundary, which is illustrated in Figure 4.20. The contact line evaporation regime is shown in Figure 4.20a and the microlayer evaporation regime is shown in Figure 4.20b. Both situations depict the flow field just below and above the critical velocity u_{cr}, with ϵ being a positive infinitesimal. Hence, the dewetting velocity in both Figure 4.20a and b is very similar, and the mass flow m_{up} dragged upwards into the dynamic meniscus region by the motion of the wall can thus be assumed equal in both situations. In Figure 4.20a, some fraction m_{ev} of m_{up} is evaporated near the contact line. The evaporated mass flow m_{ev} must thereby be smaller than m_{up}, because otherwise Q_{tot}, which is limited by the mass entrained into the microlayer as discussed above, could not increase when crossing the regime boundary. Hence, the remaining fraction $m_{re} = m_{up} - m_{ev}$ is returned to the bulk liquid region, creating a vortex flow in the dynamic meniscus. This is supported by the numerical work of Kunkelmann [90], who reports a similar vortex flow in front of the contact line in the contact line

evaporation regime. In the microlayer evaporation regime, as shown in Figure 4.20b, m_{up} is essentially equal to m_{up} in Figure 4.20a. Thus, the sudden increase in heat flux seen in the experiments suggests a sudden reduction in the returned mass flow m_{re}, i.e. a weakening of the vortex flow inside the dynamic meniscus.

The analysis above shows that microlayer formation is not limited by the evaporation at the contact line, but is only driven by the evaporation near the contact line through the effects on the contact angle. Therefore, the change between the contact line evaporation regime and the microlayer evaporation regime is entirely due to fluid dynamics, as assumed earlier in section 4.2. However, one can imagine a situation where all mass evaporated at the contact line is equal to m_{up}. If the "fluiddynamical" u_{cr} according to section 4.2 was very low, a larger "evaporative" u_{cr} could then instead be observed, whose value was not determined by the contact angle, but only the raw magnitude of evaporation in the contact line region. Consequently, no sudden increase in Q_{tot} would be observed at the regime boundary. In Figure 4.19, this situation could be expected where the upper and lower curves meet, i.e. for very low u and ΔT. However, the measurement data presented in this work allow no further comment on this specific subject due to the measurement uncertainty at very low ΔT.

Total heat flux in the contact line evaporation regime

From Figure 4.19, one might expect a linear dependency of the total heat flux Q_{tot} on the dewetting velocity u in the contact line evaporation regime (for $u < u_{cr}$). However, the small increase of Q_{tot} for $u < u_{cr}$ with u, is largely due to the increase in ΔT towards higher u. This is displayed in more detail in Figure 4.21, where Q_{tot} is plotted over Ja for only $u < u_{cr}$ for both ethanol and FC-72. Q_{tot} increases significantly with Ja. A clear dependency of Q_{tot} on u in the contact line evaporation regime is not observed. Otherwise, the data displayed in Figure 4.22 would experience larger scatter due to the present variation of u. This indicates that convective effects, such as micro convection in the dynamic meniscus region, are subordinate and Q_{tot} is dominated by evaporation. However, the data for both fluids does not collapse onto the same curve, but much larger Q_{tot} are observed for ethanol at the same Ja. Naturally, Δh_v and $c_{p,l}$ of both fluids differ greatly, but this is already considered in Ja. This suggests that further fluid properties or additional effects are relevant for the heat flux in the contact line evaporation regime. For example, λ_l is about twice as large for ethanol and conductive heat flux between wall and liquid-vapor interface is, therefore, increased.

While the relationship between Q_{tot} and Ja looks fairly linear, a best fit using a first degree polynomial is only obtained when assuming $Q_{tot}(\mathrm{Ja} = 0) > 0$, which is not physical. For ethanol, this is similar to the non-zero cross seen for Ca_{cr} (Figure 4.7a) and can be resolved by assuming a systematic measurement error in ΔT in the order of 0.5 K as well. In FC-72, however, the trend of the data itself suggests a non-linear dependency. Therefore, a power law is used to fit the data for both fluids, which is also suggested by Kunkelmann [90] and Janecek and Nikolayev [74] to describe the heat flux in the micro region. The obtained correlations are indicated in Figure 4.21 and are given by Equation 4.16 and Equation 4.17

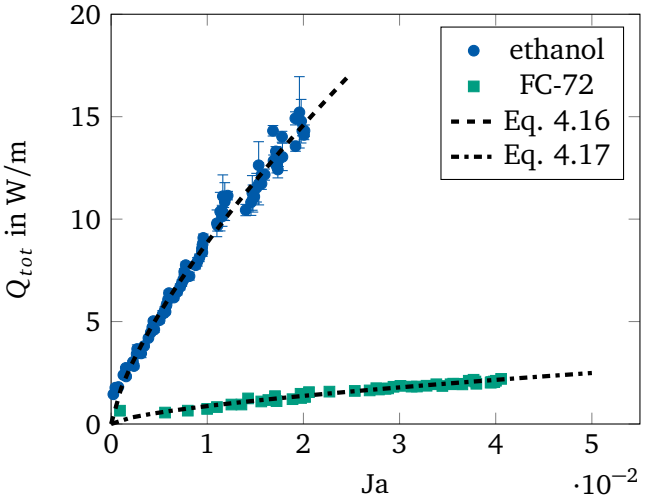

Figure 4.21: Total heat flux Q_{tot} in the contact line evaporation regime ($u < u_{cr}$) over Ja for ethanol and FC-72.

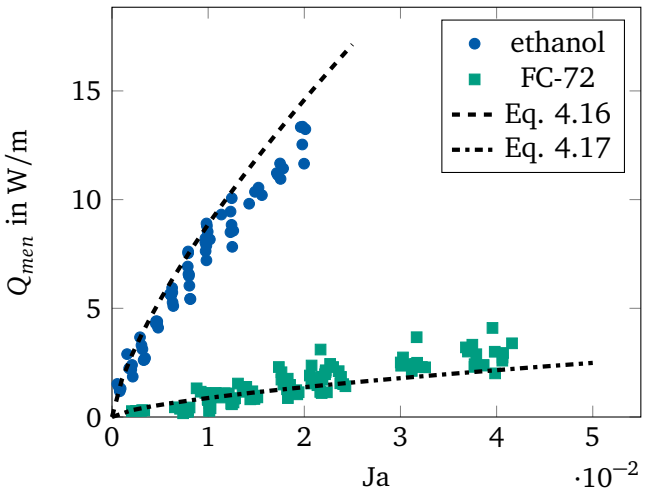

Figure 4.22: Comparison of Q_{men} in the microlayer evaporation regime ($u > u_{cr}$) to Q_{tot} in the contact line evaporation regime $u < u_{cr}$ with $e_{Q_{med}} \approx \pm 2.5\,\mathrm{W/m}$.

for ethanol and FC-72, respectively. It can be noted that the expressions for both fluids share a similar exponent.

$$Q_{tot}^{eth} = (244 \pm 29.5)\ \mathrm{Ja}^{(0.72\pm0.028)}\ \ \mathrm{W/m} \qquad \text{for} \quad u < u_{cr} \tag{4.16}$$

$$Q_{tot}^{FC} = (17.46 \pm 2.8)\ \mathrm{Ja}^{(0.65\pm0.043)}\ \ \mathrm{W/m} \qquad \text{for} \quad u < u_{cr} \tag{4.17}$$

As has been shown earlier, the dynamic meniscus region in front of the microlayer contributes to the total heat flux in the microlayer evaporation regime. Therefore, it must be assumed that this is also the case in the contact line evaporation regime, where Q_{tot} must hence be expressed as the sum of Q_{men} and the contribution of the apparent contact line Q_{cl}, i.e. the evaporation in the micro region according to the micro region model. Obviously, the latter cannot be measured directly because the size of the micro region is almost two orders of magnitude smaller than the pixel resolution of the infrared camera. When only considering the contact line evaporation regime, where the heat flux profile resembles a simple peak, it is, therefore, impossible to separate the contribution of the micro region from the contribution of the dynamic meniscus. However, it can be assumed that Q_{men} is of similar magnitude in both evaporation regimes. After all, close to Ca_{cr} the apparent contact angle is also small in the contact line evaporation regime, and the shape of the dynamic meniscus in front of the contact line is hence comparable to the shape of the dynamic meniscus in front of a microlayer. Furthermore, Q_{tot} in the contact line evaporation regime has been shown to be practically independent of u. Thus, the velocity difference between contact line evaporation regime and microlayer evaporation regime on Q_{men} can be assumed negligible. Consequently,

the difference between Q_{tot} in the contact line evaporation regime and Q_{men} in the microlayer evaporation regime offers an opportunity to estimate Q_{cl}, the contribution of the evaporation directly at the apparent contact line.

Q_{men} for $u > u_{cr}$ is displayed in Figure 4.22. The lines mark Equation 4.16 and Equation 4.17, i.e. the correlation for Q_{tot} for $u < u_{cr}$. The measurement data is rather scattered and measurement uncertainty given in the figure description is comparatively high, which is primarily due to the difficult estimation of y_0 in combination with the rather small size of the dynamic meniscus region. However, the data for Q_{men} follows Q_{tot} in the contact line evaporation regime rather well in both trend and magnitude. Especially good agreement is found for ethanol, where the dynamic meniscus region is more prominent due to the larger l_c. Here, Q_{men} seems to remain slightly below the correlation obtained for Q_{tot}. Unfortunately, the measurement uncertainty and scatter of the data does not allow a direct estimation for Q_{cl}. Nonetheless, the agreement in both trend and magnitude indicate that heat flux in the contact line evaporation regime is largely driven by the evaporative heat flux in the dynamic meniscus region in front of the contact line.

4.3.3 Local heat flux at the contact line

As shown above, heat flux at the contact line cannot be assessed using integrated quantities due to the evaporation in the dynamic meniscus region. Therefore, only the peak in heat flux at the contact line, q_{cl}, is analyzed in the following. q_{cl} is displayed in Figure 4.23, where the data for ethanol is shown in Figure 4.23a and the data for FC-72 is shown in Figure 4.23b. q_{cl} describes the average magnitude of the peak in heat flux at the contact line during the steady state and is plotted for different ΔT over $u - u_{cr}$. Thus, negative values of $u - u_{cr}$ indicate the contact line evaporation regime and positive values correspond to the microlayer evaporation regime. For $u < u_{cr}$, u has little effect on q_{cl} for both ethanol and FC-72. For $u - u_{cr} = const.$, however, q_{cl} increases with increasing ΔT. These two observations are in agreement with previous work concerning the heat flux at the contact line, for example the numerical work by Batzdorf [5] or the experiments by Kunkelmann et al. [93].

When changing from the contact line evaporation regime into the microlayer evaporation regime at $u = u_{cr}$, the observations for ethanol and FC-72 differ greatly. For FC-72, heat flux at the contact line sharply increases. The magnitude of this increase rises with ΔT and exceeds relative gains of 100%. For $u > u_{cr}$, q_{cl} then slowly decreases with u at low ΔT, while remaining rather constant at higher ΔT. For ethanol, on the other hand, q_{cl} decreases when changing from the contact line evaporation regime into the microlayer evaporation regime. The magnitude of the decrease thereby increases with ΔT. Nevertheless, it should be noted that the change in q_{cl} relative to the overall magnitude is much smaller for ethanol than for FC-72. For $u > u_{cr}$, the dependency of q_{cl} on u for ethanol then mirrors the trend for FC-72. According to the micro region model presented in section 2.1, heat flux at the contact line is, apart from fluid properties, largely dependent on the superheat at the contact line ΔT_{cl} and the contact angle θ_{ev}. Therefore, these two quantities are further explored in the following. However, as mentioned before, the size of the micro

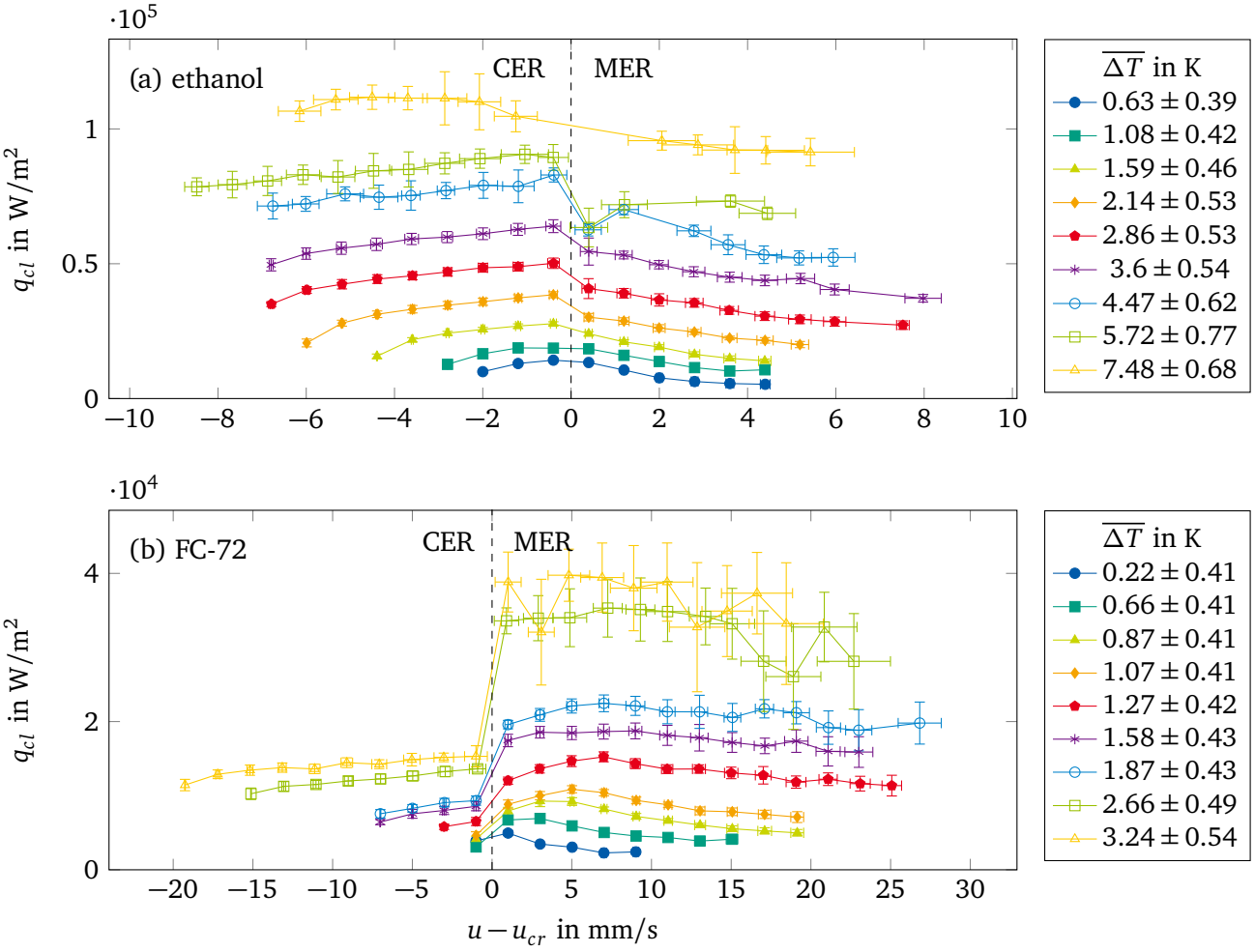

Figure 4.23: Steady state heat flux at the contact line q_{cl} over $u-u_{cr}$ for different ΔT for (a) ethanol and (b) FC-72. Positive and negative values on the abscissa correspond to the microlayer evaporation regime and contact line evaporation regime, respectively.

region is much smaller than one pixel of the infrared camera, which is the length scale corresponding to q_{cl}. Therefore, the comparison remains of qualitative nature.

Superheat at the contact line

The superheat at the contact line ΔT_{cl} is displayed relative to the wall superheat ΔT over the dewetting velocity u in Figure 4.24. The results obtained with ethanol are shown in Figure 4.24a and those obtained with FC-72 are shown in Figure 4.24b. The dotted line indicates the evaporation regimes, with all experiments above the dotted line corresponding to $u < u_{cr}$. For both fluids, ΔT_{cl} decreases when changing into the microlayer regime. In addition, the total magnitude of this decrease (in kelvin) increases towards higher ΔT. Please note that this is not directly obvious from Figure 4.24, because ΔT_{cl} is displayed relative

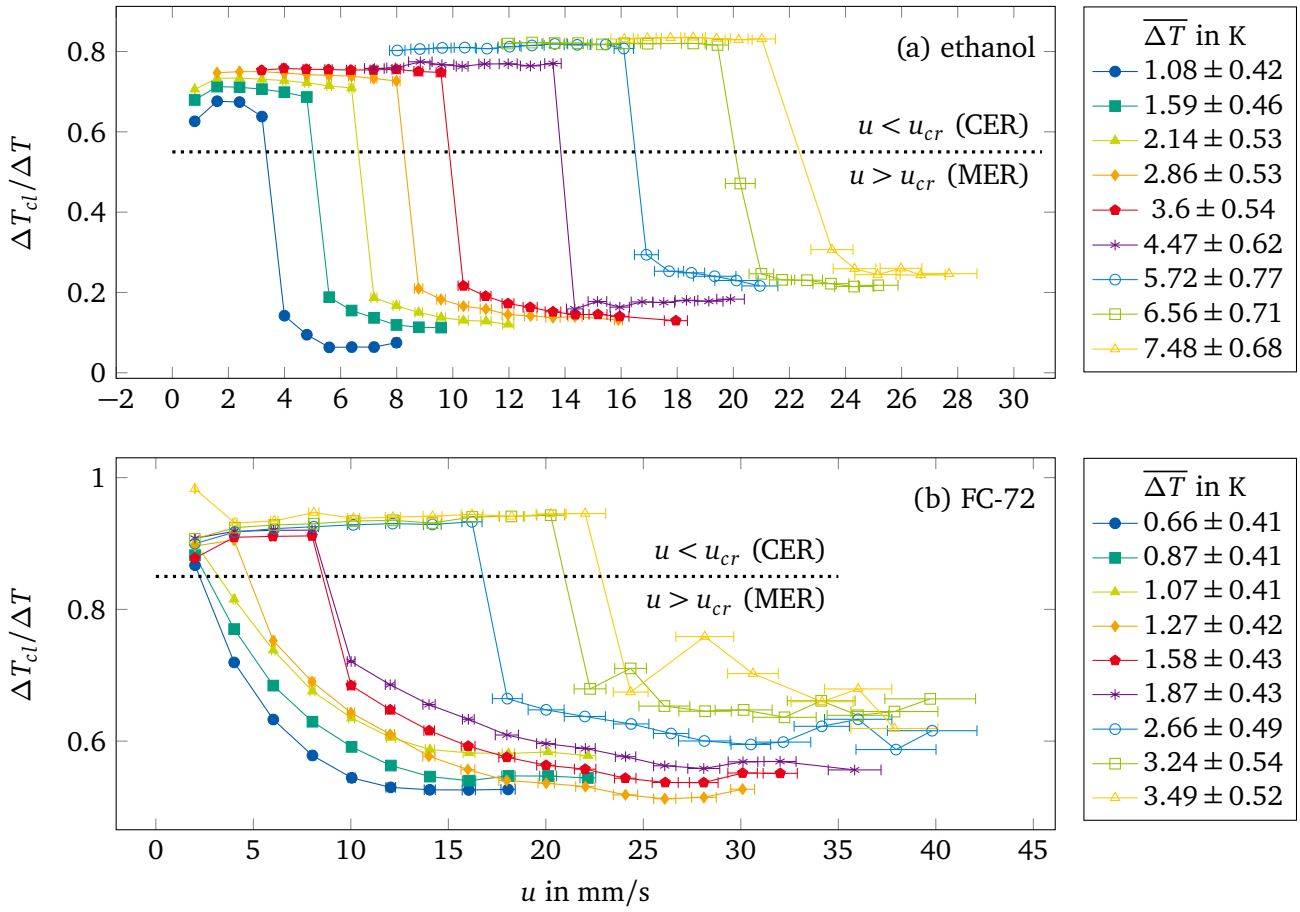

Figure 4.24: Wall superheat at the contact line ΔT_{cl} relative to the wall superheat in the bulk region ΔT during the steady state over u for different ΔT for (a) ethanol and (b) FC-72. No microlayer formation was observed for all experiments above the dotted line ($u < u_{cr}$).

to ΔT. However, it is immediately eminent that the trend for ΔT_{cl} cannot explain the increase in q_{cl} at $u = u_{cr}$ seen for FC-72. On the contrary, the effect responsible for the increase must be strong enough to counteract the reduction in ΔT_{cl}. For ethanol, on the other hand, the decrease in q_{cl} does agree with the trend observed for ΔT_{cl}. However, the relative decreases seen in ΔT_{cl} are much larger than the relative decreases seen in q_{cl}: For example, for $\overline{\Delta T} = 4.54\,\mathrm{K}$, ΔT_{cl} decreases from 3.5 K to 0.85 K at u_{cr}, which is a decrease of 75%. q_{cl}, on the other hand, decreases from $80\,\mathrm{kW/m^2}$ to $52\,\mathrm{kW/m^2}$, which is a decrease of only 35%. Similar to FC-72, some additional effect must exist, which increases q_{cl} and counteracts the detrimental effects of the reduced temperature at the contact line.

In addition to the above, the trend of $\Delta T_{cl}/\Delta T$ is noteworthy in itself. For $u < u_{cr}$, $\Delta T_{cl}/\Delta T$ is independent of u and very similar for each $\overline{\Delta T}$, for which a slight dependency can be seen for ethanol. For $u > u_{cr}$, $\Delta T_{cl}/\Delta T$ then decreases with u due to the formation of a microlayer, which cools the wall before the wall reaches the contact line. The data of FC-72 for the lowest $\overline{\Delta T} = const.$ neatly shows that this cooling effect then gradually increases with the length of the microlayer, which increases with u. Towards higher $\overline{\Delta T}$, a

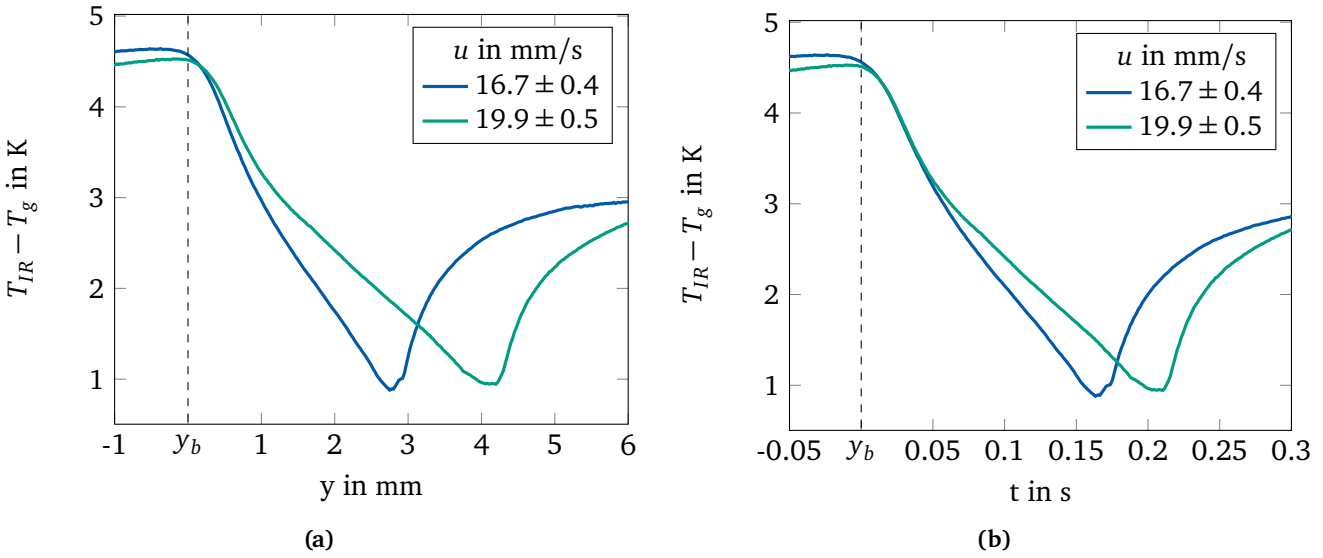

Figure 4.25: Local superheat $T_{IR} - T_g$ at the solid-liquid interface for ethanol, two different u, and similar $\Delta T \approx 4.5\,\mathrm{K}$. (a) Fixed reference frame. (b) Moving reference frame.

jump in $\Delta T_{cl}/\Delta T$ then appears, which is explained by the minimum microlayer length h_{min} increasing with ΔT (compare Figure 4.26). As h_{min} increases with ΔT, so does this cooling effect in front of the contact line and hence the magnitude of the drop in $\Delta T_{cl}/\Delta T$ at $u = u_{cr}$. However, one would then expect a further decrease in $\Delta T_{cl}/\Delta T$ with u because h increases with u for $u > u_{cr}$. As seen in Figure 4.24, this is not the case. Instead, $\Delta T_{cl}/\Delta T$ approaches some lower limit and shows very little dependency on u towards higher ΔT for FC-72 and all data for ethanol. The question arises, why $\Delta T_{cl}/\Delta T$ does not approach the obvious limit of zero with increasing u. After all, as long as ΔT_{cl} is finite, energy remains in the wall at the solid-liquid interface, which could be used to evaporate the microlayer. That this situation does not occur in the experiments, however, is illustrated in Figure 4.25.

In Figure 4.25a, the local wall superheat $T_{IR} - T_{sat}$ is plotted over y for two different dewetting velocities u. The dashed line indicates the end of the bulk liquid region $y_b = 0$. For both graphs, the location of the contact line coincides with the minimum in $T_{IR} - T_{sat}$. It can be observed that the gradient of the local wall superheat in y-direction reduces with the dewetting velocity u in such a way that the same superheat at the contact line ΔT_{cl} is reached in both experiments, even though the microlayer length h differs. In Figure 4.25a, however, the effects of wall movement and evaporation on the shape of the profiles are superimposed due to the stationary reference frame of the infrared camera. The effects of evaporation are isolated by using a Lagrangian reference frame, which is achieved by scaling the y-coordinate by u.

The resulting profiles are shown in Figure 4.25b. The time $t = y/u$ thereby describes the duration a wall-element traveling with the velocity u has spent above y_b. Both profiles now collapse neatly for low t, which corresponds to equal cooling within the dynamic meniscus region. The two profiles then start to deviate at approximately $t = 0.04\,\mathrm{s}$, which corresponds to the point in time, where the wall element passes y_0 and the microlayer region is entered. $T_{IR} - T_{sat}$ then reduces faster at the lower dewetting velocity u.

This is logical because the initial microlayer thickness δ_0 increases with u, leading to increased thermal resistance of the microlayer. Consequently, local heat flux is slightly elevated for low u (at $\Delta T = const.$) and the initial fluid mass deposited at y_0 is evaporated faster. As the initial microlayer thickness δ_0 is increased, $T_{IR} - T_{sat}$ stunningly adjusts in just the right way that ΔT_{cl} remains constant. As previously seen in Figure 4.24, this behavior is observed for all levels of wall superheat ΔT and the overall magnitude of the minimum ΔT_{cl} (in kelvin) rises with the wall superheat ΔT. For example, for $\overline{\Delta T} = 6.56\,\mathrm{K}$, ΔT_{cl} reaches approximately $0.23 \times 6.56\,\mathrm{K} \approx 1.51\,\mathrm{K}$. This suggests that evaporative heat flux, heat conduction in the liquid, and heat conduction within the wall might be coupled in some fundamental way. This is further supported by the fact that the limit in $\Delta T_{cl}/\Delta T$ is very similar for each $\overline{\Delta T}$. Similarities can be drawn to the solution of the heat equation for two semi-infinite bodies of different temperature, which reach a defined interface temperature when brought into contact.

Effects of contact angle

As ΔT_{cl} cannot explain the increase in q_{cl} for FC-72, the contact angle is considered in the following. As pointed out in section 2.1, q_{cl} increases with reducing θ_{ev} because the film thickness in the micro region decreases. Within the context of the experimental resolution, a decrease in contact angle corresponds to a reduction of mean film thickness across the pixel closest to the contact line. Indeed, θ_{ev} decreases with u and reaches a minimum at u_{cr}, as discussed in section 4.2, and the weak dependency of q_{cl} on u for $u < u_{cr}$ might well be explained by this effect. However, the reduction in θ_{ev} with u according to the micro region model is continuous, which does not agree with the sudden increase of q_{cl} seen for FC-72 at the regime boundary. One could propose a very rapid decrease in θ_{ev} as u_{cr} is approached, for which, however, no supporting literature is known to the author. Furthermore, once a microlayer is formed, the contact line is carried upwards with the moving wall and the relative velocity between contact line and wall reduces. Therefore, θ_{ev} at the end of a microlayer is very likely similar to the static evaporative contact angle and thus larger than θ_{ev} in the contact line evaporation regime. In the framework of the micro region model, this situation would lead to q_{cl} slowly increasing with u towards the regime boundary, where a maximum is reached. For $u > u_{cr}$, q_{cl} would then decrease. The described trend is, in fact, very similar to q_{cl} for ethanol. For FC-72, however, the described trend strongly contradicts the experimental data presented here.

As mentioned above, the expected behavior according to the micro region model is the trend seen for ethanol, i.e. rather little change of q_{cl}. For $\alpha < \alpha_t$, where the local heat flux rises towards the contact line, q_{cl} for $u < u_{cr}$ is thus expected to be larger than the heat flux at the beginning of the microlayer region (close to y_0) for $u > u_{cr}$. For FC-72, however, q_{cl} for $u < u_{cr}$ is about equal to the heat flux at y_0. The reader is referred to Figure 4.11 in section 4.3.1 for a visual impression. Therefore, the question is not so much why q_{cl} for FC-72 increases at u_{cr}, but rather why q_{cl} is unexpectedly low for $u < u_{cr}$. Consequently, any effect that explains the sudden increase in q_{cl}, such as the appearance of a precursor-like foot at the contact line observed by Qu et al. [118], must be absent for ethanol. The same holds for explanations tied to experimental limitations, which should have an equal effect on the observations made

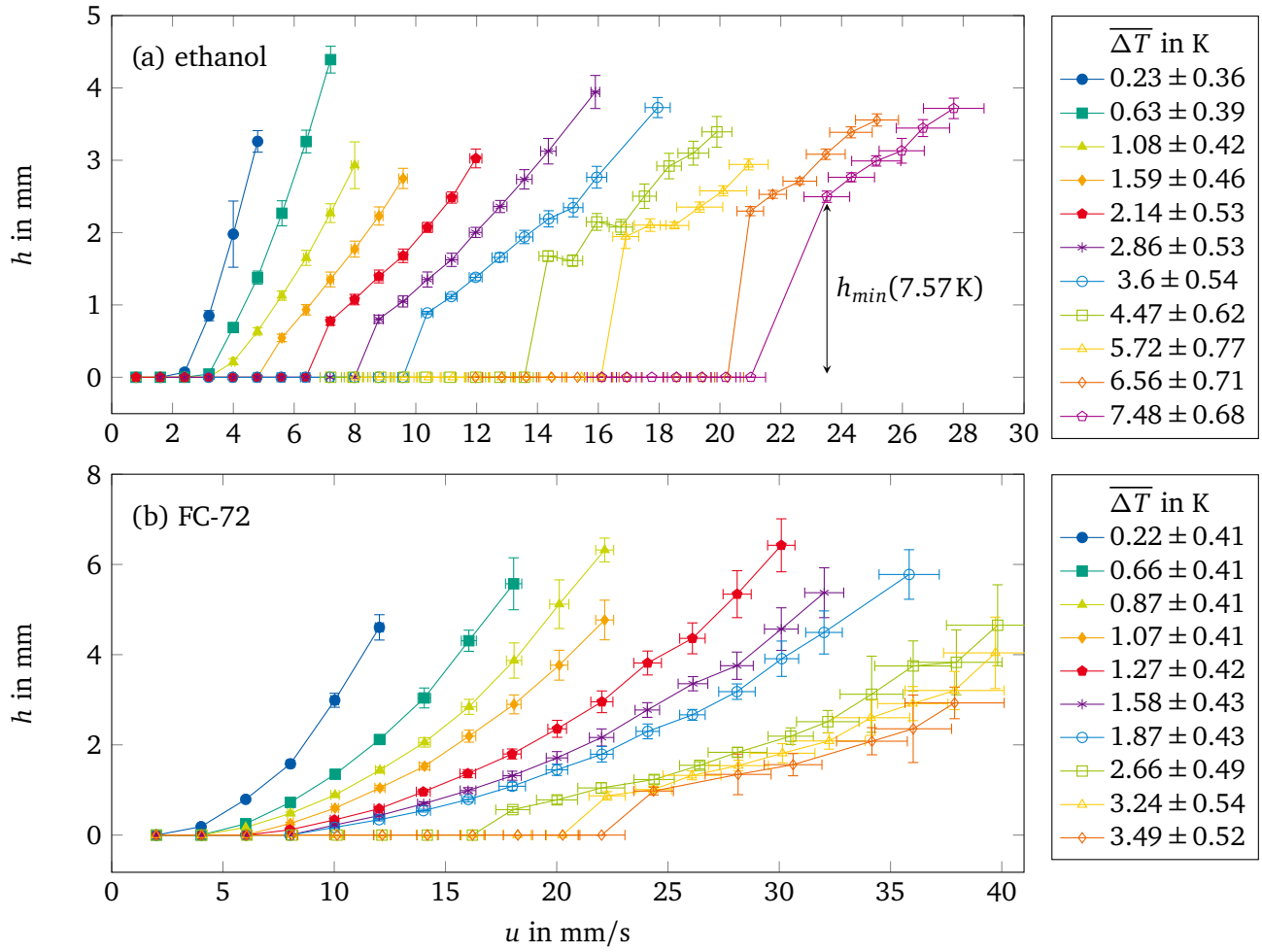

Figure 4.26: Measured steady state film length h for different dewetting velocities u and wall superheats $\overline{\Delta T}$ for (a) ethanol and (b) FC-72.

for ethanol and FC-72. As it has been shown that the interaction between solid and liquid is of importance to the length of the microlayer, it can be suggested that this might also be the case for q_{cl}. However, a satisfying explanation for the increase in heat flux at u_{cr} seen for FC-72 cannot be given by the author. The phenomenon should be studied in more detail, possibly in combination with numerical simulations, to develop a better understanding of the heat transfer at the contact line at the dewetting transition on a scale not accessible by experiment.

4.4 Microlayer length

The measured steady state microlayer length h is shown in Figure 4.26, where the results obtained with ethanol are shown in the top graph Figure 4.26a and the results obtained with FC-72 are shown in the lower graph Figure 4.26b. In both graphs h is plotted over the dewetting velocity u for different levels

of wall superheat $\overline{\Delta T}$. From the discussion above, it is clear that u_{cr} needs to be surpassed in order for a microlayer to form and $h = 0$, therefore, corresponds to $u < u_{cr}$. Above u_{cr} the microlayer length does not begin to grow from zero but from a minimal length h_{min}. This feature is most prominent for ethanol in Figure 4.26a but can also be observed for FC-72 in Figure 4.26b. However, h_{min} is generally larger for ethanol than for FC-72. For both fluids, the value of h_{min} increases with u_{cr}, i.e. with $\overline{\Delta T}$. As u is increased above u_{cr}, h increases further and the magnitude of this increase with u is larger for small $\overline{\Delta T}$. Thus, at large $\overline{\Delta T}$ a larger dewetting velocity u is needed to produce the same microlayer length h.

Analytical description of the steady state microlayer length

To deduce a description for the microlayer length h, only data points above the critical velocity u_{cr} are taken into account. As previously mentioned, an underlying relationship can be expected because h describes the particular length of the microlayer, at which the total mass lost by evaporation m_{ev} equals the mass replenished by the wall movement. The reader is again referred to Figure 4.13 for an illustration of all quantities discussed in the following. From the calculation of the integrated heat flux in the microlayer region Q_{ml}, the replenishing mass flow m_{ml} entering the bottom of the microlayer through the dynamic meniscus is described by Equation 4.13. Similarly, the mass flow m_{ev} lost by evaporation is obtained by integrating the heat flux caused by evaporation across the whole microlayer region:

$$m_e = \frac{1}{\Delta h_v} \int_{y_0}^{y_{cl}} q(y) dy. \tag{4.18}$$

Equation 4.18 is combined with Equation 4.8, the expression for the local heat flux q derived in section 4.3.1. The resulting expression can be integrated without further treatment of the contact line region because the inclusion of the thermal boundary layer in the wall resolves the heat flux singularity at the contact line. Unfortunately, a general solution for the integral does not exist. However, solutions exists for certain values of the exponent b_γ with the simplest case being $b_\gamma = 1$. Following this assumption, an expression for h is obtained through $m_{ev} = m_{ml}$:

$$h = a_u u \delta_0^2 \frac{\rho_l \Delta h_v}{\lambda_l \Delta T_0} (\alpha - 1) \ln(\alpha)^{-1}. \tag{4.19}$$

Equation 4.19 is indeterminate at $\alpha = 1$. However, the following limit is approached at $\alpha = 1$:

$$\lim_{\alpha \to 1} \frac{\alpha - 1}{\ln(\alpha)} = 1. \tag{4.20}$$

A graphical representation of this limit can be found in the appendix Figure A.2. With the data available for α, Equation 4.19 can be directly tested against the measured h. Again, Equation 2.17 is used for the description of δ_0 for ethanol and FC-72. a_u in Equation 4.19 is expected to equal a_u obtained from

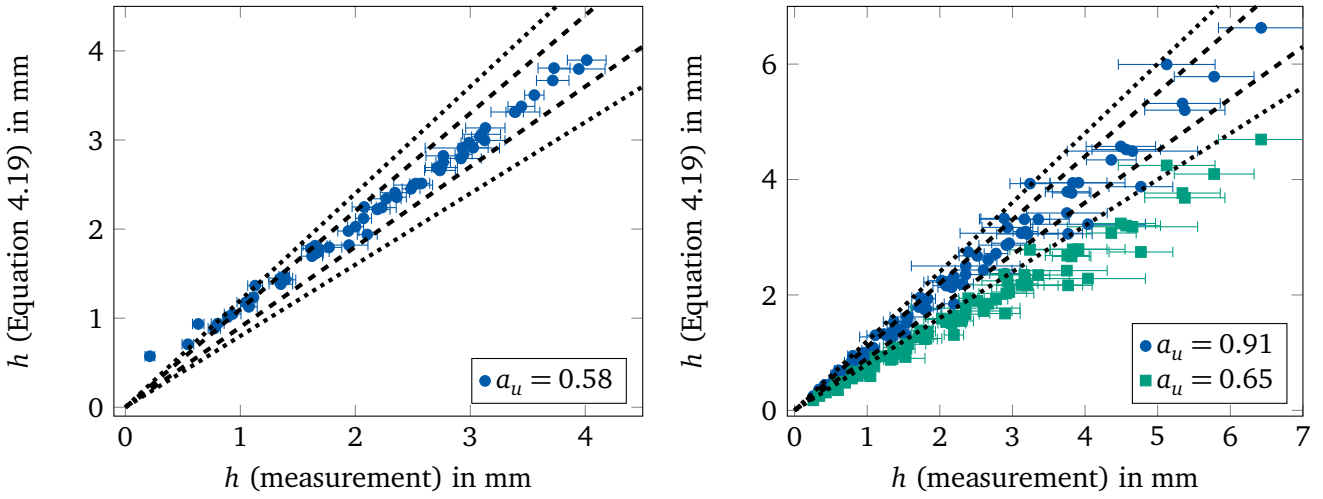

(a) ethanol

(b) FC-72

Figure 4.27: Comparison of h obtained with measurement and calculation, Equation 4.19, for (a) ethanol and (b) FC-72. The dashed and dotted lines indicate an error of ±10% and ±20%, respectively.

the analysis of Q_{ml} in section 4.3.2. In order to test this assumption, a_u is recalculated by fitting all measurement data at $\Delta T \geq 1\,\mathrm{K}$ to Equation 4.19. Measurements at $\Delta T \leq 1\,\mathrm{K}$ were found to not agree well with Equation 4.19, likely due the larger importance of measurement uncertainty in T_{IR} on T_0 and γ_0, and are, thus, disregarded.

The comparison of Equation 4.19 with the measurement data is shown in Figure 4.27. h calculated with Equation 4.19 is shown on the ordinate and the h inferred from the measurements is shown on the abscissa. For ethanol, which is displayed in Figure 4.27a, good agreement is found for $a_u^{eth} = 0.58$, which equals a_u obtained in section 4.3.2. Largest disagreement can be seen for very low h, where the microlayer length is overestimated by Equation 4.19. This is accounted to the uncertainty in y_0, whose magnitude relative to h becomes larger as h decreases. Furthermore, short h are observed for low Ca, for which the assumption of $b_\gamma = 1$ agrees with the least. Lastly, heat conduction in y-direction, which is assumed negligible, is likely more important for very short microlayers compared to long microlayers.

For FC-72, which is displayed in Figure 4.27b, however, best agreement is found for $a_u^{FC} = 0.91$, which exceeds the previously found value of $a_u = 0.65$ significantly. Consequentially, h is underestimated by Equation 4.19 for the latter value. The reason for the disagreement of a_u between the two presented methods of evaluation cannot be entirely identified. It can be argued that a_u for both fluids should be of similar magnitude due to the comparability of u, δ_0, and ρ_l in the experiments. This then indicates that $a_u^{FC} = 0.91$ obtained from h is likely wrong, and $a_u^{FC} = 0.65$ obtained from Q_{ml} likely correct. Consequentially, the error must lie within ΔT_0 or α, which are not used for the assessment of a_u in section 4.3.2. A measurement error can be assumed due to the uncertainty in y_0, the small size of the dynamic meniscus region for FC-72, and the overall lower wall superheat ΔT than for ethanol.

Nevertheless, it can be concluded that Equation 4.19 describes the measurements well. Best agreement is

found for ethanol, where 90% and 80% of the data show a deviation below ±14% and ±9.5%, respectively. For FC-72 and $a_u = 0.91$, 90% and 80% of the data is described within ±17.2% and ±12.4% deviation, respectively. It should be noted, however, that the measurement uncertainty is also greater for FC-72 due to the increased u and fluctuations.

While it was shown that Equation 4.19 can describe the length of a microlayer, it cannot be used for prediction, unless γ_{cl} and ΔT_0 are known. Analytical descriptions or correlations for $\gamma_{cl,0}$ and ΔT_0, however, are not known to the author. Attempts at finding models for γ_{cl} through fitting did not yield satisfying results because at least three fluid-dependent fitting parameters are required to describe the presented data accurately. However, the problem is simplified significantly at high ΔT, where γ_{cl} converges to a constant value. Furthermore, ΔT_0 approaches the global wall superheat ΔT if the influence of the dynamic meniscus becomes smaller. This can be expected for fluids with a low capillary length l_c. Indeed, Equation 4.19 delivers very similar results for FC-72 when using $\gamma_{95\%}$ and ΔT instead. In addition, γ_{cl} is not directly accessible through experiment. Equation 4.19 could, therefore, offer a way to estimate the thermal boundary layer through measurement of h. Lastly, the analytical analysis of q and h above is one-dimensional, as heat transfer in y-direction along the microlayer is neglected. Therefore, satisfactory results could likely be obtained from a simple one-dimensional numerical model, where the evaporation of some initial liquid thickness δ_0 is coupled with thermal conduction in the solid (z-direction only) and solved in time. The length of the microlayer, or the shape of the local heat flux, could be gained from the conversion $y = t/u$ used above.

Lastly, it is pointed out that the microlayer lengths h measured in this work do not agree with those reported by Fischer [35], where h is roughly one order of magnitude shorter for the same dewetting velocity u, wall superheat ΔT and fluid (FC-72). Hence, the expression for the microlayer length h presented by Fischer [35] does not suit the experiments reported in this work, but underestimates h by roughly one order of magnitude. While the reason for this disagreement remains largely unclear to the author, the input heat flux during the dewetting procedure is zero in this work, but non-zero in the experiments carried out by Fischer [35]. Furthermore, in the model used by Fischer [35] to derive an expression for h, the temperature of the solid substrate is assumed constant. These two differences may explain why the microlayers reported by Fischer [35] are much shorter but yet agree with his derived analytical expression.

4.5 Implications for boiling heat transfer

In the following paragraphs the research presented in this work is related to nucleate boiling and some general implications are discussed. For this purpose, it is assumed that microlayer formation underneath a growing vapor bubble is indeed a dynamic wetting transition and hence comparable to the experiments in this work.

4.5.1 Dynamic wetting transition in nucleate boiling

As outlined in section 2.2, the heat transfer mechanisms underneath a growing vapor bubble and their relative importance have been highly debated, because evidence in favor of both contact line evaporation and microlayer evaporation exists. Interpreting this debate in the context of the dynamic wetting transition, it is worth examining the experimental conditions under which contact line evaporation or microlayer evaporation have been studied in the published research. Most strikingly, the majority of observations of contact line evaporation in nucleate boiling have been made with refrigerants as working fluids and within micro gravity conditions, for example [37, 111, 150, 132, 160]. In contrast, studies observing a microlayer employ largely water and ethanol as working fluids and are performed within normal gravitational conditions, for example [15, 16, 80, 152, 153, 154]. The possible influence of these differences on the observed evaporation regime is explored in the following.

It should be stressed that the velocity, which determines regime transition in nucleate boiling, is the velocity of the dynamic meniscus region relative to the wall, i.e. the velocity of the region where the bubble is attached to the wall on a macroscopic length scale. Experimentally, this velocity is difficult to obtain. If at all, bubble growth is thus often characterized by the bubble growth rate determined from the change in r_B over time [52, 117] or by the velocity of the contact line [135]. Both methods have their merits. In the contact line evaporation regime, the velocity of the dynamic meniscus coincides with the contact line velocity. However, as soon as a microlayer is formed, the contact line velocity is determined by the depletion of the microlayer due to evaporation and can thus differ greatly from the velocity of the dynamic meniscus. In this case, the determination from the bubble growth rate is likely the better approach.

Possible effects of micro gravity

In micro gravity conditions, buoyancy effects are strongly reduced. Consequentially, bubble departure is delayed and the micro scale heat transfer mechanisms underneath the bubble can be observed for a longer period of time, which is stated as one of the main motivations for these experiments [37, 159]. The assumption, that micro scale heat transfer underneath the bubble is thereby independent of gravity is extensively supported by experimental evidence [26]. Therefore, it is puzzling how gravity could have any effect on the formation of a microlayer. In boiling (with or without micro gravity), the expansion velocity of a vapor bubble is generally not constant, but slows considerably towards reaching the maximum expansion radius on the heated surface. Initial bubble growth is thereby driven by inertia, where the bubble radius scales as $r_B \sim t$. This is followed by slower bubble growth driven by diffusion processes, where $r_B \sim \sqrt{t}$ [117]. Guion et al. [52] shows that in water under atmospheric conditions (measurements provided by Kim and Buongiorno [85]), the bubble expansion velocity decreases from 4 m/s to 0.5 m/s in only 2 ms. The authors identified a time scale of $10 - 100\,\mu$s for microlayer formation and $1 - 10$ ms for its evaporation. Therefore, it can be argued that delaying bubble departure through micro gravity only extends the diffusion driven bubble growth regime, where the bubble expands slowly. A dynamic wetting transition

is, however, more likely to occur at large velocities, i.e. during the initial bubble formation. Consequentially, a microlayer might well be present in micro gravity during the initial bubble growth, but disappears as the bubble growth velocity slows. Hence, only contact line evaporation is observed. In contrast, pure contact line evaporation is likely not observed in gravitational conditions, because the maximum bubble expansion on the heated surface is reached much faster, i.e. before the microlayer can evaporate completely.

The hypothesis above largely agrees with literature. For example, in the experiments of Jung and Kim [80], in which a microlayer is observed in water, the time between nucleation and bubble departure measures approximately 15 ms. Similar values are reported by Sielaff [135] for FC-72. In the experiments of Nejati et al. [111], on the other hand, the first observation of contact line evaporation is made after 168 ms. Similar values are reported by Fischer et al. [37]. However, the conjecture above is opposed by the experiments of Schweizer [132], where only evidence in favor of contact line evaporation is reported for a bubble growth cycle in normal gravity conditions lasting approximately 30 ms. Therefore, further effects have to be considered. Nevertheless, the arguments above point out that the delay of bubble departure and subsequent reduction in growth velocity in micro gravity might well cause contact line evaporation to predominate during the bubble cycle, which should be considered when comparing experimental results.

Possible effects of the boiling fluid

The second difference noted above concerns the boiling fluids, which has also been noted by Sielaff [135]. Considering the contact angle dependency of the dynamic wetting transition, it seems contradictory that contact line evaporation is rather observed for a highly wetting fluid and microlayer evaporation for water, which is partially wetting. Thus, one might suggest that for the superheated conditions found in boiling, θ_{ev} of water is smaller than θ_{ev} of refrigerants. However, this seems very unlikely, and literature to support this claim is not known to the author. Furthermore, Ca is generally higher in refrigerants for the same dewetting velocity due to lower surface tension and thus closer to Ca_{cr}. This leaves the possibility that the expansion velocity of the bubble is generally lower in refrigerants. Theoretically, this is supported by the higher ratios of vapor to liquid density found in refrigerants as opposed to water. Furthermore, ΔT and λ_l are generally lower in refrigerants, which could have an effect on bubble growth velocity due to slower heat diffusion. However, this is opposed by the fact that Δh_v is usually also reduced in refrigerants. Obviously, in boiling all these effects are coupled and numerical or experimental studies are needed. Studies found in literature, however, rarely report on the expansion velocity in detail, which is why a comparison cannot be given here. Thus, the effect of the employed fluid on the regime transition in boiling, especially on the bubble expansion velocity, remains unclear and should be investigated further.

Lastly, it is stressed that the characteristics of the surface are presumably of similar importance as the liquid due to the contact angle dependency of the dynamic wetting transition. Therefore, careful characterization of surface roughness and the dynamic contact angle are needed to compare experimental results. However, as shown in this work, the contact angle highly depends on the wall superheat. This dependency is difficult to measure and, therefore, rarely described even for a plain and smooth surface.

4.5.2 Microlayer thickness in nucleate boiling

In nucleate boiling, a general description for the microlayer thickness applicable for a wide range of fluids without the need for fluid dependent parameters is not known. This shortcoming is also noted by Guion et al. [52]. Furthermore, δ is generally described either in terms of time from bubble inception, i.e. according to Equation 2.6, or in terms of distance from the bubble center, i.e. according to Equation 2.10. While this approach might be practical due to the non-constant bubble growth velocity, the dependency on the dewetting velocity is lost. This situation can be compared to dip-coating or microchannels, where dimensionless descriptions for δ_0 are known and include Ca, i.e. the dewetting velocity, as a central parameter. Therefore, if microlayer formation underneath a growing vapor bubble is indeed a forced dynamic wetting transition, developing correlations for δ_0 based on Ca rather than describing δ in terms of r_B or t might prove beneficial. After all, the microlayers observed in this work are similar to those found in nucleate boiling in many ways and it is, therefore, likely that a general expression for δ_0 in terms of dimensionless quantities also exists.

It needs to be pointed out that none of the expressions and correlations for δ_0 known for dip-coating or microchannels, presented in section 2.2, seem suitable for nucleate boiling. Naturally, the physical layouts of all three differ, and individual correlations are needed in any case. However, for the same Ca, δ_0 is generally of the same order of magnitude in both dip-coating or microchannels. For example, for ethanol and $u = 1\,\mathrm{m\,s^{-1}}$, which can be expected in nucleate boiling, Equation 2.18 yields $\delta_0 = 375\,\mu\mathrm{m}$. Taylor's law (Equation 2.13), assuming the channel size equals the capillary length $d = l_c$, yields $\delta_0 = 210\,\mu\mathrm{m}$. These are about two magnitudes larger than δ_0 observed in nucleate boiling. This difference has also been pointed out by Kandlikar [83]. The work of Moriyama and Inoue [109] suggests, that this difference is likely due to the effects of acceleration. Thus, a general study of δ_0 in nucleate boiling is likely needed to obtain a suitable description for δ_0.

However, as observed here and elsewhere [54], descriptions for δ_0 in dip-coating and microchannels hold both with and without evaporation. Therefore, the study of δ_0 in nucleate boiling likely does not necessarily have to be performed in a boiling experiment. Instead, one can expect δ_0 produced by an gas bubble growing close to a wall and δ_0 underneath a growing vapor bubble to be governed by the same dimensionless quantities. Hence, one might propose an experiment, where a chamber is filled with liquid and gas (or vapor) is pumped into it through a small cavity in the wall. Different bubble expansion velocities could then be realized through a variation of the vapor mass flux. This approach removes the coupling between the bubble growth rate and ΔT, which allows for a much more general study of δ_0 compared to a nucleate boiling experiment. In addition, the experimental set-up is simplified.

4.5.3 Contribution of the microlayer to overall bubble growth and heat flux

As outlined in section 2.2.1, the contribution of the microlayer to overall heat flux and bubble growth has been highly discussed. Following the results of section 4.3.2, the total heat flux of the microlayer is

determined by the mass entering the microlayer. In nucleate boiling, the coefficient a_u is likely close to unity due to the absence of gravitational drainage. However, it has to be assumed that the bubble growth velocity is not constant and δ_0 deposited on the superheated wall varies with r_B. Therefore, Equation 4.13 must be adapted to nucleate boiling:

$$q_{ml,B} = \Delta h_v \rho_l \int_0^{r_{B,0,max}} \delta_0(r_B) dr_B \qquad \text{for} \qquad u_B > u_{cr}, \tag{4.21}$$

where $r_{B,0,max}$ is the maximum distance of the dynamic meniscus region from the bubble center. The dependency of δ_0 on r_B is due to the non-constant bubble growth velocity. From an experimental point of view, Equation 4.21 would allow an estimation of the contribution of the microlayer from observation of $r_B(t)$, if a function for $\delta_0(u_B)$ was known. This emphasizes the need for a description of δ_0 as argued above. Naturally, Equation 4.21 only holds in the microlayer evaporation regime, and breaks down if a regime transition occurs during bubble growth (such as in micro gravity as proposed above). Equation 4.21 could be combined with the transition model by Bure and Sato [12] or explicit measurements and correlations for Ca_{cr} as presented in section 4.2 to determine its applicability. In the contact line evaporation regime, Equation 4.16 and Equation 4.17 can then be applied assuming applicability for Ja found in nucleate boiling.

Furthermore, it has been suggested, that the ring-shaped heat flux associated with the contact line evaporation model might well be due to a very short microlayer [59, 86]. Multiple methods to distinguish a very short microlayer from the contact line evaporation regime can be deduced from the results presented in this thesis:

- If u and ΔT are known, the correlations for the regime boundary can be used to estimate the evaporation regime.
- Q_{tot} rises at the regime boundary when changing from the contact line evaporation regime into the microlayer evaporation regime. Therefore, the evaporation regime at hand should be easily identified by comparing Q_{tot} of the measurement data to the correlations in the contact line evaporation regime, Equation 4.17 and Equation 4.16, and the analytical expression for Q_{tot} in the microlayer evaporation regime. In addition, Q_{tot} caused by a very short microlayer is directly proportional to the momentarily bubble expansion velocity and is thus expected to strongly decrease towards the end of bubble expansion on the heated surface. In the contact line evaporation regime, on the other hand, Q_{tot} is expected to be constant during bubble growth on the heated surface, which is also observed by [132].
- In FC-72, the two regimes can be distinguished by the magnitude of the peak in heat flux at the contact line. Similarly to Q_{tot} above, the peak during bubble expansion can be compared to the peak during bubble detachment. If heat flux at the contact line is larger during bubble expansion than during bubble detachment, then a microlayer is likely present during bubble growth. If a microlayer

is absent during bubble expansion, however, the peak in heat flux at the contact line likely increases during bubble detachment due to the addition of convective cooling.

- The plausibility of a very short microlayer can be evaluated based on the expected microlayer length, Equation 4.19.

CHAPTER 5

Summary, conclusion, and outlook

Contact line evaporation and microlayer evaporation are considered as one of the most important mechanisms for two-phase heat transfer, and both have been studied for decades with various experimental and numerical methods. However, when which of these evaporation regimes is more prominent is not sufficiently understood and the prediction of boiling processes is, therefore, only possible to a limited degree. A possible transition between both evaporation regimes has recently been discussed in the published literature and experimental data on this topic is scarce, not least due to the coupling of dewetting velocity, wall superheat, and contact angle in boiling processes. Furthermore, microlayers themselves are observed in a multitude of experimental configurations, but despite many similarities their description is not uniform across different fields of research.

Within this work, the formation of microlayers and the heat flux within both evaporation regimes was generically investigated. The experimental set-up is based on a dip-coating concept, which was adapted to enable temperature measurement close to the solid-liquid interface with infrared thermography. A novel infrared calibration method, which accounts for the movement of the sample, was presented. From the time resolved temperature data, local heat flux and liquid thickness were calculated using numerical tools. Experiments were carried out with ethanol and FC-72 for varying levels of wall superheat and dewetting velocity.

A microlayer was not always observed in the experiments. It has been shown that the regimes of contact line evaporation and microlayer evaporation are separated by a critical dewetting velocity, which can be described by a critical capillary number. This critical capillary number rises with increasing wall superheat. A correlation for the regime boundary was presented. It is argued that the dependency of this forced dynamic dewetting transition on the wall superheat is driven by the dependency of the evaporative contact angle on the wall superheat. The exact mechanism determining the onset of film formation, however, remains unclear. Evidence for a *critical* transition, due to vanishing apparent contact angle, as well as for a *pre-critical* transition, due to the mobility of the contact line, was observed. Furthermore, it was suggested that further evaporation regimes exist in a vertical set-up, when gravitational forces can not be neglected.

The heat flux during the dewetting process has been investigated in detail. In the microlayer evaporation regime, the total heat flux is determined by the liquid mass flow entrained into the microlayer, independent of wall superheat, and analytically well described. In the contact line evaporation regime, the total heat flux is largely independent of the dewetting velocity, but strongly dependent on the wall superheat. The experiments allowed the deduction of correlations for the total heat flux within both evaporation regimes.

The height of the heat flux peak at the contact line was discussed. In ethanol, the observed trend followed the numerical predictions of the micro region model. In FC-72, however, heat flux at the contact line sharply increased at the transition into the microlayer evaporation regime, for which no concluding explanation could be provided. Furthermore, the reduction in temperature across the microlayer, i.e. the superheat remaining at the contact line, was found to be independent of the microlayer length, except only for FC-72 at low wall superheat and low dewetting velocity. It is suggested that this finding can be explained with the heat conduction within the solid.

Different shapes of the heat flux profiles were observed. An analytical analysis of the local evaporative heat flux in the microlayer evaporation regime revealed that the shape of the heat flux profile is determined by the interaction between microlayer and solid wall. The local evaporative heat flux was described by linear heat conduction through both liquid microlayer and thermal boundary layer within the solid wall, which showed good agreement with the measured local evaporative heat flux. The model suggests that heat flux rises towards the contact line if the thermal conductivity of the liquid is low and the thermal boundary layer remains small. In contrast, heat flux decreases towards the contact line if the thermal conductivity of the liquid is high, and the thermal boundary layer increases faster than the microlayer thickness depletes. A parameter α, which compares the thermal resistance of the liquid at the bottom of the microlayer to the thermal resistance of the thermal boundary layer at the contact line, was identified to describe the interaction between microlayer and wall. The change from a decreasing to an increasing profile shape thereby occurred at a threshold value α_t.

The length of the microlayer was measured for different combinations of wall superheat and dewetting velocity. A dimensionless expression for the length of the microlayer was derived on the basis of the analytical analysis of the local heat flux, which showed good agreement with the measurements. Therefore, the interaction between microlayer and solid wall not only determines the shape of the heat flux profile but also the overall length of the microlayer.

Microlayer formation underneath a growing vapor bubble is interpreted as a dynamic wetting transition. It is argued, that the observation of either pure contact line evaporation or pure microlayer evaporation in literature can be accounted to different experimental conditions, which affect the predominant evaporation regime. Next to others, the bubble expansion velocity is indicated as a key parameter, which could be influenced by the gravitational conditions and the working fluid.

Overall, the experimental, analytical and numerical methods developed and presented in this work are suitable to investigate the dynamic wetting transition in the presence of evaporation. The conducted research can be seen as a further step towards unraveling the complex interactions between fluid, wall,

contact line, and evaporation that determine the heat flux in the regimes of contact line evaporation and microlayer evaporation. The obtained results can help to improve the description and prediction of heat flux in applications such as boiling in microchannels or nucleate pool boiling. However, several questions remain unanswered. For instance, the fundamental mechanism determining the onset of microlayer formation remains unclear because the meniscus rise could not be studied in detail. This could be achieved by extending the existing experimental set-up with measurement equipment suitable to determine the whole dynamic meniscus and microlayer profile at high resolution, for example with laser interferometry as used by Qu et al. [118]. This technique would also offer a better validation for the thickness profiles calculated from the local heat flux than the one-dimensional thickness probe used in this work, and provide a means for obtaining accurate measurements of the contact angle. The latter offers a possibility to further study the disagreement between the contact angles obtained by the micro region model, the micro angle approach, and the presented experiments.

The thickness calculated from the local heat flux could easily be extended to two dimensions, which would allow the study of phenomena such as macroscopically structured surfaces or droplet formation. While the level of wall superheat in this work remained rather low, it should be extended to levels found underneath growing vapor bubbles to allow a direct comparison with nucleate boiling. The same holds true for the dewetting velocity. This comparison could be accompanied with a comparison of δ_0 measured in nucleate boiling and the experimental facility. However, while dewetting velocities in the order of $1\,\mathrm{m/s}$ can be achieved within the experimental facility, a much larger duration for acceleration will be needed.

Bibliography

[1] V. S. Ajaev, T. Gambaryan-Roisman, and P. Stephan. “Static and dynamic contact angles of evaporating liquids on heated surfaces.” In: *Journal of colloid and interface science* 342.2 (2010), pp. 550–558. DOI: 10.1016/j.jcis.2009.10.040.

[2] V. S. Ajaev and O. A. Kabov. “Heat and mass transfer near contact lines on heated surfaces.” In: *International Journal of Heat and Mass Transfer* 108 (2017), pp. 918–932. ISSN: 00179310. DOI: 10.1016/j.ijheatmasstransfer.2016.11.079.

[3] P. Aussillous and D. Quéré. “Quick deposition of a fluid on the wall of a tube.” In: *Physics of Fluids* 12.10 (2000), p. 2367. ISSN: 10706631. DOI: 10.1063/1.1289396.

[4] G. Barthau. “Active nucleation site density and pool boiling heat transferan experimental study.” In: *International Journal of Heat and Mass Transfer* 35.2 (1992), pp. 271–278. ISSN: 00179310. DOI: 10.1016/0017-9310(92)90266-u.

[5] S. Batzdorf. “Heat transfer and evaporation during single drop impingement onto a superheated wall.” PhD thesis. Darmstadt: Technische Universität Darmstadt, 2015.

[6] G. Berteloot et al. “Evaporation-induced flow near a contact line: Consequences on coating and contact angle.” In: *Europhysics Letters* 83.1 (2008), p. 14003. DOI: 10.1209/0295-5075/83/14003.

[7] G. Berteloot, A. Daerr, F. Lequeux, and L. Limat. “Dip coating with colloids and evaporation.” In: *Chemical Engineering and Processing: Process Intensification* 68 (2013), pp. 69–73. ISSN: 02552701. DOI: 10.1016/j.cep.2012.09.001.

[8] S. Bigham and S. Moghaddam. “Microscale study of mechanisms of heat transfer during flow boiling in a microchannel.” In: *International Journal of Heat and Mass Transfer* 88 (2015), pp. 111–121. ISSN: 00179310. DOI: 10.1016/j.ijheatmasstransfer.2015.04.034.

[9] T. D. Blake and K. J. Ruschak. “A maximum speed of wetting.” In: *Nature* 282.5738 (1979), pp. 489–491. ISSN: 0028-0836. DOI: 10.1038/282489a0.

[10] D. Bonn et al. “Wetting and spreading.” In: *Reviews of Modern Physics* 81.2 (2009), pp. 739–805. ISSN: 0034-6861. DOI: 10.1103/RevModPhys.81.739.

[11] F. P. Bretherton. “The motion of long bubbles in tubes.” In: *Journal of Fluid Mechanics* 10.02 (1961), p. 166. ISSN: 0022-1120. DOI: 10.1017/s0022112061000160.

[12] L. Bure and Y. Sato. “On the modelling of the transition between contact-line and microlayer evaporation regimes in nucleate boiling.” In: *Journal of Fluid Mechanics* 916 (2021), p. 42. ISSN: 0022-1120. DOI: 10.1017/jfm.2021.204.

[13] T. S. Chan, J. H. Snoeijer, and J. Eggers. “Theory of the forced wetting transition.” In: *Reviews of Modern Physics* 24.7 (2012), p. 072104. DOI: 10.1063/1.4736531.

[14] H. Chen, Z. Li, and J. Li. “Thin-film profile around long bubbles in square microchannels measured by chromatic interference method.” In: *Applied Physics Letters* 109.4 (2016), p. 041604. ISSN: 0003-6951. DOI: 10.1063/1.4959791.

[15] Z. Chen, A. Haginiwa, and Y. Utaka. “Detailed structure of microlayer in nucleate pool boiling for water measured by laser interferometric method.” In: *International Journal of Heat and Mass Transfer* 108.1 (2017), pp. 1285–1291. ISSN: 00179310. DOI: 10.1016/j.ijheatmasstransfer.2017.01.003.

[16] Z. Chen and Y. Utaka. “On heat transfer and evaporation characteristics in the growth process of a bubble with microlayer structure during nucleate boiling.” In: *International Journal of Heat and Mass Transfer* 81.747 (2015), pp. 750–759. ISSN: 00179310. DOI: 10.1016/j.ijheatmasstransfer.2014.10.058.

[17] Z. Chen et al. “Measurement of the microlayer characteristics in the whole range of nucleate boiling for water by laser interferometry.” In: *International Journal of Heat and Mass Transfer* 146.4 (2020), p. 118856. ISSN: 00179310. DOI: 10.1016/j.ijheatmasstransfer.2019.118856.

[18] Coblentz Society, Inc. *Evaluated Infrared Reference Spectra*. NIST Chemistry WebBook, NIST Standard Reference Database Number 69, Eds. P.J. Linstrom and W.G. Mallard, National Institute of Standards and Technology, Gaithersburg MD, 20899. retrieved 23.08.2021. DOI: 10.18434/T4D303.

[19] M. G. Cooper and A. Lloyd. “The microlayer in nucleate pool boiling.” In: *International Journal of Heat and Mass Transfer* 12.8 (1969), pp. 895–913. ISSN: 00179310. DOI: 10.1016/0017-9310(69)90154-9.

[20] R. G. Cox. “The dynamics of the spreading of liquids on a solid surface. Part 1. Viscous flow.” In: *Journal of Fluid Mechanics* 168.-1 (1986), p. 169. ISSN: 0022-1120. DOI: 10.1017/s0022112086000332.

[21] G. Delon, M. Fermigier, J. H. Snoeijer, and B. Andreotti. “Relaxation of a dewetting contact line. Part 2. Experiments.” In: *Journal of Fluid Mechanics* 604 (2008), pp. 55–75. DOI: 10.1017/s0022112008000979.

[22] B. Derjaguin. “On the thickness of the liquid film adhering to the walls of a vessel after emptying.” In: *Progress in Surface Science* 43.1-4 (1993), pp. 134–137. ISSN: 00796816. DOI: 10.1016/0079-6816(93)90022-n.

[23] B. Derjaguin. “Thickness of liquid layer adhering to walls of vessels on their emptying and the theory of photo-and motion-picture film coating.” In: *CR (Dokl.) Acad. Sci. URSS* 39 (1943), pp. 13–16.

[24] B. V. Derjaguin. *Film coating theory*. London: Focal Press, 1964.

[25] H. K. Dhavaleswarapu, S. V. Garimella, and J. Y. Murthy. “Microscale Temperature Measurements Near the Triple Line of an Evaporating Thin Liquid Film.” In: *Journal of Heat Transfer* 131.6 (2009), p. 1851. ISSN: 0022-1481. DOI: 10.1115/1.3090525.

[26] P. Di Marco. “Review of reduced gravity boiling heat transfer: European research.” In: *Journal of the Japan Society of Microgravity Application* 20.4 (2003), pp. 252–263.

[27] J. Dietl. “Numerical Simulation of Pool Boiling from Reentrant Type Structured Surfaces.” PhD thesis. Darmstadt: Technische Universität Darmstadt, 2015.

[28] B. R. Duffy and S. K. Wilson. “A third-order differential equation arising in thin-film flows and relevant to Tanner’s Law.” In: *Applied Mathematics Letters* 10.3 (1997), pp. 63–68. ISSN: 08939659. DOI: 10.1016/S0893-9659(97)00036-0.

[29] V. Dupont, J. R. Thome, and A. M. Jacobi. “Heat transfer model for evaporation in microchannels. Part II: Comparison with the database.” In: *International Journal of Heat and Mass Transfer* 47.14-16 (2004), pp. 3387–3401. ISSN: 00179310. DOI: 10.1016/j.ijheatmasstransfer.2004.01.007.

[30] J. Eggers. “Existence of receding and advancing contact lines.” In: *Physics of Fluids* 17.8 (2005), p. 082106. ISSN: 1070-6631. DOI: 10.1063/1.2009007.

[31] J. Eggers. “Hydrodynamic theory of forced dewetting.” In: *Physical review letters* 93.9 (2004), p. 094502. ISSN: 0031-9007. DOI: 10.1103/physrevlett.93.094502.

[32] H. S. Fath and R. L. Judd. “Influence of System Pressure on Microlayer Evaporation Heat Transfer.” In: *Journal of Heat Transfer* 100.1 (1978), pp. 49–55. ISSN: 0022-1481. DOI: 10.1115/1.3450503.

[33] M. Faustini et al. “Preparation of SolGel Films by Dip-Coating in Extreme Conditions.” In: *The Journal of Physical Chemistry C)* 114.17 (2010), pp. 7637–7645. DOI: 10.1021/jp9114755.

[34] A. Ferrari, M. Magnini, and J. R. Thome. “Numerical analysis of slug flow boiling in square microchannels.” In: *International Journal of Heat and Mass Transfer* 123.7 (2018), pp. 928–944. ISSN: 00179310. DOI: 10.1016/j.ijheatmasstransfer.2018.03.012.

[35] S. Fischer. “Experimental Investigation of Heat Transfer during Evaporation in the Vicinity of Moving Three-Phase Contact Lines.” PhD thesis. Darmstadt: Technische Universität Darmstadt, 2015.

[36] S. Fischer, T. Gambaryan-Roisman, and P. Stephan. “On the development of a thin evaporating liquid film at a receding liquid/vapour-interface.” In: *International Journal of Heat and Mass Transfer* 88 (2015), pp. 346–356. ISSN: 00179310. DOI: 10.1016/j.ijheatmasstransfer.2015.04.055.

[37] S. Fischer et al. “Experimental Investigation of Nucleate Boiling on a Thermal Capacitive Heater Under Variable Gravity Conditions.” In: *Microgravity Science and Technology* 24.3 (2012), pp. 139–146. ISSN: 0938-0108. DOI: 10.1007/s12217-011-9273-6.

[38] L. Fourgeaud et al. “Evaporation-driven dewetting of a liquid film.” In: *Physical Review Fluids* 1.4 (2016), p. 42. DOI: 10.1103/PhysRevFluids.1.041901.

[39] B. Franz. “Numerical simulation of bubble growth in subcooled pool and flow boiling under microgravity conditions.” PhD thesis. Darmstadt: Technische Universität Darmstadt, 2021.

[40] T. Fuchs, J. Kern, and P. Stephan. “A Transient Nucleate Boiling Model Including Microscale Effects and Wall Heat Transfer.” In: *Journal of Heat Transfer* 128.12 (2006), pp. 1257–1265. ISSN: 0022-1481. DOI: 10.1115/1.2349502.

[41] M. Galvagno, D. Tseluiko, H. Lopez, and U. Thiele. “Continuous and discontinuous dynamic unbinding transitions in drawn film flow.” In: *Physical review letters* 112.13 (2014), p. 137803. ISSN: 0031-9007. DOI: 10.1103/physrevlett.112.137803.

[42] M. Gao, L. Zhang, P. Cheng, and X. Quan. “An investigation of microlayer beneath nucleation bubble by laser interferometric method.” In: *International Journal of Heat and Mass Transfer* 57.1 (2013), pp. 183–189. ISSN: 00179310. DOI: 10.1016/j.ijheatmasstransfer.2012.10.017.

[43] P. Gao et al. “Film deposition and transition on a partially wetting plate in dip coating.” In: *Multiphase Science and Technology* 791 (2016), pp. 358–383. DOI: 10.1017/jfm.2016.64.

[44] A. Gholijani, C. Schlawitschek, T. Gambaryan-Roisman, and P. Stephan. “Heat transfer during drop impingement onto a hot wall: The influence of wall superheat, impact velocity, and drop diameter.” In: *International Journal of Heat and Mass Transfer* 153.1 (2020), p. 119661. ISSN: 00179310. DOI: 10.1016/j.ijheatmasstransfer.2020.119661.

[45] A. Gholijani, T. Gambaryan-Roisman, and P. Stephan. “Experimental investigation of hydrodynamics and heat transport during vertical coalescence of multiple successive drops impacting a hot wall under saturated vapor atmosphere.” In: *Experimental Thermal and Fluid Science* 118.1 (2020), p. 110145. ISSN: 08941777. DOI: 10.1016/j.expthermflusci.2020.110145.

[46] M. D. Giavedoni and F. A. Saita. “The axisymmetric and plane cases of a gas phase steadily displacing a Newtonian liquidA simultaneous solution of the governing equations.” In: *Physics of Fluids* 9.8 (1997), pp. 2420–2428. ISSN: 1070-6631. DOI: 10.1063/1.869360.

[47] N. Gion. “Modeling and Simulation of Liquid Microlayer Formation and Evaporation in Nucleate Boiling using Computational Fluid Dynamics.” Phd thesis. Massachusetts Institute of Technology, 2017.

[48] G. Giustini, S. Jung, H. Kim, and S. P. Walker. “Evaporative thermal resistance and its influence on microscopic bubble growth.” In: *International Journal of Heat and Mass Transfer* 101.6 (2016), pp. 733–741. ISSN: 00179310. DOI: 10.1016/j.ijheatmasstransfer.2016.05.081.

[49] G. Giustini et al. “Microlayer evaporation during steam bubble growth.” In: *International Journal of Thermal Sciences* 137 (2019), pp. 45–54. ISSN: 12900729. DOI: 10.1016/j.ijthermalsci.2018.11.012.

[50] I. Golobic, J. Petkovsek, and D. Kenning. “Bubble growth and horizontal coalescence in saturated pool boiling on a titanium foil, investigated by high-speed IR thermography.” In: *International Journal of Heat and Mass Transfer* 55.4 (2012), pp. 1385–1402. ISSN: 00179310. DOI: 10.1016/j.ijheatmasstransfer.2011.08.021.

[51] I. Golobic et al. “Experimental determination of transient wall temperature distributions close to growing vapor bubbles.” In: *Heat and Mass Transfer* 45.7 (2009), pp. 857–866. ISSN: 0947-7411. DOI: 10.1007/S00231-007-0295-Y.

[52] A. Guion, S. Afkhami, S. Zaleski, and J. Buongiorno. “Simulations of microlayer formation in nucleate boiling.” In: *International Journal of Heat and Mass Transfer* 127.4 (2018), pp. 1271–1284. ISSN: 00179310. DOI: 10.1016/j.ijheatmasstransfer.2018.06.041.

[53] A. N. Guion. “Modeling and simulation of liquid microlayer formation and evaporation in nucleate boiling using computational fluid dynamics.” PhD thesis. Cambridge: Massachusetts Institute of Technology, 2017.

[54] C. Guo et al. “Measurement and theoretical analysis of transient liquid film during micro-channel flow boiling.” In: *International Journal of Multiphase Flow* 130.1-3 (2020), p. 103365. ISSN: 03019322. DOI: 10.1016/j.ijmultiphaseflow.2020.103365.

[55] Z. Guo and M. S. El-Genk. “Liquid microlayer evaporation during nucleate boiling on the surface of a flat composite wall.” In: *International Journal of Heat and Mass Transfer* 37.11 (1994), pp. 1641–1655. ISSN: 00179310. DOI: 10.1016/0017-9310(94)90179-1.

[56] Y. Han and N. Shikazono. “Measurement of the liquid film thickness in micro tube slug flow.” In: *International Journal of Heat and Fluid Flow* 30.5 (2009), pp. 842–853. DOI: 10.1016/j.ijheatfluidflow.2009.02.019.

[57] Y. Han and N. Shikazono. “The effect of bubble acceleration on the liquid film thickness in micro tubes.” In: *International Journal of Heat and Fluid Flow* 31.4 (2010), pp. 630–639. DOI: 10.1016/j.ijheatfluidflow.2010.02.002.

[58] Y. Han, N. Shikazono, and N. Kasagi. “The Effect of Liquid Film Evaporation on Flow Boiling Heat Transfer in a Micro Tube.” In: *2010 14th International Heat Transfer Conference, Volume 6*. ASMEDC, 2010, pp. 123–132. ISBN: 978-0-7918-4941-5. DOI: 10.1115/IHTC14-22751.

[59] S. Hänsch and S. Walker. “Microlayer formation and depletion beneath growing steam bubbles.” In: *International Journal of Multiphase Flow* 111 (2019), pp. 241–263. ISSN: 03019322. DOI: 10.1016/j.ijmultiphaseflow.2018.11.004.

[60] S. Hänsch and S. Walker. “The hydrodynamics of microlayer formation beneath vapour bubbles.” In: *International Journal of Heat and Mass Transfer* 102 (2016), pp. 1282–1292. ISSN: 00179310. DOI: 10.1016/j.ijheatmasstransfer.2016.07.026.

[61] T. Harirchian and S. V. Garimella. “Effects of channel dimension, heat flux, and mass flux on flow boiling regimes in microchannels.” In: *International Journal of Multiphase Flow* 35.4 (2009), pp. 349–362. ISSN: 03019322. DOI: 10.1016/j.ijmultiphaseflow.2009.01.003.

[62] T. Harirchian and S. V. Garimella. “Flow regime-based modeling of heat transfer and pressure drop in microchannel flow boiling.” In: *International Journal of Heat and Mass Transfer* 55.4 (2012), pp. 1246–1260. ISSN: 00179310. DOI: 10.1016/j.ijheatmasstransfer.2011.09.024.

[63] T. Harirchian and S. V. Garimella. “The critical role of channel cross-sectional area in microchannel flow boiling heat transfer.” In: *International Journal of Multiphase Flow* 35.10 (2009), pp. 904–913. ISSN: 03019322. DOI: 10.1016/j.ijmultiphaseflow.2009.06.005.

[64] A. L. Hazel and M. Heil. “The steady propagation of a semi-infinite bubble into a tube of elliptical or rectangular cross-section.” In: *Journal of Fluid Mechanics* 470 (2002), pp. 91–114. ISSN: 0022-1120. DOI: 10.1017/s0022112002001830.

[65] M. Heil. “Finite Reynolds number effects in the Bretherton problem.” In: *Physics of Fluids* 13.9 (2001), pp. 2517–2521. ISSN: 1070-6631. DOI: 10.1063/1.1389861.

[66] R. C. Hendricks and R. R. Sharp. “Initiation of cooling due to bubble growth on a heating surface.” In: *NASA technical note* (1964), pp. D–2290.

[67] S. Herbert, S. Fischer, T. Gambaryan-Roisman, and P. Stephan. “Local heat transfer and phase change phenomena during single drop impingement on a hot surface.” In: *International Journal of Heat and Mass Transfer* 61 (2013), pp. 605–614. ISSN: 00179310. DOI: 10.1016/j.ijheatmasstransfer.2013.01.081.

[68] S. Herbert, T. Gambaryan-Roisman, and P. Stephan. “Influence of the governing dimensionless parameters on heat transfer during single drop impingement onto a hot wall.” In: *Colloids and Surfaces A: Physicochemical and Engineering Aspects* 432.1 (2013), pp. 57–63. ISSN: 09277757. DOI: 10.1016/j.colsurfa.2013.05.014.

[69] L. M. Hocking. “Meniscus draw-up and draining.” In: *European Journal of Applied Mathematics* 12.3 (2001), pp. 195–208. DOI: 10.1017/s0956792501004247.

[70] C. Höhmann and P. Stephan. “Microscale temperature measurement at an evaporating liquid meniscus.” In: *Experimental Thermal and Fluid Science* 26.2-4 (2002), pp. 157–162. ISSN: 08941777. DOI: 10.1016/S0894-1777(02)00122-X.

[71] K. Ibrahem, M. F. Abd Rabbo, T. Gambaryan-Roisman, and P. Stephan. “Experimental investigation of evaporative heat transfer characteristics at the 3-phase contact line.” In: *Experimental Thermal and Fluid Science* 34.8 (2010), pp. 1036–1041. ISSN: 08941777. DOI: 10.1016/j.expthermflusci.2010.02.014.

[72] A. M. Jacobi and J. R. Thome. “Heat Transfer Model for Evaporation of Elongated Bubble Flows in Microchannels.” In: *Journal of Heat Transfer* 124.6 (2002), pp. 1131–1136. ISSN: 0022-1481. DOI: 10.1115/1.1517274.

[73] V. Janecek. “Evaporation at microscopic scale and at high heat flux.” PhD thesis. Paris: Université Pierre et Marie Curie, 2012.

[74] V. Janecek and V. S. Nikolayev. “Apparent-contact-angle model at partial wetting and evaporation: Impact of surface forces.” In: *Physical review. E, Statistical, nonlinear, and soft matter physics* 87.1 (2013), p. 012404. DOI: 10.1103/PhysRevE.87.012404.

[75] V. Janecek et al. “Moving contact line of a volatile fluid.” In: *Physical review. E, Statistical, nonlinear, and soft matter physics* 88.6 (2013), p. 060404. DOI: 10.1103/PhysRevE.88.060404.

[76] H. H. Jawurek. “Simultaneous determination of microlayer geometry and bubble growth in nucleate boiling.” In: *International Journal of Heat and Mass Transfer* 12.8 (1969), pp. 843–848. ISSN: 00179310. DOI: 10.1016/0017-9310(69)90151-3.

[77] B. Jin, A. Acrivos, and A. Münch. “The drag-out problem in film coating.” In: *Physics of Fluids* 17.10 (2005), p. 103603. ISSN: 1070-6631. DOI: 10.1063/1.2079927.

[78] G. Jing et al. “Drying of colloidal suspensions and polymer solutions near the contact line: Deposit thickness at low capillary number.” In: *Langmuir : the ACS journal of surfaces and colloids* 26.4 (2010), pp. 2288–2293. DOI: 10.1021/la9027223.

[79] R. L. Judd and K. S. Hwang. “A Comprehensive Model for Nucleate Pool Boiling Heat Transfer Including Microlayer Evaporation.” In: *Journal of Heat Transfer* 98.4 (1976), pp. 623–629. ISSN: 0022-1481. DOI: 10.1115/1.3450610.

[80] S. Jung and H. Kim. “An experimental method to simultaneously measure the dynamics and heat transfer associated with a single bubble during nucleate boiling on a horizontal surface.” In: *International Journal of Heat and Mass Transfer* 73 (2014), pp. 365–375. ISSN: 00179310. DOI: 10.1016/j.ijheatmasstransfer.2014.02.014.

[81] S. Jung and H. Kim. “An Experimental Study on Heat Transfer Mechanisms in the Microlayer using Integrated Total Reflection, Laser Interferometry and Infrared Thermometry Technique.” In: *Heat Transfer Engineering* 36.12 (2015), pp. 1002–1012. ISSN: 0145-7632. DOI: 10.1080/01457632.2015.979109.

[82] S. G. Kandlikar. “History, Advances, and Challenges in Liquid Flow and Flow Boiling Heat Transfer in Microchannels: A Critical Review.” In: *Journal of Heat Transfer* 134.3 (2012), p. 126. ISSN: 0022-1481. DOI: 10.1115/1.4005126.

[83] S. G. Kandlikar. “Similarities and Differences Between Flow Boiling in Microchannels and Pool Boiling.” In: *Heat Transfer Engineering* 31.3 (2010), pp. 159–167. ISSN: 0145-7632. DOI: 10.1080/01457630903304335.

[84] J. Kern and P. Stephan. “Theoretical Model for Nucleate Boiling Heat and Mass Transfer of Binary Mixtures.” In: *Journal of Heat Transfer* 125.6 (2003), pp. 1106–1115. ISSN: 0022-1481. DOI: 10.1115/1.1622717.

[85] H. Kim and J. Buongiorno. “Detection of liquid-vapor-solid triple contact line in two-phase heat transfer phenomena using high-speed infrared thermometry.” In: *International Journal of Multiphase Flow* 37.2 (2011), pp. 166–172. ISSN: 03019322. DOI: 10.1016/j.ijmultiphaseflow.2010.09.010.

[86] J. Kim. “Review of nucleate pool boiling bubble heat transfer mechanisms.” In: *International Journal of Multiphase Flow* 35.12 (2009), pp. 1067–1076. ISSN: 03019322. DOI: 10.1016/j.ijmultiphaseflow.2009.07.008.

[87] L. D. Koffman and M. S. Plesset. “Experimental Observations of the Microlayer in Vapor Bubble Growth on a Heated Solid.” In: *Journal of Heat Transfer* 105.3 (1983), pp. 625–632. ISSN: 0022-1481. DOI: 10.1115/1.3245631.

[88] W. Kolb and R. L. Cerro. “Coating the inside of a capillary of square cross section.” In: *Chemical Engineering Science* 46.9 (1991), pp. 2181–2195. ISSN: 00092509. DOI: 10.1016/0009-2509(91)85119-i.

[89] M. T. Kreutzer et al. “Inertial and interfacial effects on pressure drop of Taylor flow in capillaries.” In: *AIChE Journal* 51.9 (2005), pp. 2428–2440. ISSN: 0001-1541. DOI: 10.1002/aic.10495.

[90] C. Kunkelmann. “Numerical Modeling and Investigation of Boiling Phenomena.” PhD thesis. Technische Universität Darmstadt, 2011.

[91] C. Kunkelmann and P. Stephan. “CFD Simulation of Boiling Flows Using the Volume-of-Fluid Method within OpenFOAM.” In: *Numerical Heat Transfer, Part A: Applications* 56.8 (2009), pp. 631–646. ISSN: 1040-7782. DOI: 10.1080/10407780903423908.

[92] C. Kunkelmann and P. Stephan. “Numerical simulation of the transient heat transfer during nucleate boiling of refrigerant HFE-7100.” In: *International Journal of Refrigeration* 33.7 (2010), pp. 1221–1228. ISSN: 01407007. DOI: 10.1016/j.ijrefrig.2010.07.013.

[93] C. Kunkelmann et al. “The effect of three-phase contact line speed on local evaporative heat transfer: Experimental and numerical investigations.” In: *International Journal of Heat and Mass Transfer* 55.7-8 (2012), pp. 1896–1904. ISSN: 00179310. DOI: 10.1016/j.ijheatmasstransfer.2011.11.044.

[94] L. Landau and B. Levich. “Dragging of a Liquid by a Moving Plate.” In: *Acta Physicochimica URSS* 17.42 (1942), pp. 141–15342-54. DOI: 10.1016/b978-0-08-092523-3.50016-2.

[95] L. D. Landau and E. M. Lifshitz. *Fluid Mechanics*. Vol. 6. Course of Theoretical Physics. 1959.

[96] M. Le Berre, Y. Chen, and D. Baigl. “From convective assembly to Landau-Levich deposition of multilayered phospholipid films of controlled thickness.” In: *Langmuir : the ACS journal of surfaces and colloids* 25.5 (2009), pp. 2554–2557. DOI: 10.1021/la803646e.

[97] J. Lee and G. Son. “Numerical simulation of liquid film formation and evaporation in dip coating.” In: *International Communications in Heat and Mass Transfer* 68 (2015), pp. 220–227. ISSN: 07351933. DOI: 10.1016/j.icheatmasstransfer.2015.09.008.

[98] E. W. Lemmon, I. H. Bell, M. L. Huber, and M. O. McLinden. *NIST Standard Reference Database 23: Reference Fluid Thermodynamic and Transport Properties-REFPROP, Version 10.0, National Institute of Standards and Technology*. 2018. DOI: 10.18434/T4/1502528. URL: https://www.nist.gov/srd/refprop.

[99] H. G. MacGregor and H. H. Jawurek. “High speed cine laser interferometry technique for microlayer studies in boiling.” In: *N&O JOERNAAL* (1992).

[100] M. Magnini, B. Pulvirenti, and J. R. Thome. “Numerical investigation of hydrodynamics and heat transfer of elongated bubbles during flow boiling in a microchannel.” In: *International Journal of Heat and Mass Transfer* 59 (2013), pp. 451–471. ISSN: 00179310. DOI: 10.1016/j.ijheatmasstransfer.2012.12.010.

[101] M. Magnini, B. Pulvirenti, and J. R. Thome. “Numerical investigation of the influence of leading and sequential bubbles on slug flow boiling within a microchannel.” In: *International Journal of Thermal Sciences* 71.081302 (2013), pp. 36–52. ISSN: 12900729. DOI: 10.1016/j.ijthermalsci.2013.04.018.

[102] M. Magnini and J. R. Thome. “An updated three-zone heat transfer model for slug flow boiling in microchannels.” In: *International Journal of Multiphase Flow* 91 (2017), pp. 296–314. ISSN: 03019322. DOI: 10.1016/j.ijmultiphaseflow.2017.01.015.

[103] M. Magnini and J. R. Thome. “Computational Study of Saturated Flow Boiling Within a Microchannel in the Slug Flow Regime.” In: *Journal of Heat Transfer* 138.2 (2016), p. 84. ISSN: 0022-1481. DOI: 10.1115/1.4031234.

[104] M. Maleki et al. “Landau-Levich menisci.” In: *Journal of colloid and interface science* 354.1 (2011), pp. 359–363. DOI: 10.1016/j.jcis.2010.07.069.

[105] I. Marchuk, A. Karchevsky, A. Surtaev, and O. Kabov. “Heat Flux at the Surface of Metal Foil Heater under Evaporating Sessile Droplets.” In: *International Journal of Aerospace Engineering* 2015.1 (2015), pp. 1–5. ISSN: 1687-5966. DOI: 10.1155/2015/391036.

[106] M. Monde. “Measurement of Liquid Film Thickness During Passage of Bubbles in a Vertical Rectangular Channel.” In: *Journal of Heat Transfer* 112.1 (1990), pp. 255–258. ISSN: 0022-1481. DOI: 10.1115/1.2910357.

[107] F. D. Moore and R. B. Mesler. “The measurement of rapid surface temperature fluctuations during nucleate boiling of water.” In: *AIChE Journal* 7.4 (1961), pp. 620–624. DOI: 10.1002/aic.690070418.

[108] S. Moosman and G. Homsy. “Evaporating menisci of wetting fluids.” In: *Journal of Colloid and Interface Science* 73.1 (1980), pp. 212–223. ISSN: 00219797. DOI: 10.1016/0021-9797(80)90138-1.

[109] K. Moriyama and A. Inoue. “Thickness of the Liquid Film Formed by a Growing Bubble in a Narrow Gap Between Two Horizontal Plates.” In: *Journal of Heat Transfer* 118.1 (1996), pp. 132–139. ISSN: 0022-1481. DOI: 10.1115/1.2824026.

[110] S. J. S. Morris. “Contact angles for evaporating liquids predicted and compared with existing experiments.” In: *Journal of Fluid Mechanics* 432 (2001), pp. 1–30. DOI: 10.1017/S0022112000003074.

[111] I. Nejati et al. “Experimental Investigation of Single Bubble Nucleate Boiling in Microgravity.” In: *Microgravity Science and Technology* 32.4 (2020), pp. 597–607. ISSN: 0938-0108. DOI: 10.1007/s12217-020-09813-z.

[112] G. Nisato, D. Lupo, and S. Ganz. *Organic and Printed Electronics*. Jenny Stanford Publishing, 2016. ISBN: 9780429083686. DOI: 10.1201/b20043.

[113] NIST Mass Spectrometry Data Center, William E. Wallace, director. *Infrared Spectra*. NIST Chemistry WebBook, NIST Standard Reference Database Number 69, Eds. P.J. Linstrom and W.G. Mallard, National Institute of Standards and Technology, Gaithersburg MD, 20899. retrieved 23.08.2021. DOI: 10.18434/T4D303.

[114] J. Okajima and P. Stephan. "Numerical simulation of liquid film formation and its heat transfer through vapor bubble expansion in a microchannel." In: *International Journal of Heat and Mass Transfer* 136.4 (2019), pp. 1241–1249. ISSN: 00179310. DOI: 10.1016/j.ijheatmasstransfer.2019.03.004.

[115] B. E. Poling, J. M. Prausnitz, and J. P. O'Connell. *The properties of gases and liquids*. 5th ed. McGraw-Hill's AccessEngineering. New York: McGraw-Hill, 2001. ISBN: 0070116822.

[116] M. Potash and P. Wayner. "Evaporation from a two-dimensional extended meniscus." In: *International Journal of Heat and Mass Transfer* 15.10 (1972), pp. 1851–1863. ISSN: 00179310. DOI: 10.1016/0017-9310(72)90058-0.

[117] A. Prosperetti. "Vapor Bubbles." In: *Annual Review of Fluid Mechanics* 49.1 (2017), pp. 221–248. ISSN: 0066-4189. DOI: 10.1146/annurev-fluid-010816-060221.

[118] D. Qu, E. Ramé, and S. Garoff. "Dip-coated films of volatile liquids." In: *Physics of Fluids* 14.3 (2002), pp. 1154–1165. ISSN: 1070-6631. DOI: 10.1063/1.1449467.

[119] D. Quéré. "On the minimal velocity of forced spreading in partial wetting." In: *C. R. Acad. Sci. II* (1991), (in Frensh).

[120] D. Quéré and E. Archer. "The Trail of the Drops." In: *Europhysics Letters* 24.9 (1993), pp. 761–766. DOI: 10.1209/0295-5075/24/9/011.

[121] D. Quéré. "Coating on a Fiber." In: *Annual Review of Fluid Mechanics* 31.1 (1999), pp. 347–384. DOI: 10.1146/annurev.fluid.31.1.347.

[122] R. Raj et al. "Contact line behavior for a highly wetting fluid under superheated conditions." In: *International Journal of Heat and Mass Transfer* 55.9-10 (2012), pp. 2664–2675. ISSN: 00179310. DOI: 10.1016/j.ijheatmasstransfer.2011.12.026.

[123] A. Y. Rednikov and P. Colinet. "Asymptotic analysis of the contact-line microregion for a perfectly wetting volatile liquid in a pure-vapor atmosphere." In: *Physical Review Fluids* 2.12 (2017). DOI: 10.1103/PhysRevFluids.2.124006.

[124] A. Y. Rednikov and P. Colinet. "Contact angles for perfectly wetting pure liquids evaporating into air: Between de Gennes-type and other classical models." In: *Physical Review Fluids* 5.11 (2020), p. 279. DOI: 10.1103/PhysRevFluids.5.114007.

[125] A. Y. Rednikov, S. Rossomme, and P. Colinet. "Steady Microstructure of a Contact Line for a Liquid on a Heated Surface Overlaid with its Pure Vapor: Parametric Study for a Classical Model." In: *Multiphase Science and Technology* 21.3 (2009), pp. 213–248. DOI: 10.1615/MultScienTechn.v21.i3.30.

[126] E. Rio and F. Boulogne. “Withdrawing a solid from a bath: How much liquid is coated?” In: *Advances in colloid and interface science* 247 (2017), pp. 100–114. DOI: 10.1016/j.cis.2017.01.006.

[127] A. de Ryck and Quéré. “Gravity and Inertia Effects in Plate Coating.” In: *Journal of colloid and interface science* 203.2 (1998), pp. 278–285. DOI: 10.1006/jcis.1998.5444.

[128] C. Schlawitschek. “Numerical simulation of drop impact and evaporation on superheated surfaces at low and high ambient pressures.” PhD thesis. Darmstadt: Technische Universität Darmstadt, 2020.

[129] K. Schweikert, A. Sielaff, and P. Stephan. “On the transition between contact line evaporation and microlayer evaporation during the dewetting of a superheated wall.” In: *International Journal of Thermal Sciences* 145.8 (2019), p. 106025. ISSN: 12900729. DOI: 10.1016/j.ijthermalsci.2019.106025.

[130] K. Schweikert, A. Sielaff, and P. Stephan. “Pixel-wise in situ calibration method for high accuracy infrared thermography of moving targets.” In: *Infrared Physics & Technology* 37.5 (2021), p. 103862. ISSN: 13504495. DOI: 10.1016/j.infrared.2021.103862.

[131] K. Schweikert, A. Sielaff, and P. Stephan. “Heat Flux During Dip-Coating of a Superheated Substrate.” In: *Interfacial Phenomena and Heat Transfer* 7.3 (2019), pp. 269–281. DOI: 10.1615/InterfacPhenomHeatTransfer.2019032623.

[132] N. Schweizer. “Multi-scale investigation of nucleate boiling phenomena in microgravity.” PhD thesis. Technische Universität Darmstadt, 2010.

[133] R. V. Sedev and J. G. Petrov. “The critical condition for transition from steady wetting to film entrainment.” In: *Colloids and Surfaces* 53.1 (1991), pp. 147–156. ISSN: 01666622. DOI: 10.1016/0166-6622(91)80041-l.

[134] R. R. Sharp. “The Nature of Liquid Film Evaporation During Nucleate Boiling.” In: *NASA technical note* 1964 (), pp. D–1997.

[135] A. Sielaff. “Experimental investigation of single bubbles and bubble interactions in nucleate boiling.” PhD thesis. Technische Universität Darmstadt, 2014.

[136] J. H. Snoeijer et al. “Thick films of viscous fluid coating a plate withdrawn from a liquid reservoir.” In: *Physical review letters* 100.24 (2008), p. 244502. ISSN: 0031-9007. DOI: 10.1103/physrevlett.100.244502.

[137] J. H. Snoeijer and B. Andreotti. “Moving Contact Lines: Scales, Regimes, and Dynamical Transitions.” In: *Annual Review of Fluid Mechanics* 45.1 (2013), pp. 269–292. ISSN: 0066-4189. DOI: 10.1146/annurev-fluid-011212-140734.

[138] J. H. Snoeijer, G. Delon, M. Fermigier, and B. Andreotti. “Avoided critical behavior in dynamically forced wetting.” In: *Physical review letters* 96.17 (2006), p. 174504. ISSN: 0031-9007. DOI: 10.1103/physrevlett.96.174504.

[139] J. H. Snoeijer and J. Eggers. “Asymptotic analysis of the dewetting rim.” In: *Physical review. E, Statistical, nonlinear, and soft matter physics* 82.5 Pt 2 (2010), p. 056314. DOI: 10.1103/physreve.82.056314.

[140] N. R. Snyder and D. K. Edwards. “Summary of confrence on bubble dynamics and boiling heat transfer.” In: *Jet Propulsion Laboratory* June 1415.Memo (1956), pp. 20–137.

[141] C. Sodtke, J. Kern, N. Schweizer, and P. Stephan. “High resolution measurements of wall temperature distribution underneath a single vapour bubble under low gravity conditions.” In: *International Journal of Heat and Mass Transfer* 49.5-6 (2006), pp. 1100–1106. ISSN: 00179310. DOI: 10.1016/j.ijheatmasstransfer.2005.07.054.

[142] V. Srinivasan et al. “Evaporation of an isolated liquid plug moving inside a capillary tube.” In: *International Journal of Heat and Mass Transfer* 89.2 (2015), pp. 176–185. ISSN: 00179310. DOI: 10.1016/j.ijheatmasstransfer.2015.05.039.

[143] P. Stephan and J. Hammer. “A new model for nucleate boiling heat transfer.” In: *Wärme- und Stoffübertragung* 30.2 (1994), pp. 119–125. ISSN: 0042-9929. DOI: 10.1007/BF00715018.

[144] P. C. Stephan and C. A. Busse. “Analysis of the heat transfer coefficient of grooved heat pipe evaporator walls.” In: *International Journal of Heat and Mass Transfer* 35.2 (1992), pp. 383–391. ISSN: 00179310. DOI: 10.1016/0017-9310(92)90276-X.

[145] P. Stephan. *Wärmedurchgang bei Verdampfung aus Kapillarrillen in Wärmerohren: Zugl.: Stuttgart, Univ., Diss*. Als Ms. gedr. Vol. Nr. 59. Fortschritt-Berichte / VDI Reihe 19, Wärmetechnik, Kältetechnik. Düsseldorf: VDI-Verl., 1992. ISBN: 3181459194.

[146] Y. Sun et al. “Transient film thickness and microscale heat transfer during flow boiling in microchannels.” In: *International Journal of Heat and Mass Transfer* 116.1 (2018), pp. 458–470. ISSN: 00179310. DOI: 10.1016/j.ijheatmasstransfer.2017.09.027.

[147] G. I. Taylor. “Deposition of a viscous fluid on the wall of a tube.” In: *Journal of Fluid Mechanics* 10.02 (1961), p. 161. ISSN: 0022-1120. DOI: 10.1017/s0022112061000159.

[148] J. R. Thome, V. Dupont, and A. M. Jacobi. “Heat transfer model for evaporation in microchannels. Part I: Presentation of the model.” In: *International Journal of Heat and Mass Transfer* 47.14-16 (2004), pp. 3375–3385. ISSN: 00179310. DOI: 10.1016/j.ijheatmasstransfer.2004.01.006.

[149] T. C. Thulasidas, M. A. Abraham, and R. L. Cerro. “Bubble-train flow in capillaries of circular and square cross section.” In: *Chemical Engineering Science* 50.2 (1995), pp. 183–199. ISSN: 00092509. DOI: 10.1016/0009-2509(94)00225-g.

[150] A. Urbano, S. Tanguy, and C. Colin. “Direct numerical simulation of nucleate boiling in zero gravity conditions.” In: *International Journal of Heat and Mass Transfer* 143 (2019), p. 118521. ISSN: 00179310. DOI: 10.1016/j.ijheatmasstransfer.2019.118521.

[151] A. Urbano, S. Tanguy, G. Huber, and C. Colin. “Direct numerical simulation of nucleate boiling in micro-layer regime.” In: *International Journal of Heat and Mass Transfer* 123.5 (2018), pp. 1128–1137. ISSN: 00179310. DOI: 10.1016/j.ijheatmasstransfer.2018.02.104.

[152] Y. Utaka, K. Hu, Z. Chen, and T. Morokuma. “Measurement of contribution of microlayer evaporation applying the microlayer volume change during nucleate pool boiling for water and ethanol.” In: *International Journal of Heat and Mass Transfer* 125.747 (2018), pp. 243–247. ISSN: 00179310. DOI: 10.1016/j.ijheatmasstransfer.2018.04.044.

[153] Y. Utaka, Y. Kashiwabara, and M. Ozaki. “Microlayer structure in nucleate boiling of water and ethanol at atmospheric pressure.” In: *International Journal of Heat and Mass Transfer* 57.1 (2013), pp. 222–230. ISSN: 00179310. DOI: 10.1016/j.ijheatmasstransfer.2012.10.031.

[154] Y. Utaka, Y. Kashiwabara, M. Ozaki, and Z. Chen. “Heat transfer characteristics based on microlayer structure in nucleate pool boiling for water and ethanol.” In: *International Journal of Heat and Mass Transfer* 68.4 (2014), pp. 479–488. ISSN: 00179310. DOI: 10.1016/j.ijheatmasstransfer.2013.09.063.

[155] Y. Utaka, Y. Tasaki, and S. Okuda. “Behaviors of micro-layer in micro-channel boiling system applying laser extinction method.” In: *Heat TransferAsian Research* 35.1 (2006), pp. 35–46. ISSN: 1099-2871. DOI: 10.1002/htj.20096.

[156] S. van Stralen, M. S. Sohal, R. Cole, and W. M. Sluyter. “Bubble growth rates in pure and binary systems: Combined effect of relaxation and evaporation microlayers.” In: *International Journal of Heat and Mass Transfer* 18.3 (1975), pp. 453–467. ISSN: 00179310. DOI: 10.1016/0017-9310(75)90033-2.

[157] O. V. Voinov. “Hydrodynamics of wetting.” In: *Fluid Dynamics* 11.5 (1976), pp. 714–721. DOI: 10.1007/bf01012963.

[158] C. M. Voutsinos and R. L. Judd. “Laser Interferometric Investigation of the Microlayer Evaporation Phenomenon.” In: *Journal of Heat Transfer* 97.1 (1975), pp. 88–92. ISSN: 0022-1481. DOI: 10.1115/1.3450295.

[159] E. Wagner, C. Sodtke, N. Schweizer, and P. Stephan. “Experimental study of nucleate boiling heat transfer under low gravity conditions using TLCs for high resolution temperature measurements.” In: *Heat and Mass Transfer* 42.10 (2006), pp. 875–883. ISSN: 0947-7411. DOI: 10.1007/s00231-006-0146-2.

[160] E. Wagner and P. Stephan. “High-Resolution Measurements at Nucleate Boiling of Pure FC-84 and FC-3284 and Its Binary Mixtures.” In: *Journal of Heat Transfer* 131.12 (2009), p. 662. ISSN: 0022-1481. DOI: 10.1115/1.3220143.

[161] P. C. Wayner, Y. K. Kao, and L. V. LaCroix. “The interline heat-transfer coefficient of an evaporating wetting film.” In: *International Journal of Heat and Mass Transfer* 19.5 (1976), pp. 487–492. ISSN: 00179310. DOI: 10.1016/0017-9310(76)90161-7.

[162] D. A. White and J. A. Tallmadge. “Theory of drag out of liquids on flat plates.” In: *Chemical Engineering Science* 20.1 (1965), pp. 33–37. ISSN: 00092509. DOI: 10.1016/0009-2509(65)80041-0.

[163] D. A. White and J. A. Tallmadge. “A theory of withdrawal of cylinders from liquid baths.” In: *AIChE Journal* 12.2 (1966), pp. 333–339. DOI: 10.1002/aic.690120223.

[164] H. Wong, C. J. Radke, and S. Morris. “The motion of long bubbles in polygonal capillaries. Part 1. Thin films.” In: *Journal of Fluid Mechanics* 292 (1995), pp. 71–94. ISSN: 0022-1120. DOI: 10.1017/s0022112095001443.

[165] T. Yabuki and O. Nakabeppu. “Heat transfer mechanisms in isolated bubble boiling of water observed with MEMS sensor.” In: *International Journal of Heat and Mass Transfer* 76.3 (2014), pp. 286–297. ISSN: 00179310. DOI: 10.1016/j.ijheatmasstransfer.2014.04.012.

[166] T. Yabuki and O. Nakabeppu. “Microlayer formation characteristics in pool isolated bubble boiling of water.” In: *Heat and Mass Transfer* 53.5 (2017), pp. 1745–1750. ISSN: 0947-7411. DOI: 10.1007/s00231-016-1936-9.

[167] T. Yabuki and O. Nakabeppu. “Microscale wall heat transfer and bubble growth in single bubble subcooled boiling of water.” In: *International Journal of Heat and Mass Transfer* 100.3 (2016), pp. 851–860. ISSN: 00179310. DOI: 10.1016/j.ijheatmasstransfer.2016.04.112.

[168] Y. Zhang and Y. Utaka. “Characteristics of a liquid microlayer formed by a confined vapor bubble in micro gap boiling between two parallel plates.” In: *International Journal of Heat and Mass Transfer* 84.1 (2015), pp. 475–485. ISSN: 00179310. DOI: 10.1016/j.ijheatmasstransfer.2015.01.013.

[169] J. Ziegler, J. H. Snoeijer, and J. Eggers. “Film transitions of receding contact lines.” In: *The European Physical Journal Special Topics* 166.1 (2009), pp. 177–180. DOI: 10.1140/epjst/e2009-00902-3.

List of Figures

List of Tables

APPENDIX A

Appendix

Table A.1: Measurement and control devices

Component	Company	Description
source measure unit	Keithley / Tektronix	Keithley 2701
heater power source	Elektro-Automatik	EA-PS 3065-03 B
interferometer	Precitec	CHRorodile 2SE
infrared camera	Flir	X6901sc
motor	Aerotech	BMS465-A-E100H
motor controller	Aerotech	SOLISTCP30
temperature control unit	Huber	Petite Fleur
pressure sensor	Wika	S-20

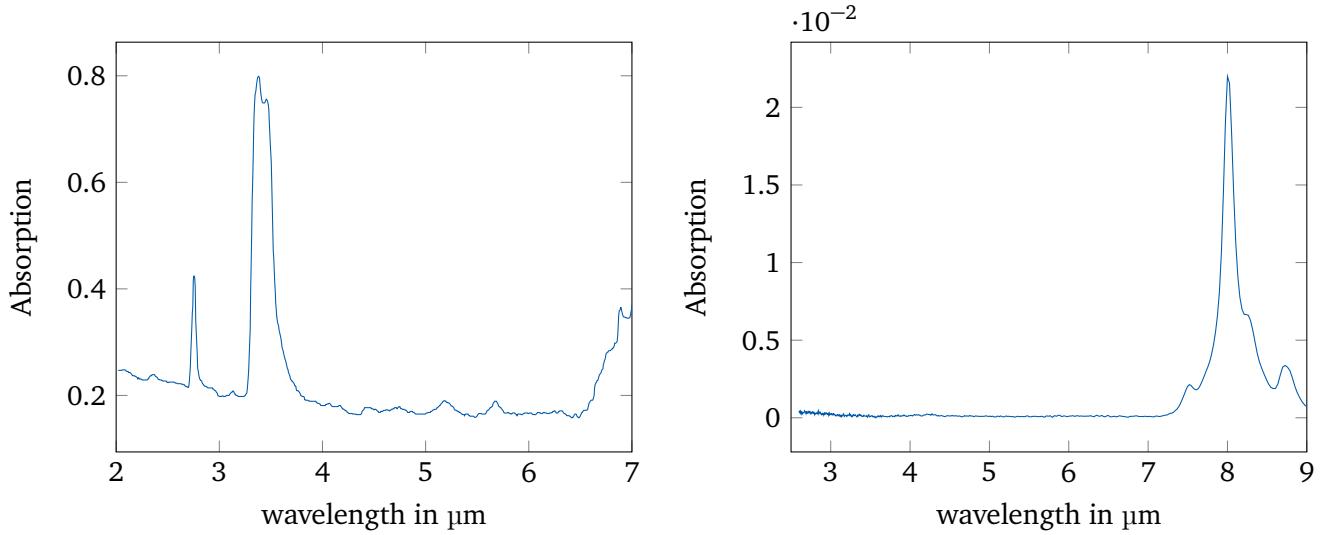

(a) ethanol

(b) FC-72

Figure A.1: Infrared absorption spectra of (a) ethanol vapor [18] and (b) FC-72 vapor [113].

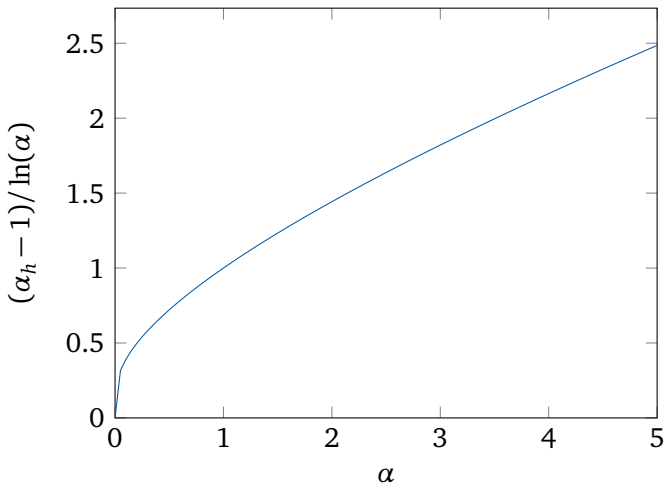

Figure A.2: Dependency of Equation 4.19 on α.